A Dissertation Submitted for a Doctorate in Materials Science

Plasmonic Nanoengineering in Hollow Metal Nanostructures: An Electron Energy-Loss Spectroscopy Study

Aziz Genç

Supervisor: Prof. Jordi Arbiol i Cobos

Tutor: Dr. Xavier Granados i García

Universitat Autònoma de Barcelona
Department of Physics, Faculty of Sciences

Institut de Ciència de Materials de Barcelona (ICMAB-CSIC)
Institut Català de Nanociència i Nanotecnologia (ICN2)

July 2015

Jordi Arbiol i Cobos, ICREA Research Professor at Institut Català de Nanociència i Nanotecnologia and **Xavier Granados García**, Tenured Scientist at Institut de Ciència de Materials de Barcelona

CERTIFY

that Aziz Genç, MSc in Materials Science and Engineering, carried out the work entitled "Plasmonic Nanoengineering in Hollow Metal Nanostructures: An Electron Energy-Loss Spectroscopy Study"under their direction and qualifies for the degree of Doctor in Materials Science.

And for that record, sign this certificate

Prof. Jordi Arbiol i Cobos Dr. Xavier Granados i García

Bellaterra, July 2015

Abstract

Metallic nanostructures have received great attention due to their ability to generate surface plasmon resonances, which are the collective oscillations of conduction band electrons in a metal excited by an electromagnetic field. Ever-increasing interest in plasmonic metal nanostructures has emerged into the field of *plasmonics*, which can be defined as the science and technology of generation, control and manipulation of excitations resulted by the light-matter interactions. Plasmonic nanostructures have been used in many different applications spanning over the fields of biology, physics, chemistry, engineering and medicine. For instance, they are widely used in sensing, surface enhanced Raman spectroscopy (SERS), plasmon-enhanced solar cells, photodetectors, drug delivery and cancer therapy as well as nanolasers, invisibility cloaks and quantum computing. It is very-well known that plasmonic properties of metallic nanostructures are greatly affected by different parameters such as the size, shape, composition and local environment. Thus, understanding and manipulating the plasmonic properties at the nanoscale is essential to fabricate devices with the desired features. In this thesis manuscript, we present a detailed characterization study on the plasmonic properties of hollow AuAg nanostructures by using electron energy-loss spectroscopy (EELS) technique. Hollow nanostructures are known to have enhanced plasmonic properties compared to their solid counterparts due to the coupling of inner and outer plasmon resonances. This study involves the first examples of spatially resolved plasmon mapping in hollow AuAg nanostructures such as nanoboxes and nanotubes, both in 2D and 3D.

This thesis manuscript is divided into six chapters. Chapter 1 is the introduction, which includes the theoretical background of surface plasmon resonances, the reviews of different parameters that affects the plasmonic properties of metal nanostructures, the application areas of plasmonic nanostructures and characterization techniques used to determine the plasmonic properties. In Chapter 2, details of the methodology are presented. This chapter includes the details about the synthesis, EELS experiments, data processing and simulations as well as general introductions to the techniques.

Experimental results and accompanying simulations are presented in Chapters 3, 4 and 5, where we perform a detailed characterization and modeling studies on complex metal nanostructures. Chapter 3 deals with the characterization of plasmonic properties of cuboid AuAg nanostructures, which are engineered from solid Ag nanocubes to hollow AuAg nanoboxes and nanoframes. The EELS data are processed by different routines and their influence on the obtained results are discussed. A series of boundary element method (BEM) simulations are used to elaborate the experimental results presented in this chapter. Moreover, the sensing properties of single-walled AuAg nanoboxes and solid Au nanoparticles against conjugation events with bovine serum albumin (BSA) and its

antibodies are compared in this chapter, revealing about 5-fold higher sensitivity for the case of hollow nanoboxes. Plasmonic properties of 1D hollow AuAg nanostructures are presented in Chapter 4. In this chapter, plasmon resonances of completely hollow AuAg nanotubes and hybrid AuAg nanotubes, a sequence formation of solid Ag core with AuAg alloyed shell and hollow AuAg parts, are compared, where simulation studies are used to discuss the difference between solid nanowires and hollow nanotubes. Chapter 5 deals with the 3D plasmonic properties of different AuAg nanostructures such as Ag@Au core-shell nanocubes, partially hollow AgAu nanocubes and AuAg nanoframes, as well as the coupling between two core-shell nanocubes and a core-shell nanocube and an AuAg nanoframe. Finally, Chapter 6 includes the general conclusions of the whole thesis and some future works that are already on-going or planned to be done in the near future.

Acknowledgements

A PhD thesis is not a venture that one can do all alone. The research presented in this dissertation could not have happened without the assistance, guidance and friendship of many outstanding individuals. With this words, I would like to thank all the people who helped me to get through this final stage.

Firstly, I would like to express my deepest gratitude to my supervisor Prof. Dr. Jordi Arbiol for his guidance, support and motivation during the past three years. He was always available for me and it helped me a lot to get through tough times during my studies. I am deeply indebted to him for all his help.

A big thanks goes to the great people of GAeN, María de la Mata, Francisco Belarre and (now doctors!) Reza Zamani and Roger Guzmán for their friendship and support both inside and outside of the institute. For a good part of my PhD, María and I were the only PhD students in the group and she has been the most wonderful colleague in answering my endless questions and even a better friend during this enduring experience. A special thanks also goes to Francisco for his daily optimism, that helped me a lot.

This work would have not been possible without the great samples provided from Inorganic Nanoparticles Group at ICN2 led by Prof. Víctor F. Puntes. In particular, I am very grateful to Javier Patarroyo for his endless efforts to synthesize the perfect samples for me. The help from Dr. Neus Gómez Bastús and Edgar González (now at Pontifica Universidad Javeriana in Colombia) is also greatly acknowledged.

The most part of the EELS studies shown in this dissertation are conducted at the Advanced Microscopy Laboratory (LMA-INA) in Zaragoza and Dr. Raúl Arenal is greatly acknowledged for his help during long hours spent in EELS acquisitions. Nice people of LMA is also acknowledged for their hospitality and solving many day-to-day problems during the experiments.

Three dimensional EELS experiments are conducted at the Ernst Ruska-Centre (ER-C) for Microscopy and Spectroscopy with Electrons in Jülich during my four months research stay. I would like to thank Prof. Rafal E. Dunin-Borkowski for hosting me at ER-C. The experiments are conducted with great assistance provided by Dr. Martial Duchamp, whom I also need to thank for the VCA code and teaching me how to process the EELS data. I would also like to thank Dr. Lothar Houben for his help in the microscope during the analysis of many different samples, some of which are not presented in this dissertation, and for (still on-going) tomography reconstructions. Some additional help provided by Dr. Vadim Migunov and Dr. András Kovács is also acknowledged. I should also thank all the ER-C crew for their hospitality and fruitful discussions at the after lunch coffee sessions and friendship outside of the institute. I received a scholarship from the German Academic Exchange Service (DAAD) during my stay at ER-C and it is greatly acknowledged.

This work would have not been the same without the amazing simulations conducted by Dr. Jordi Sancho-Parramon from Ruder Bošković Institute in Croatia. His contributions greatly enhanced the quality of this dissertation and it is deeply acknowledged.

Although we have decided not to include them in this dissertation, I would like to thank Prof. Silvija Gradečak and Dr. Xiang Zhou from Massachusetts Institute of Technology (MIT) for wonderful CL studies. I would also like to thank them and the rest of the Gradečak Group for their hospitality during my visits to MIT. I am also thankful to the support from the Electron Microscopy Division of ICN2, to Dr. Belén Ballesteros, Marcos Rosado and Elzbieta Pach. I also would like to thank Dr. Beri Mbenkum and Dr. Doris Cadavid from IREC and Oihane Beldarrain from CNM-CSIC for their help during hydrogen plasma cleaning.

This work could not be conducted without the generous PhD scholarship from the Ministry of National Education (MEB) of Turkey, which is greatly acknowledged.

I would also like to thank friends who made the experience easier, namely to Coco, Onur, Erdal, Saul, Aslı and many others at ICMAB and ICN2.

Finally, thanks to my family, for their great support and always being there for me.

To my dearest, Ekinsu for her love and understanding. The idea of getting back together soon was my lighthouse throughout this journey.

Contents

Abstract **v**

Acknowledgements **vii**

List of Figures **xiii**

List of Tables **xxvii**

1 Introduction **1**
- 1.1 Plasmonics: Theoretical background . . . 2
  - 1.1.1 Light, an electromagnetic wave . . . 2
    - 1.1.1.1 Maxwell's equations . . . 2
    - 1.1.1.2 The dielectric function of the free electron gas . . . 5
  - 1.1.2 Surface plasmon resonances . . . 11
    - 1.1.2.1 Surface plasmon polaritons . . . 11
    - 1.1.2.2 Localized surface plasmon resonances . . . 14
- 1.2 Effects of intrinsic and extrinsic parameters on the LSPRs . . . 18
  - 1.2.1 Size effects . . . 18
  - 1.2.2 Shape effects . . . 20
  - 1.2.3 Composition effects . . . 24
  - 1.2.4 Environmental effects . . . 26
  - 1.2.5 Plasmon coupling . . . 28
  - 1.2.6 Plasmon hybridization in void plasmons . . . 30
- 1.3 Applications of plasmonic nanostructures . . . 34
  - 1.3.1 Plasmonic nanosensing . . . 34
  - 1.3.2 Surface-enhanced Raman spectroscopy . . . 37
  - 1.3.3 Plasmon-enhanced photovoltaics . . . 39
  - 1.3.4 Applications in nanomedicine . . . 41
- 1.4 Characterization of LSPR properties . . . 43
  - 1.4.1 Cathodoluminescence (CL) spectroscopy . . . 44
  - 1.4.2 Electron energy-loss spectroscopy (EELS) for plasmonics . . . 47

2 Methodology **53**
- 2.1 Synthesis of hollow AuAg nanostructures . . . 55
- 2.2 Transmission electron microscopy (TEM) . . . 57
  - 2.2.1 Electron-matter interactions . . . 58

2.2.2 Basic principles of conventional TEM . . . 60
2.2.3 Basic principles of STEM . . . 61
2.2.4 Electron energy-loss spectroscopy . . . 63
2.2.4.1 Spectrum imaging: Data cube . . . 66
2.2.4.2 The need for high energy resolution . . . 67
2.2.4.3 EELS tomography . . . 68
2.2.5 Experimental details . . . 69
2.3 Processing of EELS data . . . 71
2.3.1 Gaussian fitting . . . 71
2.3.2 Blind Source Separation . . . 72
2.3.3 Vertex component analysis . . . 75
2.4 Boundary element method simulations . . . 76

3 Plasmonic Nanoengineering in Complex Metal Nanostructures: From Solid Nanocubes to Hollow Multi-walled Nanoboxes 77
3.1 Introduction . . . 78
3.2 Ag nanocube . . . 81
3.2.1 Local plasmonic properties . . . 81
3.2.2 Processing of plasmonic properties . . . 81
3.2.3 Boundary element method (BEM) simulations . . . 86
3.3 Ag@Au core-shell nanocube . . . 93
3.3.1 Local plasmonic properties . . . 93
3.3.2 Processing of plasmonic properties . . . 93
3.3.3 Boundary element method (BEM) simulations . . . 98
3.4 Pinholed AuAg nanobox . . . 102
3.4.1 Local plasmonic properties . . . 102
3.4.2 Processing of plasmonic properties . . . 102
3.4.3 Boundary element method (BEM) simulations . . . 106
3.5 Single-walled AuAg nanobox . . . 108
3.5.1 Local plasmonic properties . . . 108
3.5.2 Processing of plasmonic properties . . . 108
3.5.3 Boundary element method (BEM) simulations . . . 110
3.6 AuAg nanoframe . . . 116
3.6.1 Local plasmonic properties . . . 116
3.6.2 Processing of plasmonic properties . . . 116
3.6.3 Boundary element method (BEM) simulations . . . 118
3.7 Double-walled AuAg nanobox . . . 124
3.7.1 Local plasmonic properties . . . 124
3.7.2 Processing of plasmonic properties . . . 124
3.8 Sensing with the hollow nanostructures . . . 128
3.9 Summary and conclusions . . . 132

4 Plasmonic Nanoengineering in 1D Hollow Nanostructures: AuAg Nanotubes 135
4.1 Introduction . . . 136
4.2 Completely hollow AuAg nanotubes . . . 137
4.2.1 Structural characterization . . . 137

- 4.2.2 Local plasmonic properties . . . 138
- 4.2.3 Processing of plasmonic properties . . . 138
- 4.2.4 Boundary element method (BEM) simulations . . . 141
  - 4.2.4.1 BEM simulations on an Ag nanowire standing in vacuum 141
  - 4.2.4.2 BEM simulations on an Ag nanotube standing in vacuum 145
  - 4.2.4.3 BEM simulations on an Ag nanotube standing on substrate 151
  - 4.2.4.4 BEM simulations on an AuAg nanotube standing on substrate . . . 154
- 4.3 Hybrid AuAg nanotubes . . . 160
  - 4.3.1 Structural characterization . . . 160
  - 4.3.2 Local plasmonic properties . . . 163
  - 4.3.3 Processing of plasmonic properties . . . 164
- 4.4 Summary and conclusions . . . 168

5 Three-Dimensional Plasmonic Properties of Complex AuAg Nanostructures 171

- 5.1 Introduction . . . 172
- 5.2 Ag@Au core-shell nanocube . . . 175
  - 5.2.1 Structural characterization . . . 175
  - 5.2.2 Angle-resolved local plasmonic properties . . . 176
  - 5.2.3 Processing of 3D plasmonic properties . . . 178
- 5.3 Partially hollow AgAu nanocube . . . 184
  - 5.3.1 Structural characterization . . . 184
  - 5.3.2 Angle-resolved local plasmonic properties . . . 185
  - 5.3.3 Processing of 3D plasmonic properties . . . 186
- 5.4 Hollow AuAg nanoframe . . . 191
  - 5.4.1 Structural characterization . . . 191
  - 5.4.2 Angle-resolved local plasmonic properties . . . 192
  - 5.4.3 Processing of 3D plasmonic properties . . . 193
- 5.5 Plasmon coupling between two Ag@Au core-shell nanocubes . . . 197
  - 5.5.1 Angle-resolved local plasmonic properties . . . 197
  - 5.5.2 Processing of 3D plasmonic properties . . . 199
- 5.6 Plasmon coupling between an Ag@Au core-shell nanocube and an AuAg nanoframe . . . 205
  - 5.6.1 Angle-resolved local plasmonic properties . . . 205
  - 5.6.2 Processing of 3D plasmonic properties . . . 207
- 5.7 Summary and conclusions . . . 213

6 General Conclusions and Future Work 215

Bibliography 221

List of Figures

1.1 Dielectric function $\epsilon(\omega)$ of a free electron gas versus frequency (in plasma frequency ω_p units). Electromagnetic waves propagate without damping (lossless) only for the cases where ϵ is positive and real, whereas they are totally reflected when ϵ is negative (figure adapted from [7]) 7
1.2 Real and imaginary parts of the dielectric functions of Au (A) and Ag (B) for the free-electron model (black solid lines) and experimental dielectric data (red dotted lines). As seen in these graphs, the interband transitions limit the validity of the model (figure adapted from [2]). 9
1.3 A. Schematic of a metal film. B. Cross section along the dotted lines in A, where the positive ion cores are presented by + and the free electron gas is presented by gray background. C. shows the distribution of charges after a motion of the free electron gas, where the negative charges are uniformly displaced upward by a distance of "x". As a result of this motion, upper part of the metal film has a region of negative charges (with a surface charge density of -nex, ne being electron concentration) and the lower part of the film has a region of positive charges (with a surface charge density of +nex). An electric field $\mathbf{E} = 4\pi$ex is created inside the metal film. 10
1.4 A. Dispersion curves of the bulk plasmon (green-dashed line) and surface plasmon polariton(blue-dashed line), where the curve of light in vacuum is shown as a solid black line. Certain momentum provisions that allows coupling to light are shown by red dots and red-dashed lines. B shows the representative sketch of a mechanism of propagating surface plasmon polariton (figure adapted from [22]) 12
1.5 The schematic representations of the oscillations of surface charge densities, creating dipole localized surface plasmon modes, in spherical (upper) and elongated (lower) nanoparticles under applied $\mathbf{E}$. 16
1.6 Schematic representation of higher l-order modes for an elongated nanorod, showing the distribution of zero order, first order, second order, third order, fourth order and ninth order LSPR modes (figure adapted from [22]). 17
1.7 A. and B. Absorption spectra of the Au nanoparticles with various sizes, where the experimental values (open circles) are compared with the Mie theory simulations (solid lines) in A. C. The shift of the $\Gamma_{1/2}$ (indicated in A) versus the nanoparticle diameter. D. Change in the wavelength versus nanoparticle sizes defining the intrinsic and extrinsic regions (figure adapted from [33] and [43]. 19
1.8 A. Photographs of solutions at various times during a typical synthesis of Au nanodecahedra with size control. B. UV-Vis spectra showing the absorption changing by size. C. TEM micrographs of Au nanodecahedra (figure adapted from [34]). 19

1.9 A. Absorption spectra of different Au nanorods with aspect ratios between 1.94 and 3.08, where the shift to higher wavelengths with the increasing aspect ratio is clearly revealed. B, C and D are TEM micrographs of different Au nanorods with aspect ratios of ∼2.4, ∼2.6 and ∼3.8, respectively. Insets in the TEM micrographs are the photographs of the solutions revealing the change in color by aspect ratio of the nanorods (figure adapted from [29] and [39]). 20

1.10 A. Different silver and gold nanostructures presenting their plasmon resonances in a wide range of spectrum from UV to mid infrared (figure reproduced from [60]). B. Extinction spectra of various polyhedral Au nanostructures (figure adapted from [57]). Note that the colors in the extinction spectra are the same as the colored squared around the structures, i.e. spectrum corresponding to the cuboctahedron is green. C. Plasmon resonance wavelengths for Ag spheres, pentagons and triangles with various sizes (figure adapted from [53]). 21

1.11 Mie calculations for idealized void/Ag (upper) and void/Au (lower) spherical systems with a total diameter of 50 nm, where the shell thickness varied between 2.5 nm and 22.5 nm. 22

1.12 TEM micrographs of Au nanostructures: (A) large nanorod, (B) nanobipyramid, (C) oxidized nanobipyramid, (D) oxidized nanorod, (E) dog-bone-like nanorod, (F) peanut-like nanorod and (G) small nanorod. Their corresponding electric field enhancement contours (at the logaritmic scale) are presented in the lower row. The extinction spectra of the nanostructures are shown on the right (figure adapted from [56]). 23

1.13 (Upper row) Photographs of solutions at different stages of galvanic replacement reaction, where Ag nanocubes (far left) are used as templates to synthesize AuAg nanocages (far right). (Middle row) TEM micrographs of Ag nanocubes and AuAg nanoscages. (Lower row) UV-Vis spectra obtained from the different stages of the reaction, where the amount of Au increased from left to right. Colored arrows indicate the photographs and UV-Vis spectra corresponding to the initial Ag nanocubes and final AuAg nanocages (figure adapted from [65]). 24

1.14 UV-Vis spectra of several AuAg alloy nanoparticles with different compositions, along with the TEM micrographs taken from the $Au_{0.25}Ag_{0.75}$ and $Au_{0.75}Ag_{0.25}$ nanoparticles revealing the size homogeneity within and between the samples. Note that the AuAg alloy nanoparticles have similar sizes of ∼6 nm for all compositions (figure adapted from [79]). 25

1.15 Absorption spectra taken from ∼13 nm $Au_{0.5}Ag_{0.5}$ nanoparticles formed an alloy (in red) and mixing Au and Ag nanoparticles (in blue) (figure adapted from [74]. 26

1.16 A. Comparison of the extinction cross-sections of 20 nm Au nanospheres and ellipsoids with aspect ratio 2 in different dielectric environment (figure reproduced [82]). B. Resonant Rayleigh scattering spectra obtained from a single Ag nanoprism in various solvent environments (figure adapted from [83]). 26

1.17 A. Scattering spectra of a 60 nm Ag nanocube in vacuum (in black) and on a glass substrate (in red). B. Electric field enhancement maps of two resonances labeled as I and II in A. C. Schematics of charge distributions showing the primitive dipolar (D^o) and quadrupolar (Q^o) modes. D. Energy diagram and schematic of the substrate effect leading the formation of hybridized bonding D and anti-bonding Q modes (figure adapted from [91]. . . . 27

1.18 A. Representative SEM micrograph of Au nanodisk with a gap ∼12 nm. B. DDA-simulated extinction efficiency for varying interparticle gap for parallel incident light polarization direction (figures adapted from [96]). C. Simulated electric field contours of bowtie nanoantennas with parallel and perpendicular polizations. D. Raman spectra and E. enhancement factor for varying gap size between nanoantennas (figure adapted from [105]). . . . 29

1.19 A. Schematic energy-level diagram illustrating the plasmon hybridization mechanism in metal nanoshells as a result of the interaction between the sphere and cavity plasmons. Anti-symmetrically coupled, anti-bonding, mode (ω_+) and symmetrically coupled, bonding, mode (ω_-) are shown (reproduced from [115]). B. Extend of the hybridization for thick (upper) and thin (lower) metallic shells revealing that the hybridization is much higher for the thin metallic shell (figure adapted from [116]). . . . 30

1.20 Spherical dielectric *nanovoid* in a homogeneous metallic body. . . . 31

1.21 A. Geometry of a nanomatryushka, consisting of a spherical Au nanoparticle/void/Au nanoshell system. B. Induced electric field distribution for the two modes located at 1.81 eV (top) and 2.87 eV (bottom). Distances between the components (shown with colored arrows in A) increase from left to right, which are given in parenthesis with colors corresponding to the color of the arrows. C. Plasmon hybridization diagram, where the NC is nanocore, NS is nanoshell, NB is nonbonding and NM is nanomatryushka. D. Schematic surface charge distributions for the modes located at 1.81 eV (left) and 2.87 eV (rigt) (figure adapted from [119]). . . . 33

1.22 A. Schematics of colorimetric detection of nucleic acid sequences: DNA-Au nanoparticle probes are hybridized to a DNA target in solution and deposited onto a glass substrate, which is then illuminated with white light. The Au nanoparticles having 40-50 nm diameter scatter green light, whereas completed DNA-Au nanoparticle probes scatter yellow to orange light (figure reproduced from [134]). B. Bovine serum albumin (BSA) sensing with Au nanodimers, where sensing enhancement versus the gap size between dimers are shown for different BSA coverage amounts. On the right, schematics of BSA molecules located at the interparticle gap (figure adapted from [101]). . . . 35

1.23 A. DDA simulated plasmon resonance maximum peak positions for Au nanoframes (NF) with different edge lengths and wall thicknesses. B. DDA simulated extinction spectra of 40 nm Au NFs with 7.2 nm thick walls in various environments. C. DDA simulated extinction spectra of 90 nm Au NFs with 21.6 nm thick walls in various environments (figure adapted from [67]). . . . 36

1.24 A. Schematics of cancer cell targeting and spectroscopic detection by using antibody-conjugated SERS where Au nanoparticles stabilized with thiol-polyethyleneglycol (thiol-PEG) are used as plasmonic component. B. SERS spectra obtained in-vivo from the EGFR-positive cancer cells and EGFR-negative cancer cells along with the control data and the standard tag spectrum (figure adapted from [152]). 37

1.25 A. Schematic of the tunneling-controlled TERS setup. B. STM topograph sub-monolayered H_2TBPP molecules (the inset is the chemical structure of a single molecule). C. TERS spectra obtained for different conditions (figure adapted from [156]). 38

1.26 Different plasmonic light-trapping geometries for various solar cells. A. Three different designs for thin-film solar cells where the plasmonic nanostructures are located at the top surface of the cell, embedded in the semiconductor, and located at the metal/semiconductor interface. B. So-called plasmonic tandem geometry where the semiconductors with different bandgaps are stacked on top of each other, separated by plasmonic metal contact layer. C. Plasmonic quantum-dot solar cell with a metal/insulator/metal SPP waveguide. D. Optical nanoantenna array in organic solar cells. E. Solar cells enhanced by cavity plasmons of a metal film where the voids are filled with semiconductors. (Figure adapted from [128].) 39

1.27 A. (Left) Schematic representation of light trapping due to LSPR of Au nanoparticles in an organic solar cell. (Right) Schematic of the local enhancement of the electromagnetic field, note that the plasmon field decays exponentially with increasing distances from Au nanoparticles. B. PL decay profiles of the pristine P3HT/PCMB blend sample and the plasmonic sample, where the schematic of charge transfer process is shown as inset. C. Schematic of the interplay between LSPR and the excitons where the resulting interactions enhances the rate of exciton dissociation, thus, reduces the exciton recombination (figure adapted from [168]). . . . 40

1.28 A. Schematics of heat generation by photothermal effect (figure reproduced from [169]). B. Shape dependent photohermal stability of various Au nanostructures and their related applications in nanomedicine (figure reproduced from [170]). 41

1.29 Atlas of spatially-resolved spectroscopy techniques used in plasmon resonance measurements, organized according to their spatial and energy resolution (figure reproduced from [179]). 43

1.30 A. SEM micrograph of a 725 nm long Au nanowire on a Si substrate (scale bar is 250 nm). B. CL images of the Au nanowire at wavelengths of 592 nm, 640 nm and 730 nm, showing different plasmon modes (figure reproduced from [191]). C. CL spectra from the tip and edge of a 80 nm thick truncated tetrahedral (TT) Au nanparticle. Insets show the SEM micrograph and CL emission maps at 530 nm (edge mode) and at 604 nm (tip mode), scale bars are 200 nm (figure reproduced from [197]). 45

1.31 A. Schematics of the crescents with orientations of 90^o, 120^o and 150^o where B. shows their corresponding SEM micrographs. Scale bar is 100 nm for all micrographs. C. CL spectroscopic tomography results at different wavelengths from 470 nm to 900 nm, where the intensities are normalized. 46

1.32 EELS (blue) and CL (red) spectra obtained from the tip (A) and edge (B) of a 60 nm Au nanoprism with a 30 nm thickness deposited on graphene. 46
1.33 A. EEL spectra obtained from the tip, edge and center of a 70 nm Ag nanoprism along with their plasmon intensity and energy (only for the tip mode) maps (figure reproduced from [207]). B. STEM micrograph of a Au nanorod, the average spectrum revealing the presence of two plasmon resonances at 1.70 eV and 2.40 eV and the plasmon intensity maps of these modes (figure reproduced from [205]). 47
1.34 A. EELS spectra of two $\sim$80 nm Au nanoprisms separated by a 3 nm gap and B is the EELS spectra of two nanoprisms connected by a 4 nm bridge. C. and D. are simulated charge distributions, experimental EELS maps and simulated field distributions for various plasmon modes observed for separated and connected nanoprisms, respectively (figure adapted from [221]). 48
1.35 A. EELS spectra obtained from the spherical Ag nanoparticles ranging from 11 nm to 1.7 nm in diameter (shown in the STEM micrographs). The e-beam was placed onto the edge of nanoparticles in order to excite only the surface plasmons. B. Plot of the surface plasmon resonance energy versus nanoparticle diameter (inset shows the bulk plasmon resonance energies). C. Comparison of the experimentally observed results with the simulated results obtained by DFT-derived quantum permittivity model, where the two results are overlaid. The trend suggested by the classical approach is given in white dotted line. (figure adapted from [209]). 49
1.36 A. LSPR spectral components ($\alpha, \beta, \gamma, \delta, \epsilon$) obtained by applying non-negative matrix factorization (NMF) to the EELS datasets at different tilt angles. B. 3D visualization of each spectral components and their overlay (figure adapted from [90]). 50

2.1 A block diagram of a modern day TEM with STEM and spectroscopy capabilities (figure reproduced from [230]). 57
2.2 A. Different type of signals generated when an indicent beam interacts with a thin specimen. The techniques used in this thesis manuscript are written in parenthesis after the related signal. In the lower row, a classical view of electron scattering by a single carbon atom is shown. B. Elastic scattering. C and D are inelastic scattering by inner- and outer-shell electrons, respectively. 59
2.3 A. Ray paths in image mode (figure reproduced from [230]). Ray diagrams showing the use of objective aperture to produce bright field (B) and dark field (C) images along with the schematics of diaphgrams on the viewing screen (figures reproduced from [231]). D. Ray paths in selected area diffraction mode (figure reproduced from [230]). 61
2.4 A. HRTEM image obtained from a AuAg nanotube. B. Detail of the red squared region and C. its corresponding power spectra. 62
2.5 A. A schematic representation of a STEM, showing the basic elements and B. schematics of different STEM detectors based on the scattering angle. 62
2.6 Schematic diagram of a parallel collection of the energy-loss spectrum, so-called parallel EELS (PEELS)system (figure reproduced from [231]). . 64

2.7 A typical EELS obtained from C (intensity is in logarithmic scale). Three different regions of zero-loss peak (red), low-loss region (green) and core-loss region (blue) are indicated with colored bars above the spectrum. . . 65

2.8 Schematic representations of different EELS acquisition techniques: A. single spectrum, B. spectrum line and C. spectrum image, along with the corresponding cartesian axes of energy (E), x and y. 66

2.9 Schematic representation of electron tomography: A tilt series of a 3D object are acquired and then back-projected to obtain 3D volume (figure reproduced from [260]). 68

2.10 A. Background subtracted EELS SI obtained from the single-walled AuAg nanobox. B. Summed EELS spectrum over the SI where a Gaussian peak is fitted to the main plasmon peak. C. Center of the Gaussian fitting, which is used as plasmon energy distribution map. D. Amplitude of the Gaussian fitting, which is used as plasmon intensity distribution map. In the lower row of C and D, center and amplitude maps are shown in temperature color scale. 72

2.11 Scree plot showing the variance of the components obtained by applying the weighted PCA on the EELS data of the single-walled AuAg nanobox. 74

3.1 A. Optical and structural evolution of Ag nanocubes to double-walled AuAg nanobox. B. HAADF STEM micrographs and EDX maps of different stages of the evolution in A (adopted from [69]). 79

3.2 HRTEM micrograph of a double-walled AuAg nanobox showing the single crystalline structure of the nanobox. Details of the red, green and blue squared regions and their corresponding power spectra are also presented. 80

3.3 A. HAADF STEM micrograph of a 55 nm Ag nanocube with rounded corners. B. Selected area EEL spectra of the upper left corner, upper edge/face and center (areas are indicated in HAADF STEM micrograph, which are 5 pixel by 5 pixel) 81

3.4 A. Plasmon energy maps of the Ag nanocube, obtained by fitting a Gaussian between the energy ranges of 2.4 - 3.0 eV, 2.7 - 3.3 eV, 3.2 - 3.7 eV and 3.6 - 3.9 eV and B. their corresponding plasmon intensity maps. Notice that the colorcode and the scale is different for the instensity map of the bulk mode, where white pixels are the pixels with lowest intensity. . 83

3.5 Blind source separation (BSS) analysis of the Ag nanocube: Spectra of the 8 components and their corresponding abundance maps. 83

3.6 Vertex component analysis (VCA) of the Ag nanocube: Spectra of the 8 components and their corresponding abundance maps. 85

3.7 BEM simulations of a 50 nm Ag nanocube in vacuum: A. Simulated selected area EEL spectra of the Ag nanocube from the corner, edge and center. B. Simulated plasmon maps for LSPRs at 2.99 eV, 3.07 eV, 3.17 eV, 3.40 eV, 3.70 eV and 3.80 eV. 87

3.8 BEM simulations of Ag nanocube: Charge distribution maps (A) and their corresponding field maps (B) of different plasmon modes located at 2.99 eV, 3.07 eV, 3.17 eV, 3.40 eV, 3.70 eV and 3.80 eV. Maps are mostly obtained by a beam excitation at the edge except the one at 3.07 eV, which is obtained by a corner beam excitation, and the one at 3.80 eV (bulk mode), which is obtained by a center beam excitation. 88

3.9 Effect of rounded corners on the LSPR properties of Ag nanocubes: Nanocube with perfect corners and nanocubes with rounded corners with radii of 2 nm, 5 nm and 10 nm. Corner excitations are in blue, edge excitations are in red and center excitations are in green for all the EEL spectra presented on the right. 89
3.10 BEM simulations of a 50 nm Ag nanocube on 15 nm thick Si_3N_4 substrate: Simulated selected area EEL spectra of the Ag nanocube of the corner, edge and center. 90
3.11 BEM simulations of a 50 nm Ag nanocube on 15 nm thick Si_3N_4 substrate showing field maps of different proximal and distal plasmon modes. 90
3.12 BEM simulated local plasmon responses of 50 nm Ag nanocubes with sharp corners (upper) and rounded corners (lower) on SiN_x substrate. Dashed lines show the results obtained by BEM simulations and continuous lines show the results of BEM simulations after taking the experimental broadening, i.e. energy resolution, into account. 91
3.13 Selection of BEM simulated plasmon maps obtained from Ag nanocubes with rounded corners, radius = 15 nm, revealing the merging of corner and other modes. 92
3.14 A. HAADF STEM micrograph of a 51 nm Ag@Au core-shell nanocube. B. Selected area EEL spectra of the upper left and upper right corners, upper edge and center (areas are indicated in HAADF STEM micrograph, which are 5 pixel by 5 pixel). 93
3.15 A. Plasmon energy maps of the Ag@Au core-shell nanocube, obtained by fitting a Gaussian between the energy ranges of 1.8 - 2.6 eV, 2.3 - 3.3 eV, 3.2 - 3.7 eV and 3.5 - 3.9 eV and B. their corresponding plasmon intensity maps. White pixels in the energy maps are out of fitting parameters. Notice that the plasmon intensity map between 3.5 and 3.9 eV has a different color code, where white pixels are the pixels with lowest intensity. 94
3.16 HAADF STEM micrograph of the Ag@Au core-shell nanocube obtained simultaneously during EELS acquisition and its colored composite with the plasmon energy map for the bulk plasmon mode of Ag. Pixel size, which corresponds to the spatial resolution of the EELS maps, is 1.54 nm. 95
3.17 BSS analysis of the Ag@Au core-shell nanocube: Spectra of the 5 components and their corresponding abundance maps. 96
3.18 VCA analysis of the Ag@Au core-shell nanocube: Spectra of the 5 components and their corresponding abundance maps. 97
3.19 A. BEM simulated local EEL spectra of a 50 nm Au nanocube B. and C. are charge and field maps of different plasmon modes, respectively. 98
3.20 A. BEM simulated local EEL spectra of a 50 nm Au nanocube standing on a 15 nm thick Si_3N_4 substrate. Charge (B) and field (C) maps of two proximal modes arised due to intereaction with the substrate. 99
3.21 A. Dielectric function of Ag and Au, where the solid lines are for the real parts of the dielectric function and the dashed lines are for the imaginary parts. B. DDA simulated EEL spectra of bulk plasmon resonances of Ag and Au structures. 100
3.22 A. BEM simulated EEL spectra from the corner, edge and center of a 50 nm Ag@Au core-shell nanocube with a 1.5 nm shell thickness. B. Simulated plasmon maps of different proximal and distal modes. 101

3.23 A. HAADF STEM micrograph of a 51 nm pinholed AuAg nanobox. B. Selected area EEL spectra of the upper left and lower right corners, upper edge, center hole and bulk of the pinholed nanobox (areas are indicated in HAADF STEM micrograph, which are 5 pixel by 5 pixel). 102
3.24 A. Plasmon energy maps of the pinholed AuAg nanobox, obtained by fitting a Gaussian between the energy ranges of 2.1 - 2.5 eV, 2.4 - 3.2 eV, 3.2 - 4.0 eV and 3.5 - 3.9 eV and B. their corresponding plasmon intensity maps. White pixels in the energy maps are out of fitting parameters. Notice that the plasmon intensity map between 3.5 and 3.9 eV has a different color code, where white pixels are the pixels with lowest intensity 103
3.25 BSS analysis of the pinholed AuAg nanobox: Spectra of the 5 components and their corresponding abundance maps. 104
3.26 VCA analysis of the pinholed AuAg nanobox: Spectra of the 5 components and their corresponding abundance maps. 105
3.27 BEM simulated EEL spectra revealing the effect of void size for Ag nanostructures from 50 nm Ag nanocubes to 50 nm Ag nanobox with 2 nm thick walls. 106
3.28 A. HAADF STEM micrograph of a 50 nm single-walled AuAg nanobox with ∼ 7 nm wall thickness. B. Selected area EEL spectra of the upper left and lower right corners, upper edge, center of the nanobox (areas are indicated in HAADF STEM micrograph, which are 5 pixel by 5 pixel). . . 108
3.29 A. Plasmon energy map of the single-walled AuAg nanobox, obtained by fitting a Gaussian between the energy range between 1.9 and 2.4 eV and B. its corresponding plasmon intensity map. 109
3.30 BSS analysis of the single-walled AuAg nanobox: Spectra of the 3 components and their corresponding abundance maps. 110
3.31 VCA analysis of the single-walled AuAg nanobox: Spectra of the 3 components and their corresponding abundance maps. 111
3.32 BEM simulations of a 50 nm single-walled AuAg nanobox with sharp corners: Model for the simulations and simulated EEL spectra from the corner, edge and center of the nanobox. 112
3.33 BEM simulations of field maps of 50 nm single-walled AuAg nanobox with sharp corners, obtained from the plasmon resonances at 1.94 eV, 2.16 eV, 2.44 eV and 2.62 eV. 113
3.34 BEM simulations of 50 nm single-walled AuAg nanobox showing field maps of different plasmon modes in 3D. 113
3.35 BEM simulations of a 50 nm single-walled AuAg nanobox with smooth corners: Model for the simulations and simulated EEL spectra from the corner, edge and center of the nanobox. 114
3.36 BEM simulations of a 50 nm single-walled AuAg nanobox with smooth corners: field maps of the plasmon resonances at 2.16 eV, 2.28 eV, 2.50 eV and 2.74 eV. 115
3.37 A. HAADF STEM micrograph of a 48 nm AuAg nanoframe with ∼ 7 nm wall thickness. B. Selected area EEL spectra of the upper left corner, upper and lower edges and center of the nanoframe (areas are indicated in HAADF STEM micrograph, which are 5 pixel by 5 pixel). 116
3.38 A. Plasmon energy map of the AuAg nanoframe, obtained by fitting a Gaussian between the energy range between 1.6 and 2.1 eV and B. its corresponding plasmon intensity map. 117

3.39 BSS analysis of the AuAg nanoframe: Spectra of the 3 components and their corresponding abundance maps. 117
3.40 VCA analysis of the AuAg nanoframe: Spectra of the 3 components and their corresponding abundance maps. 119
3.41 BEM simulated EEL spectra from the corner, edge and center of a 48 nm AuAg nanoframe as shown in the upper left model. 120
3.42 BEM simulations of a 48 nm AuAg nanoframe: field maps of the plasmon resonances at 1.047 eV, 1.13 eV, 1.43 eV and 1.83 eV. 120
3.43 BEM simulated EEL spectra from the corner, edge and center of a 48 nm AuAg nanoframe which is more similar to the experimentally investigated nanoframe with its partially filled faces and rounded corners as shown in the upper left model. 121
3.44 BEM simulations of a 48 nm AuAg nanoframe with partially filled faces and smooth corners: field maps of the plasmon resonances at 1.558 eV, 1.685 eV, 1.94 eV, 2.237 eV, 2.407 eV and 2.748 eV. 122
3.45 BEM simulated 3D field maps of the plasmon resonances located at 1.558 eV, 1.685 eV and 1.94 eV in the realistic AuAg nanoframe: A, C and E are plasmon fields excited by a corner beam and B, D and F are plasmon fields excited by an edge beam. 123
3.46 A. HAADF STEM micrograph of a 50 nm double-walled AuAg nanobox. B. Selected area EEL spectra of the upper left corner, upper edge and center of the double-walled nanobox (areas are indicated in HAADF STEM micrograph, which are 5 pixel by 5 pixel). 124
3.47 A. Plasmon energy map of the double-walled AuAg nanobox, obtained by fitting a Gaussian between the energy range between 1.6 and 2.4 eV and B. its corresponding plasmon intensity map. 125
3.48 BSS analysis of the double-walled AuAg nanobox: Spectra of the 3 components and their corresponding abundance maps. 125
3.49 VCA analysis of the double-walled AuAg nanobox: Spectra of the 3 components and their corresponding abundance maps. 126
3.50 A. Schematic representation of the primary and secondary protein conjugation processes with spherical Au nanoparticles (left) and single-walled AuAg nanoboxes (right). B. UV-Vis spectra of the unconjugated (black line) spherical Au nanoparticles (left) and single-walled AuAg nanoboxes (right). After the conjugation with BSA (red line) and after the further addition of the Ab (blue line). Insets are details showing the red shift after the binding of the proteins. C. Comparison of the wavelength shift between spherical Au nanoparticles and single-walled AuAg nanoboxes after the first NP-protein interaction and secondary protein-Ab interaction.129
3.51 BEM simulated sensitivity of spherical Au nanoparticles, Au nanocubes, Au nanoboxes and Au nanoframes, against the change in the surrounding medium. Blue spectra are in water with a refracive index n = 1.33, green spectra is an environment with a refractive index of n = 1.39, red spectra are the case for the medium with a refractive index of n = 1.45. 131

3.52 Structural and LSPR evolution of the AuAg nanostructures. A. Structural sketches and corresponding solution colors of Ag nanocube, Ag@Au core-shell nanocube, pinholed AuAg nanobox, single-walled AuAg nanobox, AuAg nanoframe and double-walled AuAg nanobox. B. HAADF STEM micrographs of the nanostructures where SI EELS have been acquired, from Ag nanocube to double-walled AuAg nanobox (scale bars = 50 nm). C. Summed background subtracted EEL spectra collected over the nanostructures showing the evolution of localized surface plasmon resonances with structural changes. 133

4.1 HAADF STEM and SEM micrographs of AuAg nanotubes, revealing the hollow and multitwinned nature of the nanotubes. 137
4.2 HRTEM micrographs of a completely hollow AuAg nanotube, showing the crystallinity of the nanotubes. 138
4.3 A. HAADF STEM micrograph of a AuAg nanotube, which is 84 nm in diameter and 665 nm in length. B. Background subtracted selected area EEL spectra of different locations marked in C, which is the EELS SI taken from the white rectangle in A. 139
4.4 Plasmon energy maps (left) and their corresponding intensity maps (right) obtained by fitting a Gaussian to the energy ranges between 0.45-0.6 eV, 0.8-1.1 eV, 1.1-1.5 eV, 1.5-2.3 eV and 2.3-3.1 eV. White pixels in the energy maps are parameters out of fitting. 140
4.5 VCA of the completely hollow AuAg nanotube: Plasmon components and their corresponding abundance maps. 140
4.6 A. Structural model of the BEM simulated Ag nanowire with a length of 665 nm and a diameter of 84 nm. B. Simulated local EEL spectra obtained at the tip, at a quarter of the length (at ∼ 166 nm) and at the center (at 332.5 nm) of the Ag nanowire. Note that the nanowire is standing in vacuum. 141
4.7 BEM simulated plasmon maps of the Ag nanowire: Maps of 12 different modes, located at 0.314 eV, 0.713 eV, 1.321 eV, 1.891 eV, 2.385 eV, 2.746 eV, 2.993 eV, 3.164 eV, 3.278 eV, 3.525 eV, 3.677 eV and 3.81 eV, are presented. 143
4.8 BEM simulated plasmon maps of the Ag nanowire obtained by the beam incident on the pentagonal cross-section: Maps of 12 different modes, located at 0.314 eV, 0.713 eV, 1.302 eV, 1.891 eV, 2.385 eV, 2.746 eV, 2.993 eV, 3.164 eV, 3.278 eV, 3.468 eV, 3.658 eV and 3.81 eV, are presented. Note that 3 of the modes located at 1.302 eV, 3.468 and 3.658 eV have slightly different energies than those presented in Fig. 4.7. 144
4.9 A. Structural model of the BEM simulated Ag nanotube with a length of 665 nm and a diameter of 84 nm. B. Simulated local EEL spectra obtained at the tip, at a quarter of the length (at ∼ 166 nm) and at the center (at 332.5 nm) of the Ag nanotube. Note that the nanotube is standing in vacuum. 146
4.10 BEM simulated plasmon maps of the Ag nanotube: Maps of 12 different modes, located at 0.352 eV, 1.036 eV, 1.53 eV, 1.929 eV, 2.214 eV, 2.461 eV, 2.632 eV, 2.708 eV, 2.803 eV, 2.898 eV, 3.069 eV and 3.297 eV, are presented. 147

4.11 BEM simulated plasmon maps of the Ag nanotube obtained by the beam incident on the pentagonal cross-section: Maps of 12 different modes, located at 0.352 eV, 1.036 eV, 1.53 eV, 1.929 eV, 2.233 eV, 2.461 eV, 2.632 eV, 2.708 eV, 2.803 eV, 2.879 eV, 3.126 eV and 3.305 eV, are presented. Note that energy of some of the modes are slightly different than those presented in Fig. 4.10. 149

4.12 A. Structural model of the BEM simulated Ag nanotube with a length of 665 nm and a diameter of 84 nm, with 10 nm thick walls, standing on a 15 nm thick Si_3N_4 substrate. B. Simulated local EEL spectra obtained at the tip, at a quarter of the length (at $\sim$ 166 nm) and at the center (at 332.5 nm) of the Ag nanotube. 151

4.13 BEM simulated plasmon maps of the Ag nanotube standing on a Si_3N_4 substrate: Maps of 12 different modes, located at 0.523 eV, 1.017 eV, 1.397 eV, 1.701 eV, 1.891 eV, 2.005 eV, 2.062 eV, 2.252 eV, 2.366 eV, 2.594 eV, 2.708 eV and 2.765 eV, are presented. 153

4.14 A. Structural model of the BEM simulated AuAg nanotube with a length of 665 nm and a diameter of 84 nm, with 10 nm thick walls, standing on a 15 nm thick Si_3N_4 substrate. B. Simulated local EEL spectra obtained at the tip, at a quarter of the length (at $\sim$ 166 nm) and at the center (at 332.5 nm) of the AuAg nanotube. 155

4.15 BEM simulated plasmon maps of the AuAg nanotube standing on a Si_3N_4 substrate: Maps of 8 different modes, located at 0.504 eV, 0.979 eV, 1.359 eV, 1.625 eV, 1.891 eV, 2.139 eV, 2.29 eV and 2.385 eV, are presented. . . 157

4.16 BEM simulated plasmon maps of the AuAg nanotube obtained by the beam incident on the pentagonal cross-section: Maps of 8 different modes, located at 0.504 eV, 0.979 eV, 1.359 eV, 1.625 eV, 1.891 eV, 2.139 eV, 2.29 eV and 2.385 eV, are presented. 158

4.17 BEM simulated 3D EM field maps of the different plasmon peaks of the AuAg nanotube, which are located at 0.55 eV, 0.99 eV, 1.36 eV, 1.62 eV, 1.89 eV, 2.14 eV, 2.29 eV and 2.385 eV. These maps are obtained with a beam excitation from the near-edge (x = 0 nm, y = -10 nm), except the ones at 2.14 eV and 2.385 eV, which are obtained with a beam excitation at the center of the nanotube. 159

4.18 Bright field STEM and HAADF STEM micrographs taken from the hybrid AuAg nanotubes, revealing the presence of several micron long hybrid nanotubes formed by arrays of solid and hollow parts. 160

4.19 HRTEM micrographs taken from a hybrid AuAg nanotube, showing the crystallinity and sharp interfaces between the solid and hollow parts of the nanotubes. 161

4.20 HAADF STEM micrograph of a hybrid AuAg nanotube with a $\sim$ 90 nm diameter. EDX maps of the red rectangular region: Simultaneous HAADF STEM, elemental Ag (in red) and Au (in green) maps and their composite. 161

4.21 HAADF STEM micrograph of a hybrid AuAg nanotube with a $\sim$ 88 nm diameter. EDX maps of the red rectangular region: Simultaneous HAADF STEM, elemental Ag (in red) and Au (in green) maps and their composite. 162

4.22 HAADF STEM micrograph of a hybrid AuAg nanotube with a diameter of 88 nm. Inset shows the EDX line scan results (intensities are arbitrary units and normalized) obtained through the red arrow. 162
4.23 A. HAADF STEM micrograph of a hybrid AuAg nanotube, which is 89 nm in diameter and 1.24 μm in length. B. Background subtracted selected area EEL spectra of different locations marked in C, which is the EELS SI taken from the white rectangle in A 163
4.24 Plasmon energy maps (left) and their corresponding intensity maps (right) obtained by fitting a Gaussian to the energy ranges between 0.6-0.75 eV, 0.9-1.1 eV, 1.1-1.5 eV, 1.45-1.65 eV, 1.7-2.7 eV, 2.9-3.6 eV, and 3.5-3.9 eV. White pixels in the energy maps are out of fitting parameters. 165
4.25 VCA of the hybrid AuAg nanotube: Plasmon components and their corresponding abundance maps. 166

5.1 HAADF STEM micrographs of different AuAg nanostructures that 3D EELS maps are obtained: +40^o, 0^o, -40^o tilts of a solid Ag@Au core-shell nanocube, a partially hollow AuAg nanocube, an AuAg nanoframe, two Ag@Au core-shell nanocubes standing with $\sim$ 22 nm separation and an Ag@Au core-shell nanocube and an AuAg nanoframe standing with $\sim$ 14 nm separation. 174
5.2 High resolution HAADF STEM micrograph of a 63 nm Ag@Au core-shell nanocube. STEM-EDX maps of Ag (in green) and Au (in red). Detail of the upper right corner with two different focus revealing the shell in different focus. 175
5.3 HAADF STEM micrographs (left) of the +40^o, 0^o, -40^o tilts of a solid Ag@Au core-shell nanocube and background subtracted local EEL spectra (right) of different locations shown by black, blue, green and red squares. Note that the color of each spectra corresponds to the color of the location indicated in the HAADF STEM micrographs. 176
5.4 Series of HAADF STEM micrographs of the Ag@Au core-shell nanocube obtained simultaneously with the EELS SI at different tilt angles between +55^o and -60^o with different intervals. 179
5.5 Spectra corresponding to 4 different components obtained by VCA and their corresponding abundance maps for different tilts. Intensity of the abundance maps are normalized within each component. 180
5.6 A. Spectrum of the component I in Fig. 5.5 and its corresponding abundance maps for all tilt angles are shown in B. 180
5.7 A. Spectrum of the component II in Fig. 5.5 and its corresponding abundance maps for all tilt angles are shown in B. 181
5.8 A. Spectrum of the component III in Fig. 5.5 and its corresponding abundance maps for all tilt angles are shown in B. 181
5.9 A. Spectrum of the component IV in Fig. 5.5 and its corresponding abundance maps for all tilt angles are shown in B. 182
5.10 A. Spectrum of the component corresponding to the bulk plasmon resonance of Ag at $\sim$3.8 eV and its abundance maps for all tilt angles are shown in B. 183
5.11 High resolution HAADF STEM micrograph of a 57 nm partially hollow AgAu nanocube. STEM-EDX maps of Ag (in green) and Au (in red). Detail of the centeral hollow part. 184

5.12 HAADF STEM micrographs (left) of the +40^o, 0^o, -40^o tilts of a 50 nm partially hollow AgAu nanocube and background subtracted local EEL spectra (right) of different locations shown by black, blue, green, orange and red squares. Note that the color of each spectra corresponds to the color of the location indicated in the HAADF STEM micrographs. 185
5.13 Series of HAADF STEM micrographs of the partially hollow AgAu nanocube obtained simultaneously with the EELS SI at different tilt angles between +60^o and -40^o with different intervals. 187
5.14 Spectra of 4 different components of the partially hollow AgAu nanocube, obtained by VCA and their corresponding abundance maps for different tilts. Intensity of the abundance maps are normalized within each component. 187
5.15 A. Spectrum of the component I in Fig. 5.14 and its corresponding abundance maps for all tilt angles are shown in B. 188
5.16 A. Spectrum of the component II in Fig. 5.14 and its corresponding abundance maps for all tilt angles are shown in B. 189
5.17 A. Spectrum of the component III in Fig. 5.14 and its corresponding abundance maps for all tilt angles are shown in B. 189
5.18 A. Spectrum of the component IV in Fig. 5.14 and its corresponding abundance maps for all tilt angles are shown in B. 190
5.19 Atomic resolution HAADF STEM micrograph ∼ of a 53 nm hollow AuAg nanoframe. STEM-EDX maps of Ag (in green) and Au (in red). Details of upper right and lower left corners. 191
5.20 HAADF STEM micrographs (left) of the +40^o, 0^o, -40^o tilts of a 47 nm hollow AuAg nanoframe and background subtracted local EEL spectra (right) of different locations shown by black, blue, and red squares. Note that the color of each spectra corresponds to the color of the location indicated in the HAADF STEM micrographs. 192
5.21 Series of HAADF STEM micrographs of the hollow AuAg nanoframe obtained simultaneously with the EELS SI at different tilt angles between +60^o and -55^o with different intervals. 194
5.22 Spectra of 3 different components of the hollow AuAg nanoframe, obtained by VCA and their corresponding abundance maps for different tilts. Intensity of the abundance maps are normalized within each component. 194
5.23 A. Spectrum of the component I in Fig. 5.22 and its corresponding abundance maps for all tilt angles are shown in B. 195
5.24 A. Spectrum of the component II in Fig. 5.22 and its corresponding abundance maps for all tilt angles are shown in B. 196
5.25 A. Spectrum of the component III in Fig. 5.22 and its corresponding abundance maps for all tilt angles are shown in B. 196
5.26 HAADF STEM micrographs (left) of the +40^o, 0^o, -40^o tilts of a 59 nm and a 53 nm Ag@Au core-shell nanocubes standing with a separation of ∼22 nm. On the right, the background subtracted local EEL spectra of different locations shown by black, blue, dark green, green, turquoise, orange, violet, purple and red squares are shown. Note that the color of each spectra corresponds to the color of the location indicated in the HAADF STEM micrographs. 197

5.27 Series of HAADF STEM micrographs for the two Ag@Au core-shell nanocubes obtained simultaneously with the EELS SI at different tilt angles between +60^o and -50^o with different intervals. 199
5.28 Spectra of 6 different components of the Ag@Au core-shell nanocubes, obtained by VCA and their corresponding abundance maps for different tilts. Intensity of the abundance maps are normalized within each component. 200
5.29 A. Spectrum of the component I in Fig. 5.28 and its corresponding abundance maps for all tilt angles are shown in B. 201
5.30 A. Spectrum of the component II in Fig. 5.28 and its corresponding abundance maps for all tilt angles are shown in B. 202
5.31 A. Spectrum of the component III in Fig. 5.28 and its corresponding abundance maps for all tilt angles are shown in B. 202
5.32 A. Spectrum of the component IV in Fig. 5.28 and its corresponding abundance maps for all tilt angles are shown in B. 203
5.33 A. Spectrum of the component V in Fig. 5.28 and its corresponding abundance maps for all tilt angles are shown in B. 203
5.34 A. Spectrum of the component VI in Fig. 5.28 and its corresponding abundance maps for all tilt angles are shown in B. 204
5.35 HAADF STEM micrographs (left) of the +40^o, 0^o, -40^o tilts of a 63 nm Ag@Au core-shell nanocube and a 53 AuAg nanoframe standing with ∼ 14 nm separation. On the right, the background subtracted local EEL spectra of different locations shown by black, blue, dark green, green, turquoise, orange, violet, purple and red squares are shown. Note that the color of each spectra corresponds to the color of the location indicated in the HAADF STEM micrographs. 205
5.36 Series of HAADF STEM micrographs of the Ag@Au core-shell nanocube and AuAg nanoframe obtained simultaneously with the EELS SI at different tilt angles between +64^o and -52^o with different intervals. 207
5.37 Spectra of 7 different components of the Ag@Au core-shell nanocube and AuAg nanoframe, obtained by VCA and their corresponding abundance maps for different tilts. Intensity of the abundance maps are normalized within each component. 208
5.38 A. Spectrum of the component I in Fig. 5.37 and its corresponding abundance maps for all tilt angles are shown in B. 209
5.39 A. Spectrum of the component II in Fig. 5.37 and its corresponding abundance maps for all tilt angles are shown in B. 210
5.40 A. Spectrum of the component III in Fig. 5.37 and its corresponding abundance maps for all tilt angles are shown in B. 210
5.41 A. Spectrum of the component IV in Fig. 5.37 and its corresponding abundance maps for all tilt angles are shown in B. 211
5.42 A. Spectrum of the component V in Fig. 5.37 and its corresponding abundance maps for all tilt angles are shown in B. 211
5.43 A. Spectrum of the component VI in Fig. 5.37 and its corresponding abundance maps for all tilt angles are shown in B. 212
5.44 A. Spectrum of the component VII in Fig. 5.37 and its corresponding abundance maps for all tilt angles are shown in B. 212

List of Tables

1.1 Plasma resonance conditions and related resonance frequencies for different sample geometries in vacuum ($\epsilon_{med} = 1$). d is the thickness of the thin film and x is the direction parallel to the film. $\bar{L}_m$ denotes the depolarization factor (Table adapted from [27]). 17

3.1 Comparison of the plasmon components obtained by Gaussian fitting, BSS and VCA routines for the Ag nanocube. 85
3.2 Comparison of the plasmon components obtained by Gaussian fitting, BSS and VCA routines for the Ag@Au core-shell nanocube. 98
3.3 Comparison of the plasmon components obtained by Gaussian fitting, BSS and VCA routines for the pinholed AuAg nanobox. 106
3.4 Comparison of the plasmon components obtained by Gaussian fitting, BSS and VCA routines for the single-walled AuAg nanobox along with the BEM simulation results on the single-walled AuAg nanoboxes with sharp (BEM-1) and smooth (BEM-2) corners. 115
3.5 Comparison of the plasmon components obtained by Gaussian fitting, BSS and VCA routines for the AuAg nanoframe along with the BEM simulation results on the perfect nanoframe with sharp corners and edges (BEM-1) and on a more realistic nanoframe with smooth corners and partially filled faces (BEM-2). 123
3.6 Comparison of the plasmon components obtained by Gaussian fitting, BSS and VCA routines for the double-walled AuAg nanobox. 127

4.1 A list of resonance energies and resonance types for 12 different modes observed during the BEM simulations on the Ag nanowire. 145
4.2 A list of resonance energies and resonance types for 12 different modes observed during the BEM simulations on the Ag nanotube. 150
4.3 A list of resonance energies and resonance types for 12 different modes observed during the BEM simulations on the Ag nanotube standing on a 15 nm thick Si_3N_4 substrate. 154
4.4 Comparison of the plasmon components obtained experimentally by Gaussian fitting and VCA routines and obtained by BEM simulations for the completely hollow AuAg nanotube. 158
4.5 Comparison of the plasmon components obtained experimentally by Gaussian fitting and VCA routines for the hybrid AuAg nanotube. 167

Ekinsu'ya,
"Kalplerimizde yepyeni bir dünya taşıyoruz, şimdi, şu anda büyümekte"

Chapter 1

Introduction

1.1 Plasmonics: Theoretical background

Metallic nanoparticles have a crucial role for the emerging technologies in the area of optics since they can manipulate light far beyond the diffraction limit [1]. Interaction of electromagnetic radiation and conduction electrons of metals (at the interfaces or small nanostructures) leads to an enhanced optical near field of sub-wavelength dimensions, termed as plasmons [2]. Thanks to the recent developments and increasing interest, a branch of photonics, "plasmonics" has grown into an independent research field, which deals with the science and technology of generation, control and manipulation of the excitations resulted by the light-matter interactions [1–6].

We start with the theoretical basics leading to the plasmon resonances, thus, plasmonics phenomena. It should be noted here that fundamental equations shown in this section are mostly adapted from Stefan A. Maier's [2] and Charles Kittel's [7] indispensable books.

1.1.1 Light, an electromagnetic wave

1.1.1.1 Maxwell's equations

Electromagnetic fields and their interaction with metals (even at the nanometer scale, down to few nanometers) can be defined classically by Maxwell's equations [8]:

$$\nabla \cdot \mathbf{D} = \rho_{ext} \tag{1.1}$$

$$\nabla \cdot \mathbf{B} = 0 \tag{1.2}$$

$$\nabla x \mathbf{E} = -\frac{\partial \mathbf{B}}{\partial t} \tag{1.3}$$

$$\nabla x \mathbf{H} = \mathbf{J}_{ext} + \frac{\partial \mathbf{D}}{\partial t}. \tag{1.4}$$

Equations (1.1) - (1.4) are related to four macroscopic fields of **D** (the dielectric displacement, Coulombs per square Meter), **B** (the magnetic induction or magnetic flux density, Teslas), **E** (the electric field, Volts per Meter) and H (magnetic field, Amperes per Meter) with external charge (ρ_{ext}) and current ($\mathbf{J}_{ext}$) densities. Note that charge and current densities are presented as external instead of total of internal and external as the external set drives the system [2].

These four macroscopic fields are furhter associated with the polarization **P** and magnetization **M** by

$$\mathbf{D} = \epsilon_0 \mathbf{E} + \mathbf{P} \tag{1.5}$$

$$\mathbf{H} = \frac{1}{\mu_0}\mathbf{B} - \mathbf{M} \tag{1.6}$$

where ϵ_0 is the electric permitivity ($\epsilon_0 \approx 8.854$ x 10^{-12} Farads per Meter) and μ_0 is the magnetic permeability ($\mu_0 \approx 4\pi$ x 10^{-7} Henries per Meter) of free space, i.e. vacuum. Since we are interested in nonmagnetic media throughout this thesis manuscript, we will not consider a magnetic response represented by **M**, therefore, we only consider cases where $\mathbf{B} = \mu_0 \mu \mathbf{H}$ (as the relative magnetic permeability of the nonmagnetic medium μ = 1, it becomes $\mathbf{B} = \mu_0 \mathbf{H}$) [2]. **P** is the density of electric dipoles, which are caused by the alignment of the microscopic dipoles with the applied electric field, inside a material [7]. It is related to the internal charge density ($\nabla \cdot \mathbf{P}$ = -ρ) and the conversation of charges ($\nabla \cdot \mathbf{J}$ = - $\partial\rho/\partial$t) compels that the internal charge density and current density are linked by

$$\mathbf{J} = \frac{\partial \mathbf{P}}{\partial t}. \tag{1.7}$$

The electrons within a material will generate a **P** as a respond to an applied **E** (according to equation (1.5)) [9]. When we consider a linear, isotropic and nonmagnetic media, **D** can be expressed as

$$\mathbf{D} = \epsilon_0 \epsilon \mathbf{E} \tag{1.8}$$

where ϵ is the dielectric constant or relative permitivity of the nonmagnetic medium. This linear relationship between **D** and **E** can also be defined by using the dielectric susceptibility χ, which describes the linear relationship between **P** and **E**, giving

$$\mathbf{P} = \epsilon_0 \chi \mathbf{E}. \tag{1.9}$$

Inserting equations (1.5) and (1.9) into (1.8) yields $\epsilon = 1 + \chi$. The last important fundamental relationship need to be mentioned here is between the internal current density $\mathbf{J}$ and the electric field $\mathbf{E}$, which is defined via conductivity σ

$$\mathbf{J} = \sigma \mathbf{E}. \tag{1.10}$$

Electromagnetic phenomena with metals can be defined using both ϵ and σ. For instance, at low frequencies the conductivity, σ is the preferred quantity, whereas, the dielectric function is commonly used in optical frequencies [2]. As underlined before, above presented relations are only valid in linear media and they do not exhibit temporal and spatial dispersion. However, the optical response of metals are known to be dependent on frequency (ω) and wave vector (K). Therefore, we have to express these linear relationships by taking the non-locality in time and space into account. They can be simplified as the following in the Fourier domain [2]:

$$\mathbf{D}(\mathbf{K}, \omega) = \epsilon_0 \epsilon(\mathbf{K}, \omega) \mathbf{E}(\mathbf{K}, \omega) \tag{1.11}$$

$$\mathbf{J}(\mathbf{K}, \omega) = \sigma(\mathbf{K}, \omega) \mathbf{E}(\mathbf{K}, \omega). \tag{1.12}$$

Using equations (1.5), (1.7) and (1.11-1.12), we can derive the fundamental relationship between the relative permitivity (i.e. dielectric function) and the conductivity (in the Fourier domain ∂/∂t $\rightarrow$ -iω)

$$\epsilon(\mathbf{K}, \omega) = 1 + \frac{i\sigma(\mathbf{K}, \omega)}{\epsilon_0 \omega}. \tag{1.13}$$

The spatially local response of metals can be defined as the following for the optical properties:

$$\epsilon(\mathbf{K} = 0, \omega) = \epsilon(\omega). \tag{1.14}$$

This is only valid for the conditions where the wavelength λ is larger than the characteristic dimensions of the material (mean free path of the electrons inside the material can be considered as a characteristic dimension for the surfaces). As mentioned earlier, we are interested in the plasmonic properties of hollow metal nanostructures throughtout this thesis manuscript. This allows us, since the wavelength of the light is larger than the nanoparticle dimensions, to neglect the dependence on momentum and to use this quasistatic approximation [2].

In general, as linked to equation (1.13), $\epsilon(\omega) = \epsilon_1 + \mathrm{i}\epsilon_2$ and $\sigma(\omega) = \sigma_1 + \mathrm{i}\sigma_2$ are complex valued functions of the frequency ω. ϵ can be defined experimentally at optical frequencies by reflectivity studies and the assessment of the complex refractive index $n\ (\omega) = n\,(\omega) + i\kappa\,(\omega)$ of the medium, defined as $n = \sqrt{\epsilon}$. κ is called the extinction coefficient which determines the optical absorption of electromagnetic waves propagating through the medium. κ is associated with the absorption coefficient α by the relation

$$\alpha(\omega) = \frac{2\kappa(\omega)\omega}{c}. \tag{1.15}$$

This indicates that the imaginary part ϵ_2 of the dielectric function dictates the amount of absorption inside the medium. For the cases where $|\epsilon_1| \gg |\epsilon_2|$, real part of the refractive index n is mainly determined by ϵ_1. Examination of equation (1.13) thereby reveals that the real part of σ regulates the amount of absorption and the amount of polarization is governed by the imaginary part which contributes to ϵ_1 [2].

When examining the traveling-wave solutions of Maxwell's equations (1.3 and 1.4) in the absence of an external stimuli and in the time and Fourier domains, one can come up with two distinguishable cases depending on the polarization direction of the **E**: For transverse waves, $\mathbf{K}\cdot\mathbf{E} = 0$, yielding a dispersion relation of

$$K^2 = \epsilon(\mathbf{K}, \omega)\frac{\omega^2}{c^2} \tag{1.16}$$

and for long longitudinal waves $\epsilon(\mathbf{K}, \omega) = 0$. The latter signifies that the longitudinal collective oscillations can only take place for frequencies that correspond to zeros of $\epsilon(\omega)$, which will be revisited in the following while mentioning about bulk plasmons.

1.1.1.2 The dielectric function of the free electron gas

We continue by introducing the dielectric function of the free electron gases of metals [7]. The optical properties of metals can be described by a *plasma model*, where a gas of free electrons with an electron concentration of n moves against a stable background of positive ion cores [2, 7]. We should point out here that plasma is a medium with equal concentration of positive and negative charges where, at least, one charge type is mobile [7].

The dielectric response $\epsilon(\omega, 0)$ or $\epsilon(\omega)$ of an electron gas can be obtained from the equation of motion, where we apply Newton's law to a single free electron, where the electrons oscillate in an applied field $\mathbf{E}$ and their motion is damped via collisions with a collision frequency of $\gamma = 1/\tau$ (τ being the relaxation time of the free electron gas):

$$m\frac{d^2x}{dt^2} + m\gamma\frac{dx}{dt} = -e\mathbf{E}. \tag{1.17}$$

If $\mathbf{x}$ and $\mathbf{E}$ have the harmonic time dependence ($\mathbf{E}_{(t)} = \mathbf{E}_{(0)}e^{-i\omega t}$ and $\mathbf{x}_{(t)} = \mathbf{x}_{(0)}e^{-i\omega t}$), then

$$\mathbf{x}(t) = \frac{e}{m(\omega^2 + i\gamma\omega)}\mathbf{E}(t). \tag{1.18}$$

The $\mathbf{P}$ can be given by

$$\mathbf{P} = -ne\mathbf{x} = -\frac{ne^2}{m\omega^2 + i\gamma\omega}\mathbf{E}. \tag{1.19}$$

As given in equation (1.13), the dielectric function at a frequency ω can be expressed as [7]

$$\epsilon(\omega) = 1 + \frac{\mathbf{P}(\omega)}{\epsilon_0\mathbf{E}(\omega)}. \tag{1.20}$$

We reach to the dielectric function of the free electron gas by combining (1.19) and (1.20):

$$\epsilon(\omega) = 1 - \frac{ne^2}{\epsilon_0 m\omega^2 + i\gamma\omega}. \tag{1.21}$$

The plasma frequency ω_p is defined by

$$\omega_p^2 = \frac{ne^2}{\epsilon_0 m}, \tag{1.22}$$

which emerges as the frequency of the collective oscillation of the free electrons in the metal, i.e. the oscillation is originated by an electric field due to all the electrons, hence it is called a collective oscillation [10]. The definition of a plasmon relies in this argument: A plasmon is a quantum of a plasma oscillation (the collective oscillations of the free electrons defined by the plasma frequency) [7, 10]. We, therefore, write the dielectric function as

$$\epsilon(\omega) = 1 - \frac{\omega_p^2}{\omega^2 + i\gamma\omega}. \tag{1.23}$$

This equation is known as the "Drude" model [11, 12]. Fig. 1.1 shows the variation of the dielectric function of a free electron gas versus ω/ω_p [7]. As can be seen in this figure, electromagnetic waves propagate without damping only for the conditions where ϵ is positive and real. For negative ϵ, electromagnetic waves are totally reflected. This behavior can be understood by considering the dispersion relation presented in equation (1.16), which tells us a lot about the dielectric function and frequency relationship. For instance, if we consider a real and positive ϵ, K is real for real ω and a transverse electromagnetic wave propagates with a phase velocity of c/$\epsilon^{1/2}$. For a real but negative ϵ, K is imaginary for real ϵ, where the wave is damped with a characteristic length of 1/|K|. When ϵ is imaginary, $\mathbf{K}$ is imaginary for real ω and waves are damped in space. Two other cases can be defined considering $\epsilon = \infty$ and $\epsilon = 0$. When $\epsilon = \infty$, the sysyem has a finite in the absence of an $\mathbf{E}$ where the $\epsilon(\omega, \mathbf{K})$ determines the frequencies of the oscillations. As mentioned before, when $\epsilon = 0$, longitudinally polarized waves are possible only at the zeros of ϵ [7].

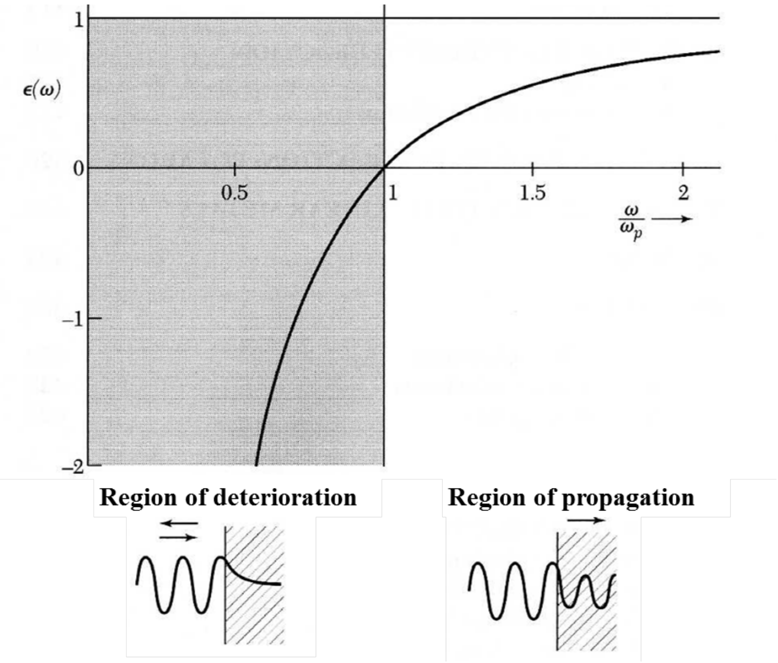

FIGURE 1.1: Dielectric function $\epsilon(\omega)$ of a free electron gas versus frequency (in plasma frequency ω_p units). Electromagnetic waves propagate without damping (lossless) only for the cases where ϵ is positive and real, whereas they are totally reflected when ϵ is negative (figure adapted from [7])

.

Here, we are interested on the frequencies $\omega < \omega_p$, where metals retain their metallic character [2]. For large frequencies, where ω is close to ω_p, the dispersion relation leads to a negligible damping where $\epsilon(\omega)$ is predominantly real and can be expressed as

$$\epsilon(\omega) = 1 - \frac{\omega_p^2}{\omega^2}. \tag{1.24}$$

However, it should be noted that the behavior of noble metals, such as Au, Ag and Cu, in this frequency region is completely regulated by the interband transitions, leading to an increase in the imaginary part of the ϵ. As suggested by the name, this model assumes an ideal free-electron metal, which is not completely valid for the real metals [7]. One needs to modify the so-called Drude model for the noble metals used in plasmonics. Free-electron model dictates that $\epsilon \rightarrow 1$ at $\omega \gg \omega_p$. An extension to this is needed in the region $\omega > \omega_p$, where the response is dominated by free s electrons for the noble metals such as Au, Ag and Cu. This is due to the fact that the d-band is close to the Fermi surface, which generates a highly polarized environment due to the positive backgound of the ion cores [2]. We describe the $\mathbf{P}_\infty = \epsilon_0(\epsilon_\infty$ - $1)\mathbf{E}$, after adding this to the equation (1.5) $\mathbf{P}$ represents only the polarization caused by the free electrons. ϵ_∞ lies in the range of $1 \leq \epsilon_\infty \leq 10$, thus, we can write the dielectric function as:

$$\epsilon_{(\omega)} = \epsilon_\infty - \frac{\omega_P^2}{\omega^2 + i\gamma\omega}. \tag{1.25}$$

Application of this description to Au and Ag is shown in Fig. 1.2 illustrating its validity limits. This figure shows the real (on the left) and imaginary (on the right) parts of the dielectric functions of Au (A) and Ag (B) for the free-electron model (black solid lines) and experimental dielectric data (red dotted lines). Experimental dielectric data used in this figure is obtained from Johnson and Christy [13]. As seen in these figure, the Drude model is not acceptable for describing either real or imaginary parts of Au and Ag due to interband transitions not being taken into account [2]. Especially for the case of Au, its validity breaks down in the visible range (even starting from the near-infrared region).

It is clear that the Drude model fails in describing the optical properties of Au and Ag at the visible frequencies. One can overcome this by taking the effects of interband transitions into account by replacing equation (1.17) by

$$m\frac{d^2x}{dt^2} + m\gamma\frac{dx}{dt} + m\omega_0^2 x = -e\mathbf{E}, \tag{1.26}$$

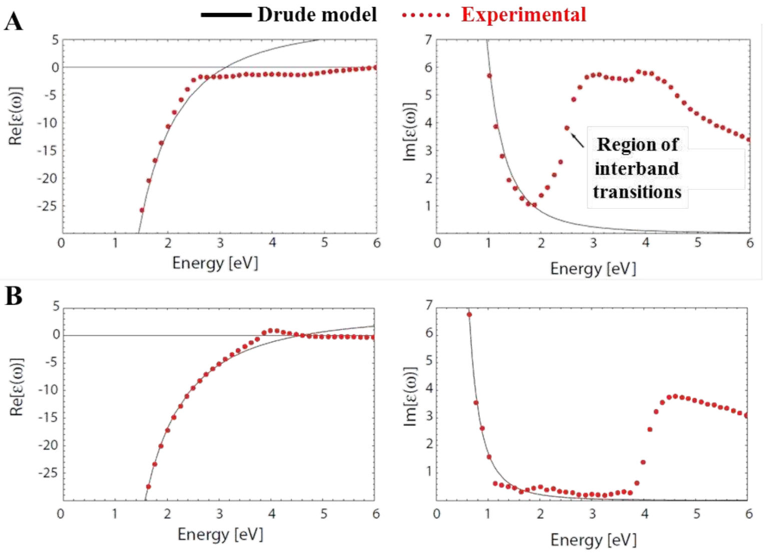

FIGURE 1.2: Real and imaginary parts of the dielectric functions of Au (A) and Ag (B) for the free-electron model (black solid lines) and experimental dielectric data (red dotted lines). As seen in these graphs, the interband transitions limit the validity of the model (figure adapted from [2]).

which relates the interband transitions to the classical picture of a bound electron with resonance frequency ω_0. We therefore obtain so-called "Lorentz" model, which is derived as [2]:

$$\epsilon_{(\omega)} = \epsilon_\infty - \frac{\omega_P^2}{\omega^2 - \omega_0^2 + i\gamma\omega}. \tag{1.27}$$

It should be pointed out that both the Drude and Lorentz models are useful and describe the optical properties of many materials quite accurately.

Volume plasmons

We have already introduced the term plasmon as collective oscillation of the conduction electrons in a material. We have also introduced the conditions for plasmon excitations. Here, we like to shortly mention about the volume plasmons, also known as bulk plasmons, as the next section will be focused on the surface plasmon resonances. Volume or bulk plasmons are the plasmons inside the "bulk" of the materials. As mentioned above, when $\omega = \omega_p$, $\epsilon = 0$ and K = 0, the oscillation of the conduction electrons has a constant phase throughout the metal, where all the free electrons are oscillating in phase at the plasma frequency [7].

Fig. 1.3 schematically shows this mechanism. Let us assume that we have a metal film as shown in Fig. 1.3A. We locate the charges as "+" signs representing the fixed positive background of the ions and the free electron gas as dark gray background (as shown in

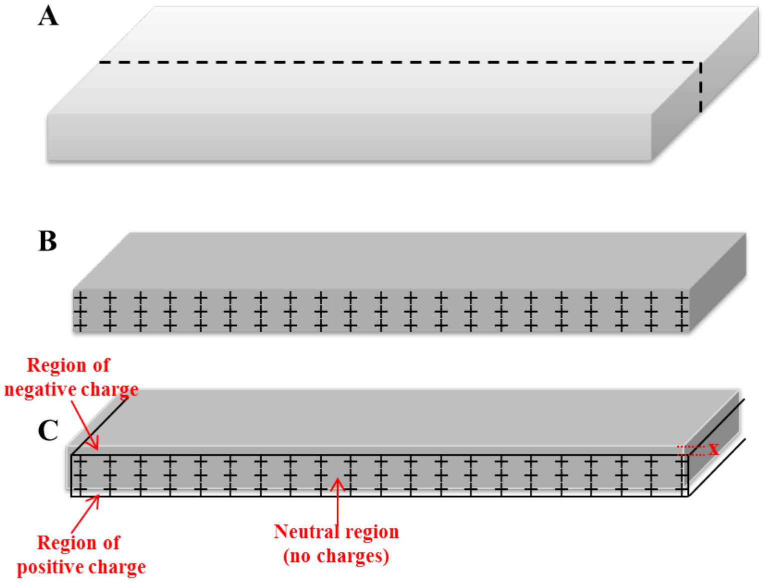

FIGURE 1.3: A. Schematic of a metal film. B. Cross section along the dotted lines in A, where the positive ion cores are presented by + and the free electron gas is presented by gray background. C. shows the distribution of charges after a motion of the free electron gas, where the negative charges are uniformly displaced upward by a distance of ”x”. As a result of this motion, upper part of the metal film has a region of negative charges (with a surface charge density of -nex, ne being electron concentration) and the lower part of the film has a region of positive charges (with a surface charge density of +nex). An electric field **E** = 4πex is created inside the metal film.

Fig. 1.3B). Let us now suppose that the electrons are displaced by distance of ”x”, creating the positively and negatively charged regions (as illustrated in Fig. 1.3C). This displacement of charges generates a charge density ρ:

$$\rho = 4\pi nex. \tag{1.28}$$

An electric field **E** is generated by this charge density:

$$\mathbf{E} = 4\pi nex. \tag{1.29}$$

The oscillating electrons are faced to a force by this generated electric field, therefore, the oscillation can be explained by the above presented (equation (1.17)) motion. The plasma frequency was defined in equation (1.22). With this, we can express the equation of motion as the following:

$$\frac{d^2x}{dt^2} + \omega_p^2 x = 0. \tag{1.30}$$

This relation clearly shows that ω_p is the frequency of the oscillation of the conduction electrons, hence, the plasmons being the quanta of these plasma oscillations. It was Pines and Bohm who first discussed a quantized bulk plasma oscillation of electrons in a metallic solid in order to explain the energy losses of fast electrons passing through metallic foils [14]. They called this excitation a "plasmon" in 1952, nowadays, we have slightly modified this definition by naming it as volume or bulk plasmon in order to distinguish between the surface plasmons, which will be introduced in the following.

1.1.2 Surface plasmon resonances

So far, we have introduced a background leading to the plasmons from a solid state point of view and the concept of volume plasmons. In this section, we will present the surface plasmons. In general, the surface plasmon term is used to describe both polarization oscillations of metallic nanoparticles (known as localized surface plasmon resonances) and waves propagating along a plane interface between metal and a dielectric (known as propagating surface plasmons or surface plasmon polaritons(SPPs)) [10]. The surface electromagnetic waves were first discussed by Zenneck [15] and Sommerfeld [16]. Rithie expanded the work of Pines and Bohm and investigated the metal film surfaces where he found the presence of a new lowered loss at the interface due to the excitation of surface collective oscillations [17]. In 1959, Powell and Swan manifested the existence of these oscillations by a series of electron energy-loss spectroscopy studies in aluminum [18] and magnesium [19] foils. One year later, Stern and Ferrel named these oscillations as surface plasmons [20].

As we will be showing results about plasmonic properties of metal nanostructures along this thesis manuscript, we will give an emphasis to the former case, i.e. localized surface plasmon resonances (LSPR). Yet, it is important to mention about the surface plasmon polaritons as they have been used in many different applications [21].

1.1.2.1 Surface plasmon polaritons

As mentioned above, surface plasmon polaritons are surface electromagnetic waves that propagate along the metal/dielectric(or vacuum) interface. Fig. 1.4A shows the dispersion curves of bulk plasmon (green-dashed line) and surface plasmon polariton (blue-dashed line) [22], whose behavior will be discussed in detail in the following. Fig. 1.4B shows the schematic of the SPP propagation and surface charge density between two semi infinite nonmagnetic media. Medium I is a material (or environment) with a positive dielectric constant and medium II is a material (metal) with a negative dielectric constant.

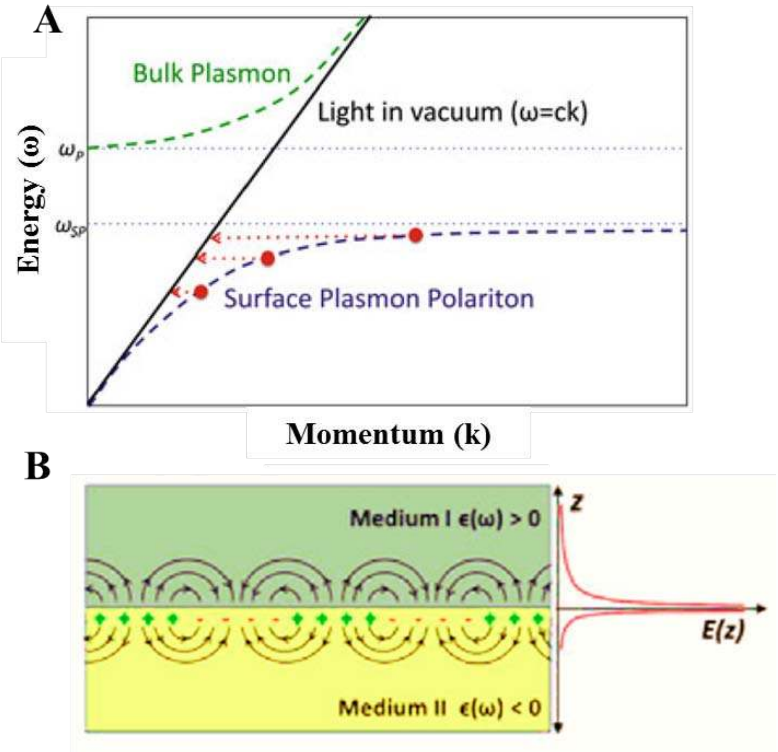

FIGURE 1.4: A. Dispersion curves of the bulk plasmon (green-dashed line) and surface plasmon polariton(blue-dashed line), where the curve of light in vacuum is shown as a solid black line. Certain momentum provisions that allows coupling to light are shown by red dots and red-dashed lines. B shows the representative sketch of a mechanism of propagating surface plasmon polariton (figure adapted from [22])

The electric field **E** related with the surface plasmon, known as the evanescent field, drops off exponentially in the metal and in the dielectric [2]. The **E** complies the Helmholtz equation in both media [10]:

$$\nabla^2 E_i + \mu_i \epsilon_i \frac{\omega^2}{c^2} E_i = 0, \tag{1.31}$$

with i = 1, 2. Solutions to the Maxwell's equations are generally classified as s-polarized and p-polarized electromagnetic modes [23]). For an ideal surface that can generate propagating waves along the interface, component of the electric field must be normal to the surface. Therefore, s-polarized mode, with its **E** being parallel to the interface do not exist [23]. We seek a solution for the p-polarized mode, which is also called transverse magnetic (TM) mode as it is **H** is parallel to the interface. x-axis being the propagation direction, we can write,

$$z > 0 \qquad E_{x1} = E_0 \exp[i\alpha x + i\gamma_1 z], \tag{1.32}$$

$$z < 0 \qquad E_{x2} = E_0 \exp[i\alpha x - i\gamma_2 z], \tag{1.33}$$

which satisfies the continuity condition along the interface [10]. In these conditions,

$$\gamma_1 = [\mu_1 \epsilon_1 \frac{w^2}{c^2} - \alpha^2]^{1/2} \tag{1.34}$$

with $\mathrm{Im}(\gamma_1) > 0$ and

$$\gamma_2 = [\mu_2 \epsilon_2 \frac{w^2}{c^2} - \alpha^2]^{1/2} \tag{1.35}$$

with $\mathrm{Im}(\gamma_2) > 0$, defining the evanescent decay length of the fields perpendicular to the interface [2, 10]. As stated, we only look for transverse waves, thus, $\nabla \cdot \mathbf{E} = 0$. In Fourier domain, this relation becomes $\mathbf{k} \cdot \mathbf{E} = 0$ where $\mathbf{k} = (\alpha, 0, \gamma)$, following:

$$z > 0 \qquad E_{z1} = -\frac{kE_o}{\gamma_1} \exp[i\alpha x + i\gamma_1 z], \tag{1.36}$$

$$z < 0 \qquad E_{z2} = \frac{kE_o}{\gamma_2} \exp[i\alpha x - i\gamma_2 z]. \tag{1.37}$$

When we implement the continuity condition of the z-component of $\epsilon \mathbf{E}$ at the interface, we get

$$\frac{\gamma_2}{\gamma_1} = -\frac{\epsilon_2}{\epsilon_1}. \tag{1.38}$$

Equation (1.38) is the surface-plasmon condition [23]. This equations shows the dispersion relations of the surface wave, where the confinement to the surface demands $\mathrm{Re}[\epsilon_1] < 0$ if $\epsilon_2 > 0$. Thus, the surface waves exist only at interfaces between a conductor and an insulator. For TM polarization, the surface-plasmon condition can be expressed as (where α is shown as $\mathrm{K}_{SP}(\omega)$) [10]:

$$K^2_{SP}(\omega) = \frac{\omega^2}{c^2} \frac{\epsilon_1 \epsilon_2}{\epsilon_1 + \epsilon_2}. \tag{1.39}$$

With this information, we can revisit the dispersion relation presented in Fig. 1.4A. For small momentums corresponding to low frequencies, the SPP propagation constant is close to k_0 at light line. In this regime, the waves extend into dielectric space over many wavelengths and SPPs have hte nature of a grazing-incidence light field, also known as Sommerfeld-Zenneck waves [2]. In the regime of large momentums, the frequency of the SPPs reaches to the surface plasmon frequency

$$\omega_{sp} = \frac{\omega_p}{\sqrt{1+\epsilon_2}}. \tag{1.40}$$

In the limit of negligible damping, where $\mathrm{Im}[\epsilon_1(\omega)] = 0$, the wave vector (momentum) goes to infinity as the frequency approaches to ω_{sp}. Thereby, the mode acquires electrostatic character and it is known as the surface plasmon [2].

1.1.2.2 Localized surface plasmon resonances

Localized surface plasmon resonances (LSPRs) are non-propagating excitations of the conduction electrons of metallic nanoparticles under an applied electromagnetic field. Within this definition, we already mentioned about the terms "localized" and "non-propagating", which differentiates these oscillations of surface charge densities of metallic nanoparticles than the above presented surface plasmon polariton. In this case, the oscillations are under the constraints of the physical boundaries of the nanoparticle geometry [2, 22]. Another difference between the SPPs and LSPRs is that the LSPRs occur naturally due to the scattering of small (sub-wavelength where the particles size, $d \ll \lambda$) metal nanoparticles even by direct light illumination, where the phase-matching techniques has to be employed for the SPPs [2]. In 1908, Mie solved the Maxwells equations developing an electromagnetic theory of scattering and absorption of light by spherical particles [24]. This so-called Mie theory is still valid for spherical nanoparticles and can be used for non-spherical nanoparticles after modifications. In Mie theory, the scattering and absorption by a nanoparticle can be given by scattering and absorption cross-sections which relate the energy that is scattered (sent back) to the far field and absorbed (depleted) within the nanoparticle [22]. Scattered cross-section C_{scat} can be related to the scattered power I_{scat} and incident power I_{inc} by $C_{scat} = I_{scat}/I_{inc}$, where absorbed cross-section $C_{abs} = I_{abs}/I_{inc}$. For a spherical nanoparticle with a radius a, we can find

$$C_{scat} = \frac{8\pi}{3}k^4a^6\left|\frac{\epsilon_{sph}-\epsilon_{med}}{\epsilon_{sph}+2\epsilon_{med}}\right| = \frac{k^4}{6\pi}|\alpha_{sph}|^2 \Rightarrow C_{scat} \propto \frac{a^6}{\lambda^4} \tag{1.41}$$

$$C_{abs} = 4\pi ka^3\mathrm{Im}\left\{\frac{\epsilon_{sph}-\epsilon_{med}}{\epsilon_{sph}+2\epsilon_{med}}\right\} = k\mathrm{Im}\alpha_{sph} \Rightarrow C_{abs} \propto \frac{a^3}{\lambda}, \tag{1.42}$$

where α_{sph} is the dipolar polarizability of the spherical particle, defined by $\mathbf{p} = \epsilon_0\epsilon_m\alpha\mathrm{E}_0$, in the quasistatic approach:

$$\alpha_{sph} = 4\pi\epsilon_0 a^3\frac{\epsilon_{sph}-\epsilon_{med}}{\epsilon_{sph}+2\epsilon_{med}}, \tag{1.43}$$

where ϵ_{sph} being the dielectric function of the spherical particle and ϵ_{med} being the dielectric function of the surrounding medium [22]. If the ϵ_{sph} is constant and its imaginary part is negligible, the scattering cross-section reveals a a flat spectral response and almost zero absorption. A resonant enhancement can be obtained when the $\mid \epsilon_{sph} + 2\epsilon_{med} \mid$ is a minimum, which simplifies to

$$R_e\left[\epsilon\left(\omega\right)\right] = -2\epsilon_{med}, \tag{1.44}$$

for the case of small or slowly-varying Im[ϵ] [2]. This relationship gives the dipole localized surface plasmon mode of the metal nanoparticle and it is called the Fröhlih condition [2, 22, 25, 26]. For a metallic nanoparticle in vacuum ($\epsilon_{med} = 1$) with a dielectric function given as the Drude model (equation (1.23)), the Fröhlih condition is met at a resonance frequency $\omega_{res} = \frac{\omega_p}{\sqrt{3}}$. At the Fröhlih frequency, along with a generation of a very large $\mathbf{P}$, the amplitude of the $\mathbf{E}$ outside the particle becomes very large (especially near the particle surface) [26]. The resonance, which generates the dipole surface plasmon modes, shifts to lower energies (red-shifts) as the dielectric constant of the medium increases [2]. The schematics of dipole localized surface plasmon mode excitations from a spherical and elongated particle are shown in Fig. 1.5.

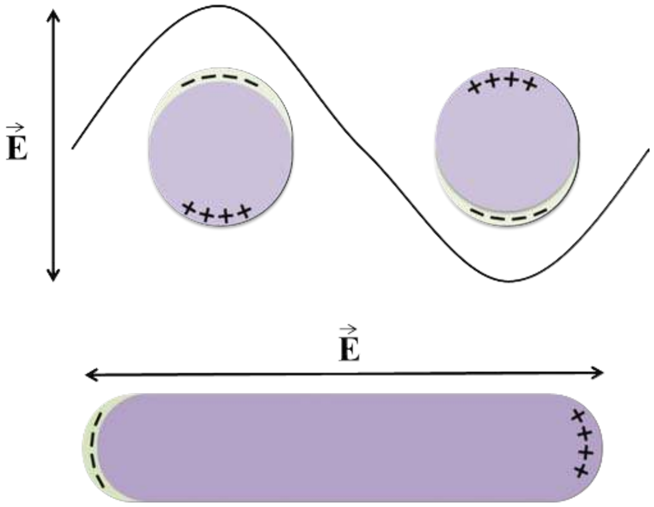

FIGURE 1.5: The schematic representations of the oscillations of surface charge densities, creating dipole localized surface plasmon modes, in spherical (upper) and elongated (lower) nanoparticles under applied **E**.

The equation (1.44), which leads to the generation of the dipole localized surface plasmon modes, is simply the same equation as:

$$\epsilon(\omega) = -\frac{l+1}{l}\epsilon_{med}, \qquad l = 1, 2, ... \tag{1.45}$$

with l = 1 [26]. It is, thus, clear that generation of high order localized surface plasmon modes complies the same relation. Fig. 1.6 shows the schematic representation of higher l-order LSPRs generated in a metallic nanorod [22]. These higher order modes are time-oscillating, stationary surface charge densities.

As a conclusion to this section, we can summarize the above mentioned resonance conditions and frequencies for different type of sample geometries, hence, different type of plasmon resonances. Table 1.1 shows the resonance conditions and related resonance frequencies for the plasmon excitations for a bulk metal, planar surface, thin film, spherical and ellipsoid nanoparticles (only dipole modes), which is adapted from [27].

In this section, we have presented the theoretical basics behind the excitation of different kinds of plasmon resonances such as volume plasmons, surface plasmon polaritons and localized surface plasmon resonances. As mentioned, we are mostly interested in the LSPRs, which is the type that is generated by the investigated nanostructures in this thesis manuscript. After giving a short theoretical background about the LSPRs in this section, the following section is devoted to the characteristics of LSPRs such as shape and composition dependency, substrate effects and so on from a practical point of view.

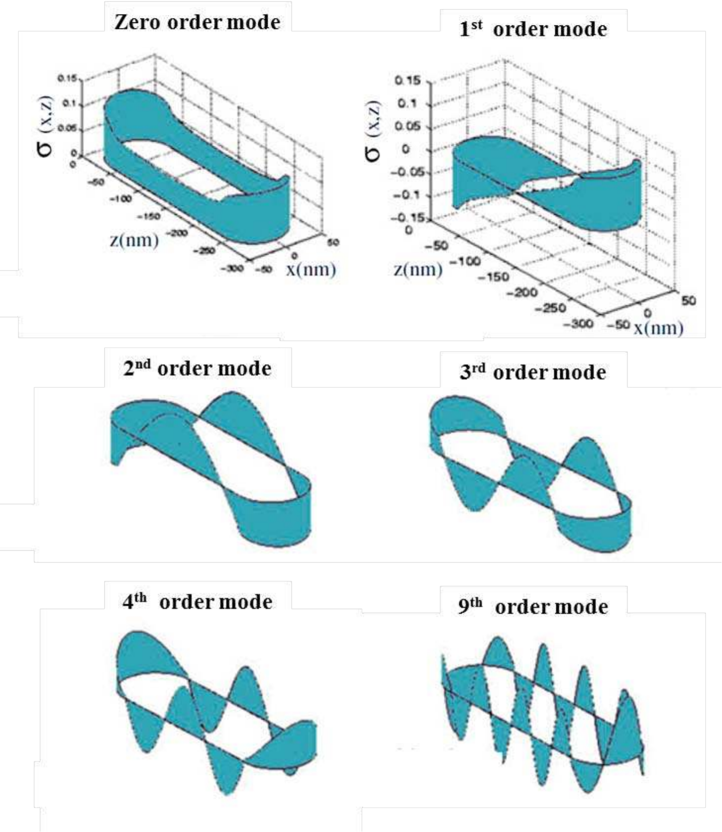

Figure 1.6: Schematic representation of higher l-order modes for an elongated nanorod, showing the distribution of zero order, first order, second order, third order, fourth order and ninth order LSPR modes (figure adapted from [22]).

Table 1.1: Plasma resonance conditions and related resonance frequencies for different sample geometries in vacuum ($\epsilon_{med} = 1$). d is the thickness of the thin film and x is the direction parallel to the film. $\bar{L}_m$ denotes the depolarization factor (Table adapted from [27]).

Sample geometry	**Resonance condition**	**Resonance frequency**
Bulk metal	$\epsilon_1(\omega) = 0$	$\omega_1 = \omega_p$
Planar surface	$\epsilon_1(\omega) =$ -1	$\omega_1 = \frac{\omega_p}{\sqrt{2}}$
Thin film	$\frac{\epsilon(\omega)+1}{\epsilon(\omega)-1} = \exp\left(-(k)_x d\right)$	$w_1 = \frac{wp}{\sqrt{2}}\sqrt{1\exp\left(-(k)_x d\right)}$
Spherical nanoparticle	$\epsilon_1(\omega) =$ -2	$\omega_1 = \frac{\omega_p}{\sqrt{3}}$
Ellipsoid nanoparticle	$\epsilon_1\left(\omega\right) = -\frac{1-\bar{L}_m}{\bar{L}_m}$	$\omega_1 = \omega_p \bar{L}_m$

1.2 Effects of intrinsic and extrinsic parameters on the LSPRs

This section is about the effects of intrinsic and/or extrinsic parameters such as size, shape, composition, environment (surrounding medium, substrate) or coupling on the final properties of LSPRs. As mentioned above, we will present these effects from a practical point of view, i.e. by not going deep into the theory and physics behind them. For further information, these effects are widely described in literature [2, 6, 21]. It is well-known that the LSPR properties of the metallic nanostructures are affected by their size, shape, composition and environment [28, 29] and, many different nanostructures have been investigated so far [30]. In the following, we will present an overview about the effects of these parameters on the LSPRs of different metal nanostructures.

1.2.1 Size effects

Instric size effects of the plasmonic nanoparticles can be understand by taking size dependent damping into account [2, 22, 31], as standard Mie theory and scattering-based methods only allow the study extrinsic size effects [32, 33]. There are numerous studies investigating the size effects of various metal nanostructures on their plasmonic properties [28, 29, 31–44]. In the following, we will give examples from several studies pointing out the typical size effects for different kinds of metal nanostructures.

Berciaud et al. [33] investigated the intrinsic size effects of the individual Au nanoparticles, with diameters between 5 and 33 nm, on their optical properties. They reported that the energy of the plasmon peak shifts to higher energies as the particle sizes get smaller (Fig. 1.7A). Another effect of the decreasing nanoparticle size is on the full-width-at-half-maximum (FWHM), which gets broader as the size gets smaller and it is almost impossible to define the FWHM for the 5 nm Au nanoparticles from the given absorption spectra (Fig. 1.7C). Therefore, they have introduced another parameter of red half-width at half-maximum $\Gamma_{1/2}$ = E$_R$ - E1/2 where E1/2 is the resonant energy at half of the absorption intensity [33]. It shifts to higher energy widths as the particle diameter gets smaller. Link and El-Sayed [43] studied the optical properties of spherical Au nanoparticles with sizes between 9 nm and 99 nm, and reported a similar behavior as [33], where the plasmon energy shifted to higher energies as the nanoparticle size was getting smaller (Fig. 1.7B). They also showed that the plasmonic properties of nanoparticles smaller than ∼12 nm are controlled by the intrinsic size effects, whereas when their sizes get bigger, then the plasmonic properties are determined by the extrinsic size effects (Fig. 1.7D.)

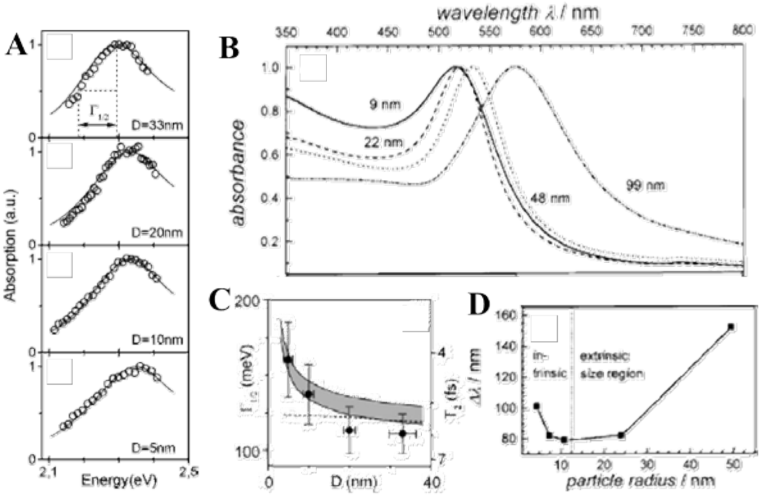

FIGURE 1.7: A. and B. Absorption spectra of the Au nanoparticles with various sizes, where the experimental values (open circles) are compared with the Mie theory simulations (solid lines) in A. C. The shift of the $\Gamma_{1/2}$ (indicated in A) versus the nanoparticle diameter. D. Change in the wavelength versus nanoparticle sizes defining the intrinsic and extrinsic regions (figure adapted from [33] and [43].

Another example about size effects of nanostructures on their plasmonic properties is shown in Fig. 1.8. Sanchez-Iglesias et al. [34] investigated the synthesis of Au nanodecahedra with fine size tuning and they reported that plasmon resonances shift to lower energies (higher wavelengths) as the size of the nanodecahedra get larger (Fig. 1.8C). Photographs of the solutions taken from the different stages of the typical nanodecahedra synthesis (Fig. 1.8A) and a TEM micrograph (Fig. 1.8B) showing the synthesized Au nanodecahedra are also presented in this figure. As seen in the photographs of the solution, a fine control over the optical properties can be obtained simply by controlling the sizes of the nanostructures.

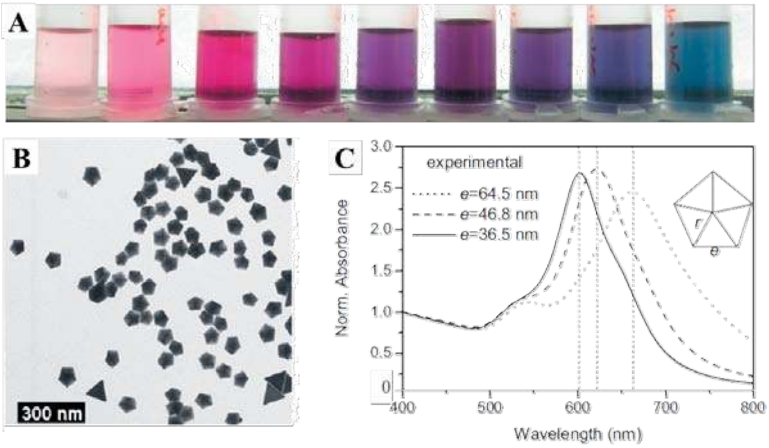

FIGURE 1.8: A. Photographs of solutions at various times during a typical synthesis of Au nanodecahedra with size control. B. UV-Vis spectra showing the absorption changing by size. C. TEM micrographs of Au nanodecahedra (figure adapted from [34]).

Spectral tunability of Au nanorods in terms of control over nanorod size and aspect ratio is well documented in the literature [29, 39, 43, 45]. Fig. 1.9 shows the change of optical properties of Au nanorods by the changes in their aspect ratio. As seen in Fig. 1.9A, the plasmon resonances shifts to higher wavelengths (lower energies) by increasing aspect ratios [29]. Fig. 1.9B, Fig. 1.9C and Fig. 1.9D are TEM micrographs of different Au nanorods with aspect ratios of ∼2.4, ∼2.6 and ∼3.8, respectively [39]. Insets in the TEM micrographs are the photographs of the solutions revealing the change in optical properties by controlling the aspect ratio of the nanorods.

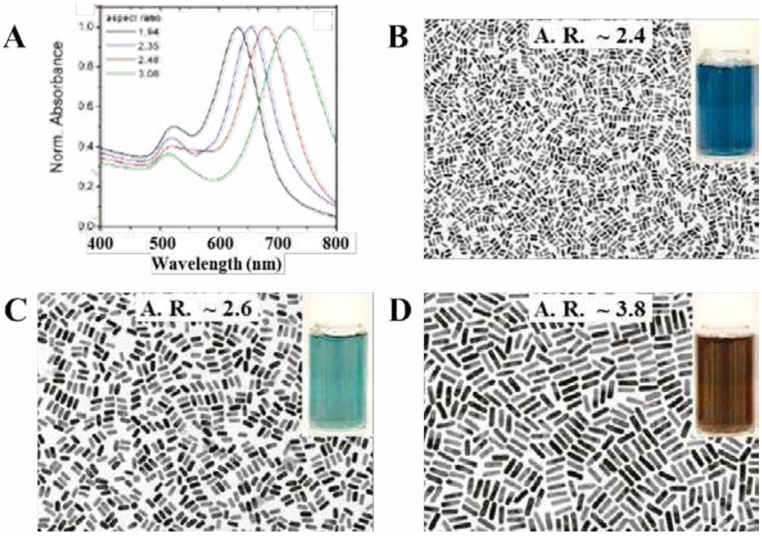

FIGURE 1.9: A. Absorption spectra of different Au nanorods with aspect ratios between 1.94 and 3.08, where the shift to higher wavelengths with the increasing aspect ratio is clearly revealed. B, C and D are TEM micrographs of different Au nanorods with aspect ratios of ∼2.4, ∼2.6 and ∼3.8, respectively. Insets in the TEM micrographs are the photographs of the solutions revealing the change in color by aspect ratio of the nanorods (figure adapted from [29] and [39]).

1.2.2 Shape effects

After presenting the size effects on the plasmonic properties of some commonly used nanostructures like spherical nanoparticles and nanorods, and some highly faceted nanostructures like nanodecahedra, we continue with the shape effects on the plasmonic properties of different metal nanostructures. As mentioned in the previous section, LSPR resonances are under the constraints of the physical boundaries of the nanoparticle geometry [2, 22]. Therefore, the shape of the nanoparticles define their LSPR properties. Similar to the size effects, there are many studies, both theoretical and experimental, about the effects of nanostructures' shape on their plasmonic properties [30, 46–59].

Fig. 1.10A shows the resonance range of different Au and Ag nanostructures from UV to mid infrared region [60]. As it can be seen here, modifying the shape, and/or size, of the nanostructures allows one to tune the plasmonic properties within the visible range and beyond. Fig. 1.10B shows the extinction spectra of different polyhedral Au nanostructures such as octahedron (in red), truncated octahedron (in yellow), cuboctahedron (in green), truncated cube (in blue), cube (in purple) and trisoctahedron (in black) [57]. Even though they have similar sizes (the length scale shown along the sketches are the same for all nanostructures), the possibility of fine tuning the plasmonic properties is obvious. Fig. 1.10C shows the plasmon resonance wavelength for spherical, pentagonal and triangular Ag nanostructures with different sizes [53]. The reason for the scattering of the plasmon resonance wavelengths for the case of Ag triangles was revealed to be due to the three-dimensional shape anomalies in triangular structure, suggesting the importance of the shape effects on the plasmonic properties of the nanostructures [53]. By looking at Fig. 1.10B and Fig. 1.10C, one can see that the shape of the nanostructure has more prevailing impact on the plasmonic properties than the size.

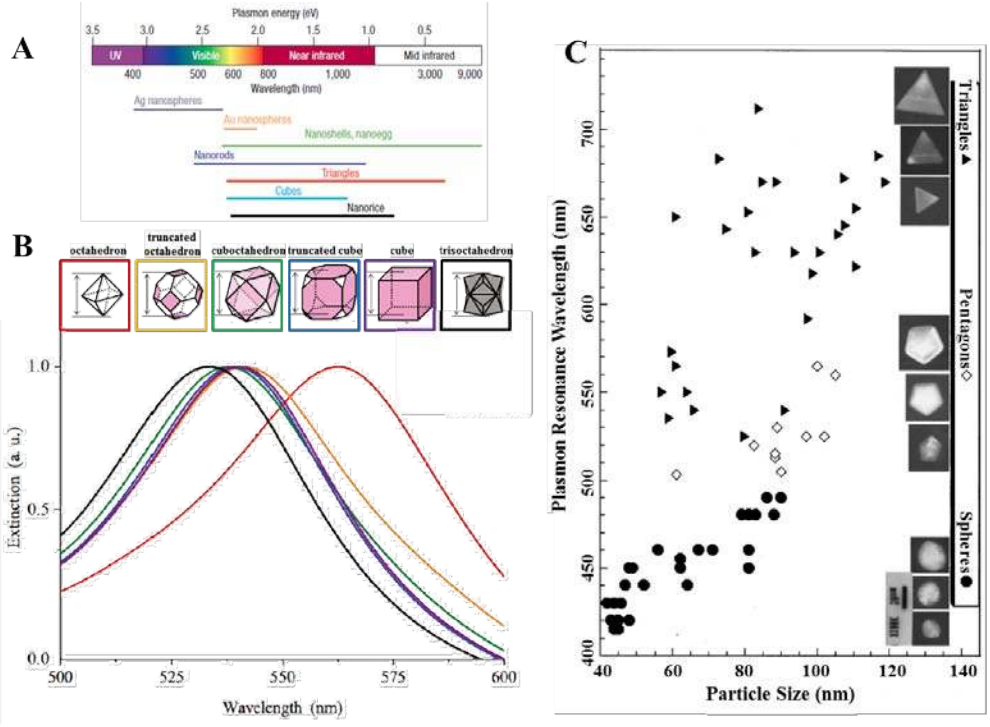

FIGURE 1.10: A. Different silver and gold nanostructures presenting their plasmon resonances in a wide range of spectrum from UV to mid infrared (figure reproduced from [60]). B. Extinction spectra of various polyhedral Au nanostructures (figure adapted from [57]). Note that the colors in the extinction spectra are the same as the colored squared around the structures, i.e. spectrum corresponding to the cuboctahedron is green. C. Plasmon resonance wavelengths for Ag spheres, pentagons and triangles with various sizes (figure adapted from [53]).

Another commonly used modification of the morphology to control and tune the optical properties of metal nanostructures is creating hollow nanostructures [61]. Here, we present a set of calculations that we have conducted based on the Mie theory [62] in idealized hollow Ag and Au spherical nanoparticle systems. Here we assume perfectly symmetrical void/Ag and void/Au systems with different void sizes as shown in the accompanying sketches (Fig. 1.11). As seen in these figures, even the smallest change in the void size modulates the plasmon resonance significantly. These calculations clearly reveal the extend of plasmon resonance engineering by hollow nanostructures, which is the main motivation of the experimental and simulation studies conducted during this thesis manuscript. The changes observed are mostly due to a mechanism called plasmon hybridization [63], which will be explained in detail in the following. It is also worth noting here that the extinction efficiency of Ag nanostructures are a lot higher than those of Au nanostructures, which can be understood by considering the above mentioned (Fig. 1.2) differences in interband transition effects for Ag and Au, resulting the presence of more intense and sharp plasmon peaks for Ag nanostructures [53, 64].

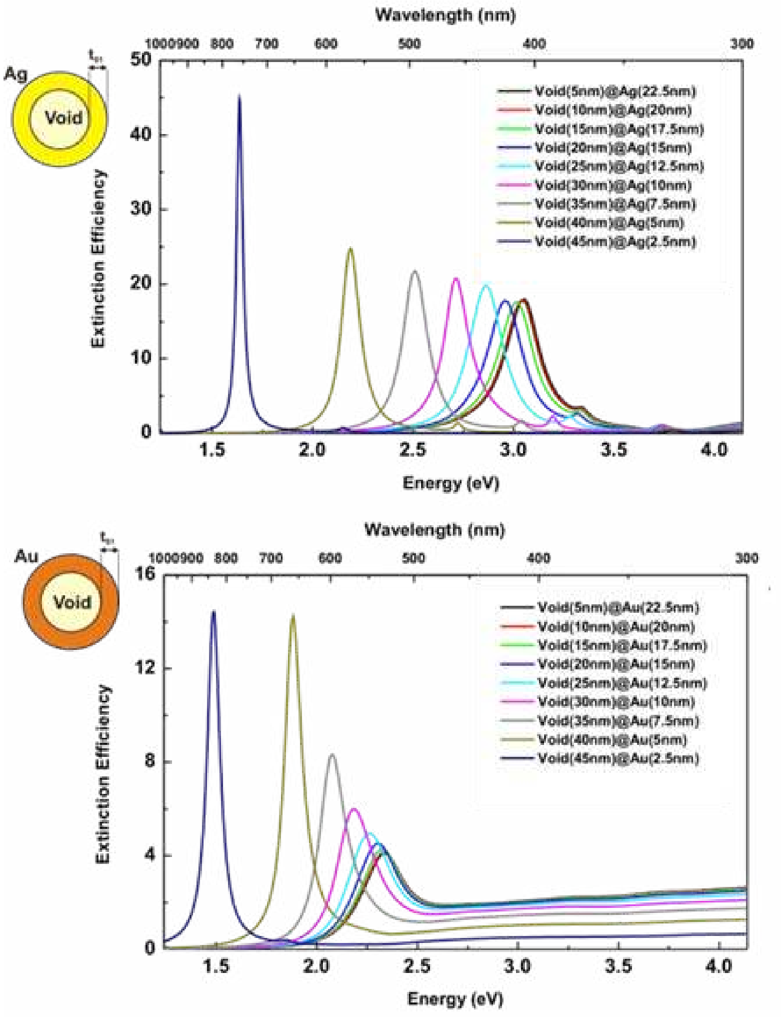

FIGURE 1.11: Mie calculations for idealized void/Ag (upper) and void/Au (lower) spherical systems with a total diameter of 50 nm, where the shell thickness varied between 2.5 nm and 22.5 nm.

As seen in Fig. 1.10B, the difference between the plasmon resonances of truncated octahedron, cuboctahedron, truncated cube and cube nanostructures is quite negligible. The fact that nanostructures with different morphologies can have similar plasmon resonance energies arises the question about the determination of shape effects on the LSPR properties. As the LSPRs are constrained by the morphology of the nanostructures, their shape must have crucial effects on the LSPR properties. However, the differences on the plasmonic properties may not always be manifested in plasmon resonance energies, as it is the case for the above presented polyhedral Au nanostructures. The distribution of the plasmon resonances is equally important as the plasmon resonance energy for many applications and it can not be distinguished by the UV-Vis spectroscopy. For instance, Chen et al. [56] reported the shape dependent refractive index sensitivities of various Au nanostructures that have the same plasmon resonance wavelengths, yet, the distribution of plasmon resonances for each nanostructure is different (shown in Fig. 1.12). Fig. 1.12 shows the TEM micrographs and electric field enhancement contours of various Au nanostructures such as nanorods with different size and shapes, nanobipyramid, and oxidized nanorod and nanobipyramids. Altough their corresponding extinction spectra reveal that they have almost the same plasmon resonance wavelengths, their distribution is different for each nanostructure resulting in 2-fold differences during refractive index sensing [56]. In general, it is safe to say that even slight variations in the morphology generate plasmon resonances with different energies and/or different distributions. For instance, Qian et al. [59] reported the effects of edge rounding on the plasmonic properties of nanocube and nanobox-like structures and concluded that, along with its effects on the distribution, plasmon resonances shifted to higher energies for the nanocubes/-nanoboxes with rounded edges compared to those of with sharp edges.

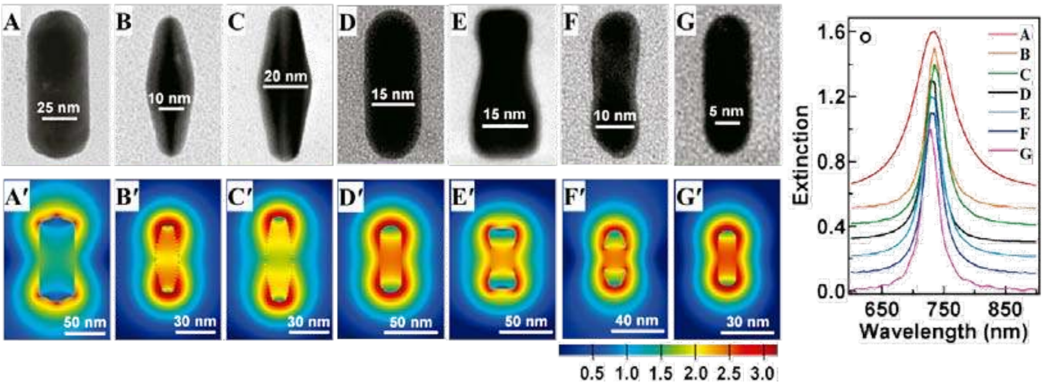

FIGURE 1.12: TEM micrographs of Au nanostructures: (A) large nanorod, (B) nanobipyramid, (C) oxidized nanobipyramid, (D) oxidized nanorod, (E) dog-bone-like nanorod, (F) peanut-like nanorod and (G) small nanorod. Their corresponding electric field enhancement contours (at the logaritmic scale) are presented in the lower row. The extinction spectra of the nanostructures are shown on the right (figure adapted from [56]).

1.2.3 Composition effects

Composition of the plasmonic structure is another crucial parameter on the plasmonic properties. As it is discussed during the previous section based on the dielectric constant of different materials (for instance, see Fig. 1.2) and indirectly shown during the above sections about size and shape effects (for instance, see Fig. 1.10), a material's plasmon resonance is highly dependent on its composition. Before starting showing solely compositional effects on the plasmonic properties of different nanostructures, we find it convenient to mention about the galvanic replacement process, where the modulation in the plasmonic properties can be accounted both as morphological and chemical manipulations [50, 61, 65–69]. It should be noted here that the hollow metallic nanostructures studied in this thesis manuscript are also synthesized by the galvanic replacement reaction [69], details of which will be presented in Chapter 2.

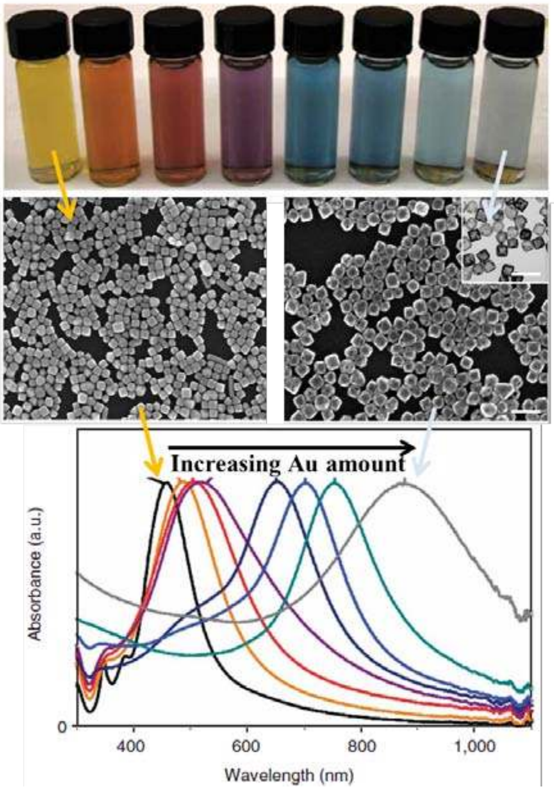

Figure 1.13: (Upper row) Photographs of solutions at different stages of galvanic replacement reaction, where Ag nanocubes (far left) are used as templates to synthesize AuAg nanocages (far right). (Middle row) TEM micrographs of Ag nanocubes and AuAg nanoscages. (Lower row) UV-Vis spectra obtained from the different stages of the reaction, where the amount of Au increased from left to right. Colored arrows indicate the photographs and UV-Vis spectra corresponding to the initial Ag nanocubes and final AuAg nanocages (figure adapted from [65]).

As the differences between Ag and Au nanostructures are also mentioned above while discussing the size and shape effects, we will shortly talk about the alloyed nanostructures and the effects of chemical composition on their plasmonic properties. This issue is also widely investigated in the literature in various experimental and simulation studies [70–78].

We must stress here that most of the studies reporting the effects of composition on the optical properties of metallic nanostructures tend to disregard the effects of size differences of the synthesized nanoparticles. Liu et al. [79] investigated the effects of composition on optical properties of mono-disperse AuAg alloy nanoparticles (Fig. 1.14). They have synthesized mono-disperse nanoparticles with different AuAg compositions, all of which have an average diameter of ∼6 nm. As seen in the UV-Vis spectra, the plasmon resonance peak shifts to higher wavelengths (lower energies) as the amount of Au increases, in fact, the plasmon resonance wavelength is dependent on the Au amount showing a perfect linear relation [79], which was also reported in [70].

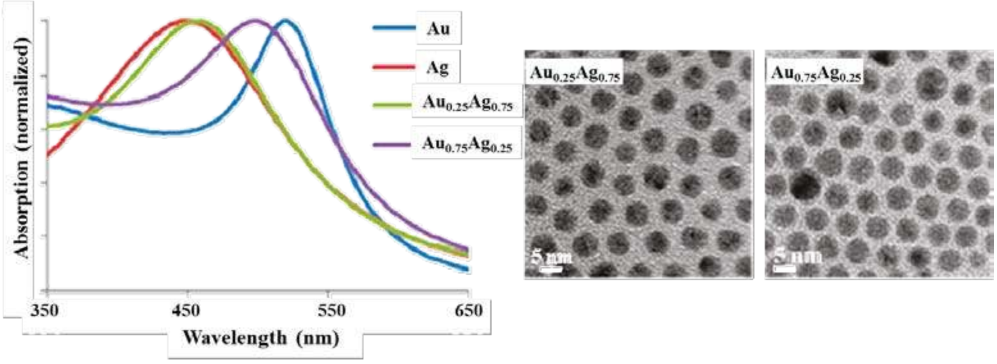

FIGURE 1.14: UV-Vis spectra of several AuAg alloy nanoparticles with different compositions, along with the TEM micrographs taken from the $Au_{0.25}Ag_{0.75}$ and $Au_{0.75}Ag_{0.25}$ nanoparticles revealing the size homogeneity within and between the samples. Note that the AuAg alloy nanoparticles have similar sizes of ∼6 nm for all compositions (figure adapted from [79]).

Another issue to be taken into account is the distribution of the composition, i.e. alloy formation or segregated alloys/heterostructures/core-shells etc. The formation of alloys for the spherical nanoparticles, to some extend, can be directly detected by the shape of the UV-Vis spectra, where the optical absorption spectrum of the alloys reveals the presence of only one plasmon band (note that it is only valid for the small sized spherical nanoparticles) [70, 74, 80, 81]. For instance, Fig. 1.15 shows the absorption spectra taken from $Au_{0.5}Ag_{0.5}$ nanoparticles with an average size of 13 nm. As seen in this figure, the absorption spectrum of the alloyed $Au_{0.5}Ag_{0.5}$ nanoparticles (in red) shows the presence of one peak generated by combined resonances of the alloy, whereas the absorption spectrum taken from the $Au_{0.5}Ag_{0.5}$ nanoparticles formed by physically mixing 50% Au and 50% Ag nanoparticles shows the separate plasmon resonances associated to Au and Ag nanoparticles.

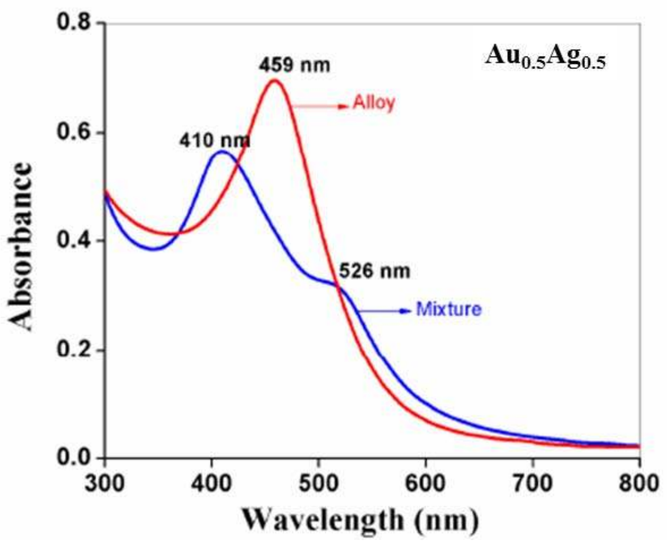

FIGURE 1.15: Absorption spectra taken from ~13 nm $Au_{0.5}Ag_{0.5}$ nanoparticles formed an alloy (in red) and mixing Au and Ag nanoparticles (in blue) (figure adapted from [74].

1.2.4 Environmental effects

The plasmonic properties of the nanostructures are highly affected by the environment. In the previous section (1.1), we have described in detail the theoretical background of the dependency of the optical properties on the dielectric constant of the environment. The fact that plasmonic properties of nanostructures are highly dependent on the surrounding medium forms the basis of plasmonic sensing [82–84], which will be elaborated in the following section. Yet, it should be pointed out that we also take into account the presence of substrate, which also affects the plasmonic properties remarkably [38, 47, 85–92], when we mention about the environmental effects.

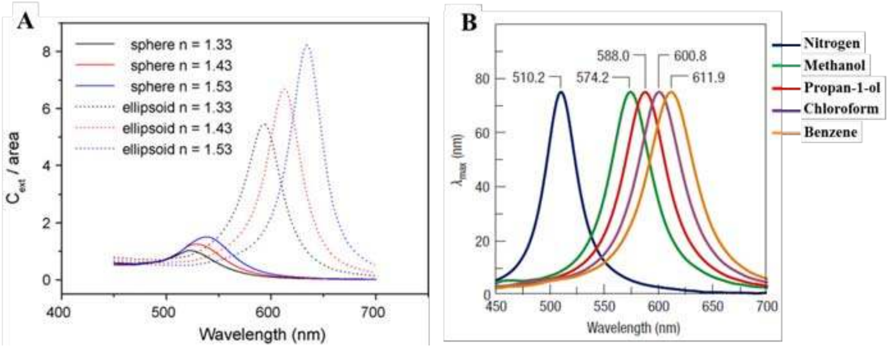

FIGURE 1.16: A. Comparison of the extinction cross-sections of 20 nm Au nanospheres and ellipsoids with aspect ratio 2 in different dielectric environment (figure reproduced [82]). B. Resonant Rayleigh scattering spectra obtained from a single Ag nanoprism in various solvent environments (figure adapted from [83]).

Fig. 1.16A shows the comparison of extinction cross-sections of 20 nm Au nanospheres and ellipsoids (with aspect ratio of 2) in different environments whose refractive index n = 1.33, 1.43 and 1.53 [82]. As seen in this figure, the peaks shift to higher wavelength as the refractive index increases and the difference is more significant for the ellipsoid Au nanostructures. Another example about the plasmonic behavior of nanostructures in different environments is shown in Fig. 1.16B where the resonant Rayleigh scattering spectra obtained from a single Ag nanoprism in different chemical solvents such as nitrogen, methanol, propan-1-ol, chloroform and benzene [83]. About 100 nm difference in scattering wavelength can be observed between the nanoparticle in nitrogen and in benzene.

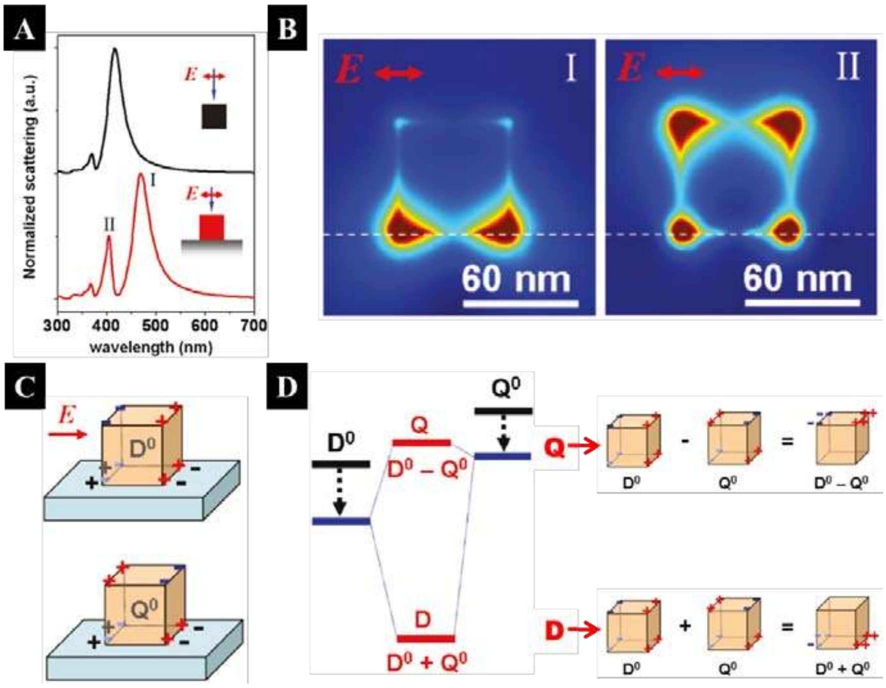

FIGURE 1.17: A. Scattering spectra of a 60 nm Ag nanocube in vacuum (in black) and on a glass substrate (in red). B. Electric field enhancement maps of two resonances labeled as I and II in A. C. Schematics of charge distributions showing the primitive dipolar (D^o) and quadrupolar (Q^o) modes. D. Energy diagram and schematic of the substrate effect leading the formation of hybridized bonding D and anti-bonding Q modes (figure adapted from [91].

Zhang et al. [91] reported the formation of substrate-induced fano resonances in a Ag nanocube (Fig. 1.17). Fig. 1.17A shows the scattering spectra obtained from a 60 nm Ag nanocube standing in vacuum (in black) and on a glass substrate (in red). As seen in this figure, plasmon resonance of the nanocube in vacuum shifts to higher wavelength (labeled as I) and a new mode (labeled as II) emerges due to the substrate effects. Fig. 1.17B shows electric field enhancement maps corresponding to the modes labeled as I and II, revealing that mode I is confined in the region that is in contact with the substrate and mode II is present more intensely at the upper part. The schematics of charge distribution showing the primitive dipolar (D^o) and quadrupolar (Q^o) modes are shown in Fig. 1.17C. As the distribution of these primitive modes can not explain the electric field enhancement maps, a hybridization model is proposed (Fig. 1.17D), which results in the generation of hybridized bonding D and antibonding Q modes [91]. These bonding and anti-bonding modes are usually referred as proximal and distal modes, respectively, and they will be used as such throughout this thesis manuscript.

Nicoletti et al. [90] reported the distribution of multiple proximal and distal modes in a 100 nm Ag nanocube experimentally by three-dimensional EELS analyses. More recently, Li et al. [92] showed the energy transfer from plasmonic Ag nanocubes to different semiconducting substrates such as amorphous silicon (a-Si) and boron phosphide (BP) and to an insulating substrate of silicon dioxide (SiO_2). A hybridization model, similar to the one presented in Fig. 1.17D, is suggested, where the model is further expanded to the dependency of the dielectric constant of the substrate.

In this thesis manuscript, we have obtained the EELS data from the nanostructures deposited on 15 nm thick Si_3N_4 grids for the results presented in Chapters 3 and 4, whereas the results presented in Chapter 5 are obtained by using 18 nm thick SiO_2 grids. In Chapters 3 and 4, we have discussed the effects of Si_3N_4 grids on the plasmonic properties of hollow AuAg nanostructures.

1.2.5 Plasmon coupling

Another factor that affects the plasmonic properties of metal nanostructures is the presence of another metal nanostructure nearby, what is known as plasmon coupling [93]. When two metal nanostructures are placed close to each other, their LSPRs interact with each other and create electric field enhancements in the gap region that are much larger than those for the isolated nanostructures. This enhancement is investigated widely for many different nanostructures with many different alignments as it significantly increases the efficiency of plasmonic applications, especially in sensing and surface enhanced Raman scattering leading the way to the detection of single molecules [94–105].

The interaction between plasmon fields of adjacent nanostructures modulates the energy of plasmon resonances, where, as a universal rule in the classical regime, plasmon resonances shift to lower energies with decreasing gap sizes. Having said that, one needs to take the quantum effects into account for very narrow gaps, where the electron conduction plays an important role and diminishes the coupling plasmon strength (for instance see the chapter in [93] on quantum plasmonics in coupled nanoparticles with narrow gaps). Scholl et al. [106] experimentally observed quantum tunneling between two plasmonic Ag nanoparticles with a gap ∼0.5 nm. More recently, Tan et al. [107] observed quantum tunneling between two adjacent Ag nanocubes, where they could increase the gap up to 1.3 nm for the charge transfer via quantum tunneling thanks to bridging by self-assembled monolayers.

Fig. 1.18 shows two examples of plasmon coupling between nanodisks and nanotriangles (so-called bowtie nanoantennas), with gaps in the classical regime (figures adapted from [96, 105]). Fig. 1.18A shows a typical SEM micrographs of Au nanodisk pairs with 12 nm gaps, where the individual nanodisk is 88 nm in diameter and 25 nm in thickness. DDA-simulated extinction efficiencies versus the interparticle gaps are shown in Fig. 1.18B, revealing that the extinction efficiency icreases and the peaks shift to higher wavelengths as the interparticle gap gets narrower [96]. Another typical example of plasmon coupling is so-called bowtie nanoantennas. Fig. 1.18C shows the simulated electric field contours of bowtie nanoantennas with parallel and perpendicular polizations. Fig. 1.18D and Fig. 1.18E shows the Raman spectra and enhancement factors for different gaps, where the Raman signal and thus, enhancement factor significantly increase as the gaps get narrower [105].

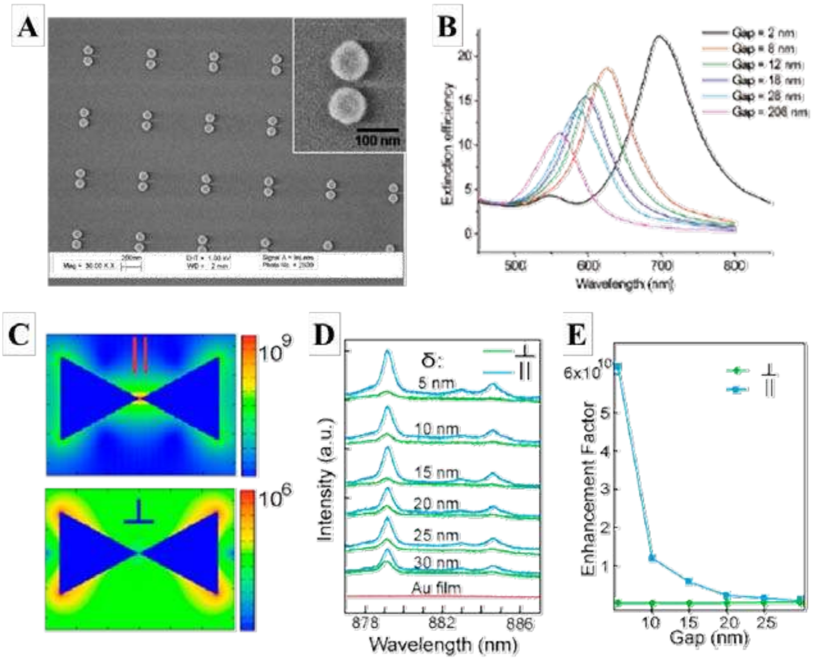

FIGURE 1.18: A. Representative SEM micrograph of Au nanodisk with a gap ∼12 nm. B. DDA-simulated extinction efficiency for varying interparticle gap for parallel incident light polarization direction (figures adapted from [96]). C. Simulated electric field contours of bowtie nanoantennas with parallel and perpendicular polizations. D. Raman spectra and E. enhancement factor for varying gap size between nanoantennas (figure adapted from [105]).

Plasmonic coupling between two Ag@Au core-shell nanocubes separated with a ∼22 nm gap and between an Ag@Au core-shell nanocube and an AuAg nanoframe separated with a ∼14 nm gap are presented in Chapter 5 with 3D EELS analyses.

1.2.6 Plasmon hybridization in void plasmons

We have already introduced the term of plasmon hybridization in several occasions above (for instance, see Fig. 1.11 and Fig. 1.17). Plasmon hybridization mechanism, developed by Prodan et al. [63], is a model that explains the plasmon resonances of complex nanostructures with complex geometries as the interaction or ”hybridization” of plasmons generated by simpler geometries (Fig. 1.3). This principle has opened the way to rational designs of complex nanostructures with desired plasmonic properties by a simple approach [108]. Although it has also been widely used to explain the interaction between two solid nanostructures, or solid nanostructure/environment interactions [91, 92, 102, 109–112], we will focus on its application for the plasmonic properties of the hollow nanostructures during this section [63, 108, 113, 114]. We use the term of ”void plasmons” for the plasmon resonances generated in the hollow nanostructures [2] and note that they are also known as cavity plasmons.

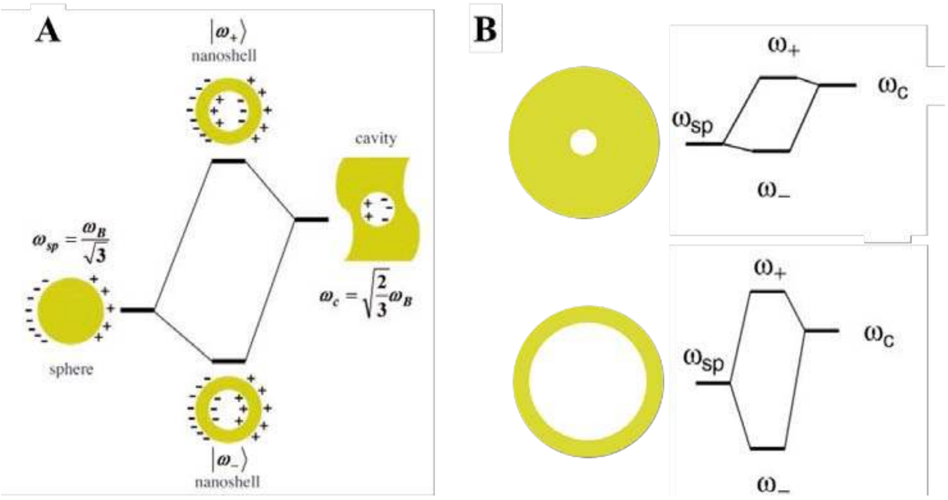

FIGURE 1.19: A. Schematic energy-level diagram illustrating the plasmon hybridization mechanism in metal nanoshells as a result of the interaction between the sphere and cavity plasmons. Anti-symmetrically coupled, anti-bonding, mode (ω_+) and symmetrically coupled, bonding, mode (ω_-) are shown (reproduced from [115]). B. Extend of the hybridization for thick (upper) and thin (lower) metallic shells revealing that the hybridization is much higher for the thin metallic shell (figure adapted from [116]).

Fig. 1.19A shows the schematic of plasmon hybridization mechanism developed by Proden et al. [63], where the energy-level diagram describing the mechanism in metal nanoshells as a result of the interaction between the sphere and cavity plasmons. The plasmon resonances present in the metallic shell are identified as anti-symmetrically coupled anti-bonding mode (ω_+) and symmetrically coupled bonding mode (ω_-). Fig. 1.19B shows the plasmon hybridization mechanism in metal nanoshells with different shell thicknesses and reveals that the interaction of plasmon resonances, thus, plasmon hybridization is much higher for the thin metallic shells [116].

As this thesis manuscript is about nanoenginnering of plasmon resonances in hollow nanostructures, it is convenient to elaborate the physics behind such a mechanism. Let us assume a metallic structure containing dielectric inclusions with dimensions a (where a $\ll \lambda$). Similar to the hybridization model presented in Fig. 1.19A, we have a nanovoid with a radius r = a, which has a dielectric constant ϵ_m in a homogeneous metallic body with a dielectric constant $\epsilon(\omega)$ (Fig. 1.20).

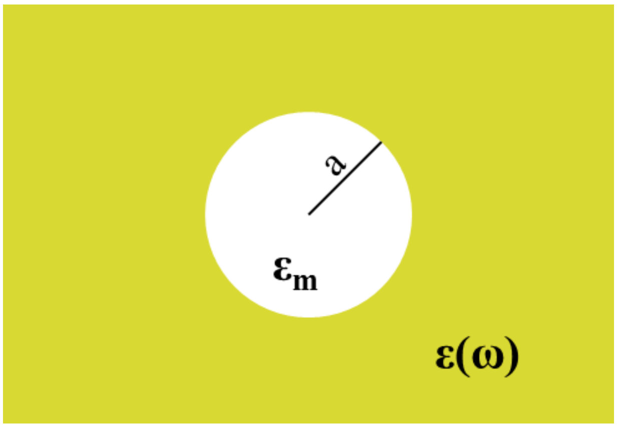

FIGURE 1.20: Spherical dielectric *nanovoid* in a homogeneous metallic body.

This dielectric nanovoid can sustain an electromagnetic dipole resonance analogous to a metallic nanoparticle. Simply, we can imagine this system like a spherical metallic nanoparticle with a dielectric constant ϵ_m placed in an environment with a dielectric constant $\epsilon(\omega)$. Simply changing $\epsilon(\omega)$ (or ϵ_{sph}) $\rightarrow \epsilon_m$ and $\epsilon_m \rightarrow \epsilon(\omega)$ in equation (1.43), we can express the polarizability of the nanovoid as [2]:

$$\alpha = 4\pi a^3 \frac{\epsilon_m - \epsilon}{\epsilon_m + 2\epsilon}. \tag{1.46}$$

Note that the induced dipole moment is oriented antiparallel to the applied outside field in this case, contrary to metal nanoparticles [2]. The Fröhlih condition becomes

$$\mathbf{Re}\left[\epsilon\left(\omega\right)\right] = -\frac{1}{2}\epsilon_m. \tag{1.47}$$

As shown in the hybridization model in Fig. 1.19A two fundamental dipolar modes of a void/shell nanoparticle system can be considered as they emerged by the hybridization of dipolar modes of a metallic sphere and a dielectric void in a metallic substrate. [63]. As a result of this hybridization, a bonding mode and an anti-bonding mode are generated in the metallic nanoshell. Validity of this model is proven by quantum-mechanical calculations and finite-difference time-domain simulations [115, 117, 118]. If one describes the particle plasmon as an incompressible deformation of the conduction electron gas of the metallic nanostructure, such deformations can be expressed by using spherical harmonics of order l [63]. The frequencies of the hybridized plasmon resonances ($\omega_{l\pm}$) can be written as for each $l > 0$ [63],

$$\omega_{l\pm}^2 = \frac{\omega_p^2}{2}\left[1 \pm \frac{1}{2l+1}\sqrt{1 + 4l(l+1)(\frac{a}{b})^{2l+1}}\,\right], \tag{1.48}$$

where a and b are the inner and outer radius of the shell, respectively.

The plasmon hybridization model can explain the interactions between the plasmon resonances of more complex systems such as double-shell metallic nanoparticles [63]. Recently, it has been implemented to explain quantum plasmonics in a complex system of so-called "nanomatryushka" [119]. Fig. 1.21 shows the geometry of a nanomatryushka (Fig. 1.21A) and induced electric field distributions for the modes located at 1.81 eV (top) and 2.87 eV (bottom) with varying component sizes (Fig. 1.21B) as indicated in paranthesis below the figures where the colors correspond to the colors of the arrows in the geometry. For a total nanomatryushka size of ∼8 nm, the induced field maps fit well with the classical modeling, where the mode located at 1.81 eV induces a strong field in the core-shell gap and the mode located at 2.87 eV induce strong field both in the gap and outside of the shell. As the diameters (given in parenthesis, in nm) get smaller, the electric field inside the gap diminishes gradually. In the size regime of ∼1.5 nm nanomatryushka, similar to above mention plasmon coupling in quantum regime, charge transfer between the core and shell becomes so strong and the nanomatryushka system acts like a spherical nanoparticle [119]. Fig. 1.21C shows the plasmon hybridization diagram between the nano-core and nano-shell, resulting in the generation of bonding hybridized plasmon resonance located at 1.81 eV ($\omega_-{}^- >_{NM}$) primarily due to hybridization of nano-core plasmon mode ($\omega_- >_{NC}$) and the bonding shell plasmon mode ($\omega^- >_{NS}$). The higher energy dipole mode located at 2.87 eV ($\omega_-{}^+ >_{NM}$) is created from the nano-core plasmon mode and the anti-bonding shell plasmon mode ($\omega^+ >_{NS}$) with a slight admixture of bonding shell plasmon mode. A third non-bonding mode ($\omega_-{}^+ >_{NB}$) is also predicted as an anti-bonding combination of the nano-core resonant mode and the anti-bonding resonant mode of the shell, which was not visible in the spectrum due to its low dipole moment [119]. Fig. 1.21D shows the schematic surface charge distribution corresponding to the modes located at 1.81 eV (left) and at 2.87 eV (right).

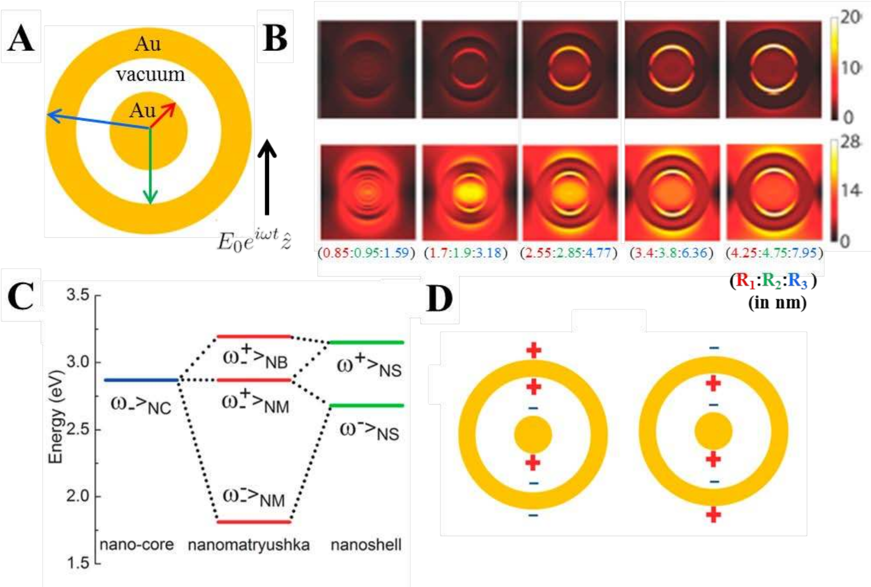
A
Au
vacuum
Au
$E_0 e^{i\omega t}\hat{z}$
B
20
10
0
28
14
0
(0.85:0.95:1.59) (1.7:1.9:3.18) (2.55:2.85:4.77) (3.4:3.8:6.36) (4.25:4.75:7.95)
(R1:R2:R3)
(in nm)
C
Energy (eV)
3.5
3.0
2.5
2.0
1.5
ω->NC
ω+->NB
ω+->NM
ω->NM
ω+>NS
ω->NS
nano-core
nanomatryushka
nanoshell
D
+
-

FIGURE 1.21: A. Geometry of a nanomatryushka, consisting of a spherical Au nanoparticle/void/Au nanoshell system. B. Induced electric field distribution for the two modes located at 1.81 eV (top) and 2.87 eV (bottom). Distances between the components (shown with colored arrows in A) increase from left to right, which are given in parenthesis with colors corresponding to the color of the arrows. C. Plasmon hybridization diagram, where the NC is nanocore, NS is nanoshell, NB is nonbonding and NM is nanomatryushka. D. Schematic surface charge distributions for the modes located at 1.81 eV (left) and 2.87 eV (rigt) (figure adapted from [119]).

As shown here the plasmon hybridization model can be used to explain plasmon resonances generated by voids in metal nanostructures. Therefore, we will use this model in order to explain and understand the plasmon resonances of hollow AuAg nanostructures synthesized by galvanic replacement reaction [69] investigated during this thesis manuscript, as it is also suggested by [61, 66, 67].

1.3 Applications of plasmonic nanostructures

Plasmonic nanostructures can be termed as nanoantennas with an anology to radio antennas as their EM modulation mechanism is quite similar to those of the radio antennas [120, 121]. They have the ability to direct and enhance radiative emission (and vice versa) in transmission mode and they can convert propagating free-space EM wave to highly confined and strongly enhanced electric fields [120–125]. With the ability of the localization of light at nanoscale, plasmonic nanostructures are attractive building blocks for nano optics and novel applications such as sensor devices [126], surface enhanced Raman spectroscopy (SERS) [127], photovoltaics [128], theranostics [68], superlenses [129], nanolasers [130], invisibility cloaks [131] and quantum computing [132] among others. In this section, we will give some information about most common applications of plasmonic nanostructures such as sensing, SERS, photovoltaic solar cells and nanomedicine.

1.3.1 Plasmonic nanosensing

As mentioned extensively in the previous section, LSPR properties of nanostructures are known to be highly sensitive to the local environment, as well as to their size and shape. Label-free optical sensing with plasmonic nanoparticles is based on the detection of adsorbate induced refractive index changes near or on the nanoparticles, which change the dielectric constant of the surrounding medium and can be measured by using UV-visible extinction spectroscopy [83, 84, 126, 133]. Adsorbate induced shifts in LSPR can be expressed as $\Delta\lambda_{max}$, which is simply given in the equation (1.49) [84]:

$$\Delta\lambda_{max} = \lambda_{max} < after > -\lambda_{max} < before > . \tag{1.49}$$

Early biosensing experiments are based on the label-free colorimetric assays where the color change produced by aggregation of Au colloids are used as probes to detect interactions between DNA stands [82]. The color change in this simple setup can be visualized even with "naked" eye. A schematic representation of colorimetric detection of nucleic acid sequences is shown in Fig. 1.22A. In this strategy two metal nanoparticle colloids, each capped with a different and non-complementary single stranded DNA (ssDNA) are mixed together (which are labeled as DNA-Au NP probes in the figure). Further addition of a third oligonucleotide induces aggregation due to the hybridization between the oligonucleotides resulting in change of color of the colloidal solution [82, 134]. The color changes are amplified when the aggregates are visualized on a chromatographic plate such as glass, and by this way, detection limits in zeptomolar range (about 600 molecules) can be obtained [134]. This technique is quite versatile and can be applied easily to different bio-molecular detection and medical diagnostic applications [135–138].

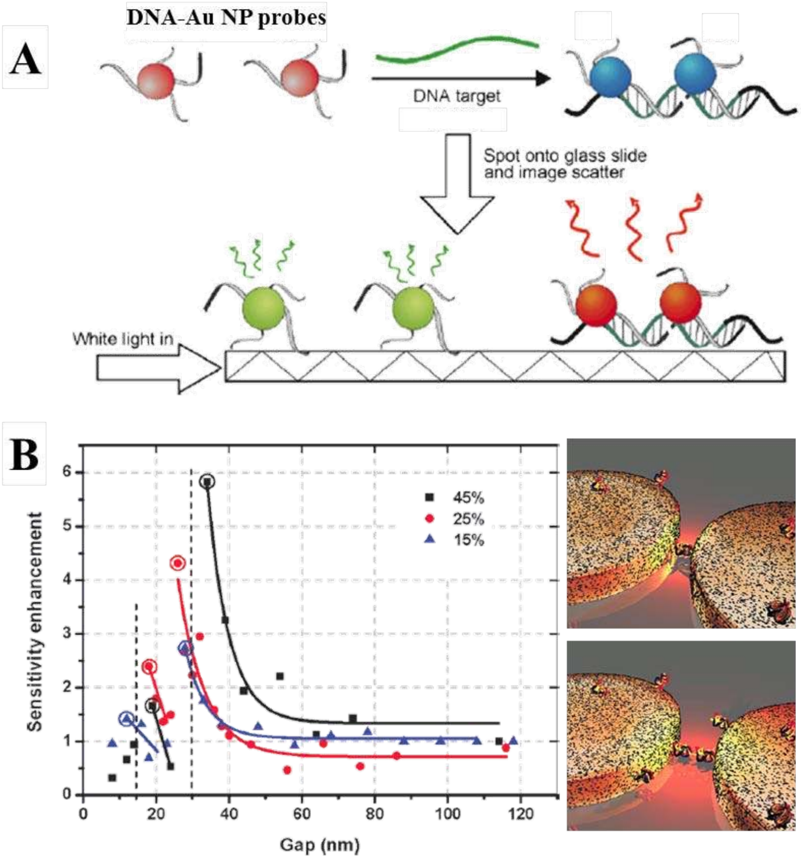

FIGURE 1.22: A. Schematics of colorimetric detection of nucleic acid sequences: DNA-Au nanoparticle probes are hybridized to a DNA target in solution and deposited onto a glass substrate, which is then illuminated with white light. The Au nanoparticles having 40-50 nm diameter scatter green light, whereas completed DNA-Au nanoparticle probes scatter yellow to orange light (figure reproduced from [134]). B. Bovine serum albumin (BSA) sensing with Au nanodimers, where sensing enhancement versus the gap size between dimers are shown for different BSA coverage amounts. On the right, schematics of BSA molecules located at the interparticle gap (figure adapted from [101]).

It has been reported that by carefully engineering the nanoparticle assemblies, it is possible to visualize single binding events such as DNA hybridization and protein conjugation [95, 101]. As mentioned above, plasmon coupling enhances the efficiencies of plasmonic applications due to the presence of highly enhanced fields in the gap between two interacting nanostructures. Such an enhanced fields can be exploited to detect single protein binding events [101]. Fig. 1.22B shows the sensitivity enhancement of Au nanodimers towards bovine serum albumin (BSA) protein sensing by different interparticle gaps. The percentages shown in this figures represent the BSA coverage of Au dimers. On the right, schematic of nanodimer-protein interactions is shown, where one (top) or two (down) BSA molecules are located at the gap region [101].

Hollow nanostructures are known to have better sensing properties than their solid counterparts due to the above mentioned plasmon hybridization mechanism [63] resulting in the enhanced plasmon fields along with more homogeneous distribution [67, 139, 140]. For instance, Sun and Xia [141] compared the sensitivity of Au nanospheres and nanoshells and reported that a SF of 60 nm/RIU measured for the solid nanosphere becomes 409 nm/RIU for the case of a hollow nanoshell of the same size, which corresponds to almost a 7 fold increase in the SF. Similarly, in their review article, Mahmoud et al. [140] tabulated a 5 fold increased SF when comparing Au nanocubes and hollow Au nanocages. Fig. 1.23A shows the modulation of LSPR peak positions for Au nanoframes (NF) with different edge lenghts and wall thicknesses, which are simulated by discrete dipole approximation (DDA) assuming perfect shapes [67]. As seen in this figure, even the sub-nanometer changes in the wall thickness result in significant changes in the LSPR peak position, suggesting their high sensitivity to the modifications. In order to prove that, plasmon resonances of Au NFs with 40 nm and 90 edge lengths are simulated for the NFs located in different environments with different refractive indexes. Fig. 1.23B shows the DDA simulated extinction spectra of 40 nm NF with 7.2 nm thick walls surrounded by different media. As seen in these figure, about the peak located at about 900 nm for the NF in air shifts to about 1150 nm for the NF in water. For the 40 nm Au NF with 7.2 nm thick walls a high sensitivity factor of 739 nm/RIU is calculated [67]. Fig. 1.23C the DDA simulated extinction spectra of 90 nm NF with 21.6 nm thick walls surrounded by different media and indicates a sensitivity factor of 494 nm/RIU.

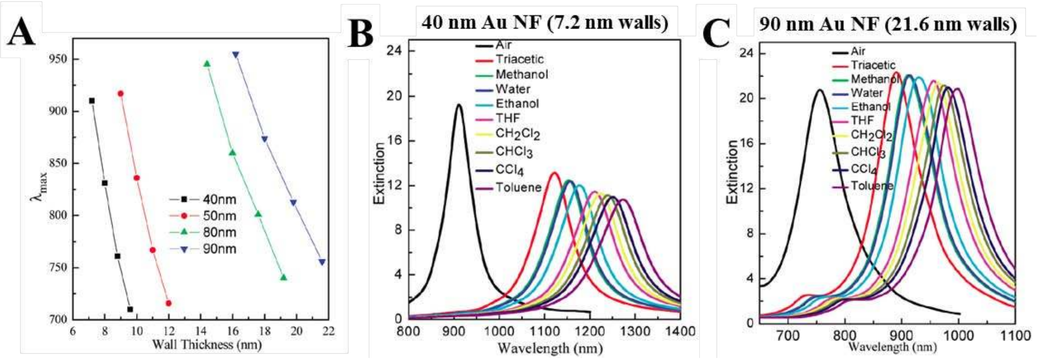

FIGURE 1.23: A. DDA simulated plasmon resonance maximum peak positions for Au nanoframes (NF) with different edge lengths and wall thicknesses. B. DDA simulated extinction spectra of 40 nm Au NFs with 7.2 nm thick walls in various environments. C. DDA simulated extinction spectra of 90 nm Au NFs with 21.6 nm thick walls in various environments (figure adapted from [67]).

In Chapter 2 of the present thesis manuscript, we will measure the sensitivity of single-walled AuAg nanoboxes and solid Au nanoparticles against conjugation events with BSA and its antibodies, in order to reveal the effects of enhanced plasmonic properties of such nanostructures on their sensitivity.

1.3.2 Surface-enhanced Raman spectroscopy

Surface-enhanced Raman spectroscopy (SERS), a technique where the enhanced Raman scattering is obtained due to the localization and amplification of incident light fields by a surface plasmon resonance, is arguably one of the most common applications of plasmonic nanostructures since its discovery about 40 years ago [142–144]. With the developments in the spectroscopic information and nanofabrication techniques and novel detection schemes, SERS has been established as a powerful tool in sensing and detecting in molecular level [127, 145].

After the pioneering works of Nie and Emory [146] and Kneipp et al. [147] reporting the ability of SERS for single molecule detection, it has extensively been exploited for the detection of different molecules at single molecule level [148–151] and for detection of disease markers [152–154]. Moreover, utilization of SERS in living cells [155] and in-vivo tumor targeting and spectroscopic detection [152] has been realized. Fig. 1.24A shows the schematics of cancer cell targeting and spectroscopic detection by using antibody-conjugation SERS. Spherical Au nanoparticles with ∼60 nm in diameter are stabilized with thiol-polypolyethyleneglycol (thiol-PEG) and used as the plasmonic component during targeting and SERS. Fig. 1.24B shows the SERS spectra obtained in-vivo from the cancer cells along with the control data and standard tag spectrum [152].

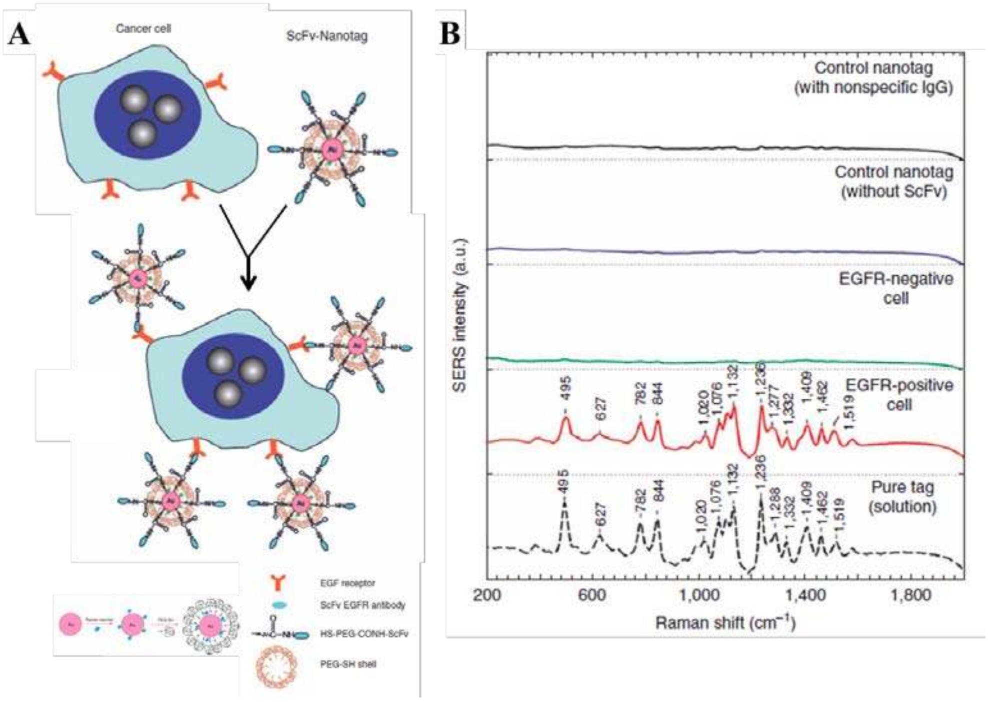

FIGURE 1.24: A. Schematics of cancer cell targeting and spectroscopic detection by using antibody-conjugated SERS where Au nanoparticles stabilized with thiol-polyethyleneglycol (thiol-PEG) are used as plasmonic component. B. SERS spectra obtained in-vivo from the EGFR-positive cancer cells and EGFR-negative cancer cells along with the control data and the standard tag spectrum (figure adapted from [152]).

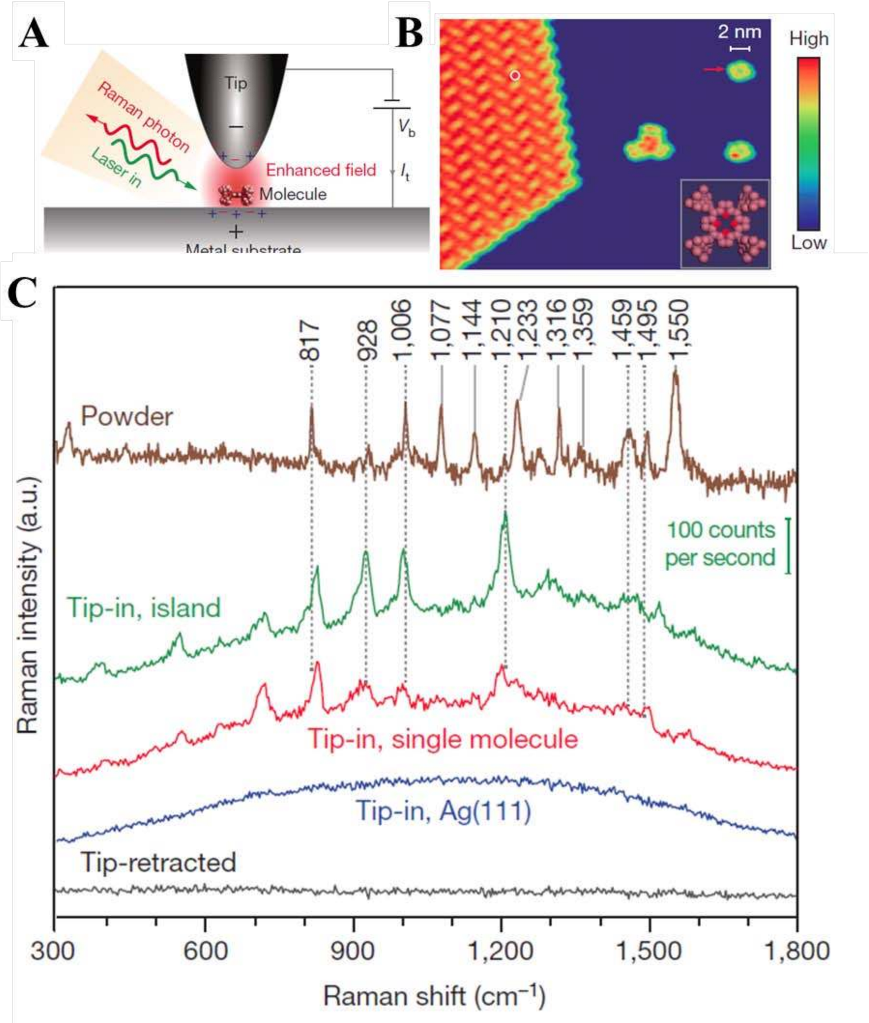

FIGURE 1.25: A. Schematic of the tunneling-controlled TERS setup. B. STM topograph sub-monolayered H_2TBPP molecules (the inset is the chemical structure of a single molecule). C. TERS spectra obtained for different conditions (figure adapted from [156]).

More recently, Zhang et al. [156] used a modified SERS system termed as tip-enhanced Raman spectroscopy (TERS) to chemically map single molecules on Ag substrates. Fig. 1.25A shows the schematic of the TERS system based on the scanning tunneling microscopy coupled with SERS providing spatial resolutions at sub-nanometer scale, i.e. sub-molecular scale. STM topograph of sub-monolayered meso-tetrakis(3,5-di-tertiarybutylphenyl)-porphyrin (H_2TBPP) molecules (the inset is the chemical structure of the molecule) on Ag(111) surface is shown in Fig. 1.25B, revealing the sub-single molecule resolution power of the setup. Fig. 1.25C shows the TERS spectra obtained from different conditions and locations such as tip-retracted TERS (i.e. standard SERS) on the Ag substrate, TERS on the substrate and TERS on single molecules, molecule islands and powders [156]. As seen in this figure, tunneling-controlled TERS setup can provide chemical information from the single molecules with sub-molecular spatial resolutions thanks to the enhanced field generated by plasmonic substrate.

1.3.3 Plasmon-enhanced photovoltaics

Photovoltaics, the conversion of sunlight to energy, have received great interest as clean and sustainable source of energy, which, ultimately, has the potential of solving the problem of climate change [128, 157, 158]. Implementation of plasmonic nanostructures to photovoltaics improve the efficiency of the devices by increasing light absorption. There has been numerous studies reporting enhancements in efficiencies of silicon and other inorganic based solar cells and organic solar cells over the years [128, 157–167].

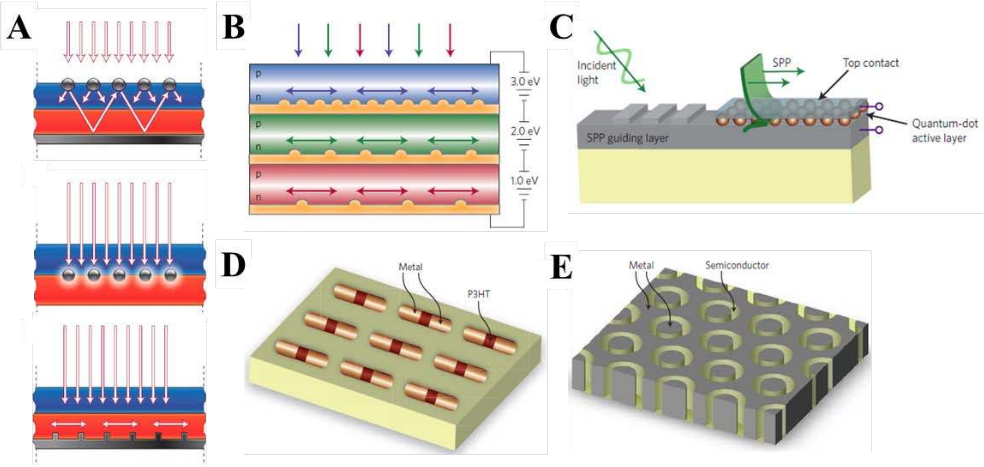

FIGURE 1.26: Different plasmonic light-trapping geometries for various solar cells. A. Three different designs for thin-film solar cells where the plasmonic nanostructures are located at the top surface of the cell, embedded in the semiconductor, and located at the metal/semiconductor interface. B. So-called plasmonic tandem geometry where the semiconductors with different bandgaps are stacked on top of each other, separated by plasmonic metal contact layer. C. Plasmonic quantum-dot solar cell with a metal/insulator/metal SPP waveguide. D. Optical nanoantenna array in organic solar cells. E. Solar cells enhanced by cavity plasmons of a metal film where the voids are filled with semiconductors. (Figure adapted from [128].)

Fig. 1.26 shows different designs for plasmonic light-trapping for various solar cells [128]. Fig. 1.26A shows three ways that reduces the physical thickness of the photovoltaic absorber layers while keeping their optical thickness constant. On top, metallic nanoparticles are used as scattering elements that couple and trap the sunlight into an absorbing semiconductor thin film. In the middle, metallic nanoparticles acts like nanoantennas where the plasmonic near-field coupled to the semiconductor increase the absorption cross-section. Lower design consists of a corrugated metallic film on the back which couples sunlight into SPP modes at the metal/semiconductor interface [128]. In addition to these three principal design presented in Fig. 1.26A, there are many other cell designs that can increase the light confinement and scattering from metal nanoparticles. Four of them are shown in Fig. 1.26. In a plasmonic ”tandem” design (Fig. 1.26B, semiconductors with different bandgaps are stacked on top of each other which are separated by a plasmonic metal layer that couples different wavelength bands into the corresponding semiconductor layer. A design utilizing quantum-dots and SPPs for solar cells is shown in Fig. 1.26C. As a result of nanoscale plasmonic solar-cell engineering, an organic photovoltaic light absorber could be integrated in the gap between plasmonic nanoantennas (Fig. 1.26D). Last example presented in this figure is a metal film with coaxial voids generating Fabry-Perot resonances and the voids are filled with semiconductor absorbers (Fig. 1.26E) [128].

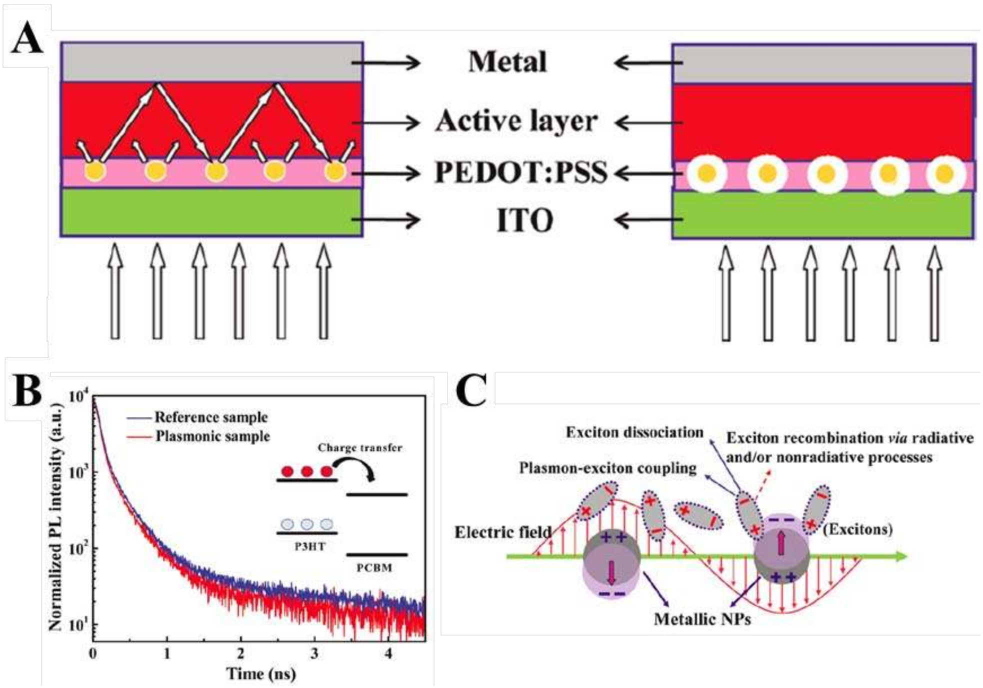
A
Metal
Active layer
PEDOT:PSS
ITO
B
Reference sample
Plasmonic sample
Charge transfer
P3HT
PCBM
Normalized PL intensity (a.u.)
10^4
10^3
10^2
10^1
0
1
2
3
4
Time (ns)
C
Exciton dissociation
Exciton recombination *via* radiative and/or nonradiative processes
Plasmon-exciton coupling
Electric field
(Excitons)
Metallic NPs

FIGURE 1.27: A. (Left) Schematic representation of light trapping due to LSPR of Au nanoparticles in an organic solar cell. (Right) Schematic of the local enhancement of the electromagnetic field, note that the plasmon field decays exponentially with increasing distances from Au nanoparticles. B. PL decay profiles of the pristine P3HT/PCMB blend sample and the plasmonic sample, where the schematic of charge transfer process is shown as inset. C. Schematic of the interplay between LSPR and the excitons where the resulting interactions enhances the rate of exciton dissociation, thus, reduces the exciton recombination (figure adapted from [168]).

Wu et al. [168] studied the surface plasmonic effects of metal nanoparticles on the performance of polymer bulk heterojunction solar cells and reported a ~33% power conversion efficiency thanks to the plasmonic nanoparticles. Fig. 1.27A shows the schematic of light trapping mechanism through forward scattering as a result of LSPRs generated by Au nanoparticles (left) and schematic of the local enhancement of the electromagnetic field (right) [168]. The plasmonic field decays exponentionally with respect to the distance from the plasmonic nanoparticles. Fig. 1.27B shows the PL decay for the initial P3HT/PCMB blend sample and sample containing plasmonic Au nanoparticles. Scheme of the charge transfer distribution is shown as an inset in this figure. Representation of the interplay between the LSPR and the excitons is shown in Fig. 1.27C, where the interactions results an enhancement of the rate of exciton dissociation, thereby reducing exciton recombination [168].

1.3.4 Applications in nanomedicine

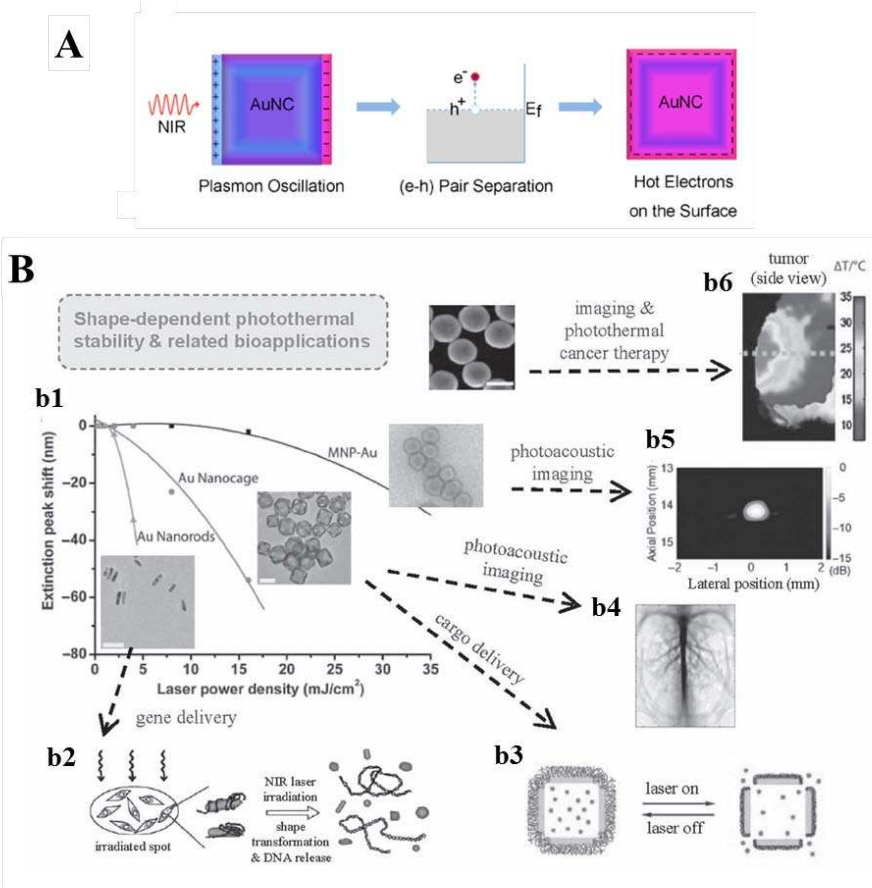
A
NIR
AuNC
Plasmon Oscillation
e⁻
h⁺
Ef
(e-h) Pair Separation
AuNC
Hot Electrons on the Surface
B
Shape-dependent photothermal stability & related bioapplications
b1
Extinction peak shift (nm)
0
-20
-40
-60
-80
Laser power density (mJ/cm²)
0 5 10 15 20 25 30 35
MNP-Au
Au Nanocage
Au Nanorods
gene delivery
b2
irradiated spot
NIR laser irradiation
shape transformation & DNA release
cargo delivery
b3
laser on
laser off
photoacoustic imaging
b4
photoacoustic imaging
b5
Axial Position (mm)
13 14 15
-2 -1 0 1 2
Lateral position (mm)
0 -5 -10 -15 (dB)
imaging & photothermal cancer therapy
b6
tumor (side view)
ΔT/°C
35 30 25 20 15 10

FIGURE 1.28: A. Schematics of heat generation by photothermal effect (figure reproduced from [169]). B. Shape dependent photohermal stability of various Au nanostructures and their related applications in nanomedicine (figure reproduced from [170]).

Thanks to their ability to absorb light and convert it to heat by a mechanism called photothermal effect, plasmonic nanoparticles have been intensively used in different nanomedicine applications such as imaging, drug delivery, cancer diagnosis and therapy [68, 169–178]. The schematic mechanism behind the heat generation by plasmonic nanoparticles is presented in Fig. 1.28A [169], where the plasmons of the Au nanocage generated by near-infrared region (NIR) illumination decay into hot electrons with energies between vacuum level and Fermi level. The heat generation in the surface hot electrons will be released to the media causing an increase in the temperature. Fig.

1.28B presents an atlas of shape-dependent photothermal stability of Au nanostructures such as nanorods, nanocages and multifunctional nanoparticles [170].

It should be noted here that most of the Au nanostructures used in nanomedicine are hollow nanostructures or nanorods due to the fact that their plasmon resonances can be finely tuned (as presented above) in the near-infrared region (NIR) where the blood and soft tissue are relatively transparent [171]. Moreover, these hollow nanostructures can be used as suitcases for drug delivery applications [68, 170, 177], where they have been employed succesfully in therapy of different kind of cancers as a less harmful alternative to standard chemotherapies [172, 178].

1.4 Characterization of LSPR properties

It is crucial to understand and manipulate LSPR properties of metallic nanostructures in order to fabricated functional devices with desired properties. Over the years, there have been many different techniques used in order to characterize plasmonic properties at different length scales. Fig. 1.29 shows an atlas of spatially-resolved spectroscopy techniques used in plasmon resonances measurements based on their spatial and energy resolutions [179]. Please note this atlas was published in 2010 and over the recent years, thanks to the developments in the instrumentation and spectroscopy techniques, there has been many reported exceeding the spatial and/or energy resolutions presented in this atlas. Even though, it is useful in order to compare different techniques and as seen here, cathodoluminescence (CL) and electron energy-loss spectroscopies (EELS) can provide information with high spatial and energy resolutions. Thus, after giving an introduction about the different techniques, we will present some examples on the plasmonic property characterizations by CL and EELS, with an emphasis on the latter.

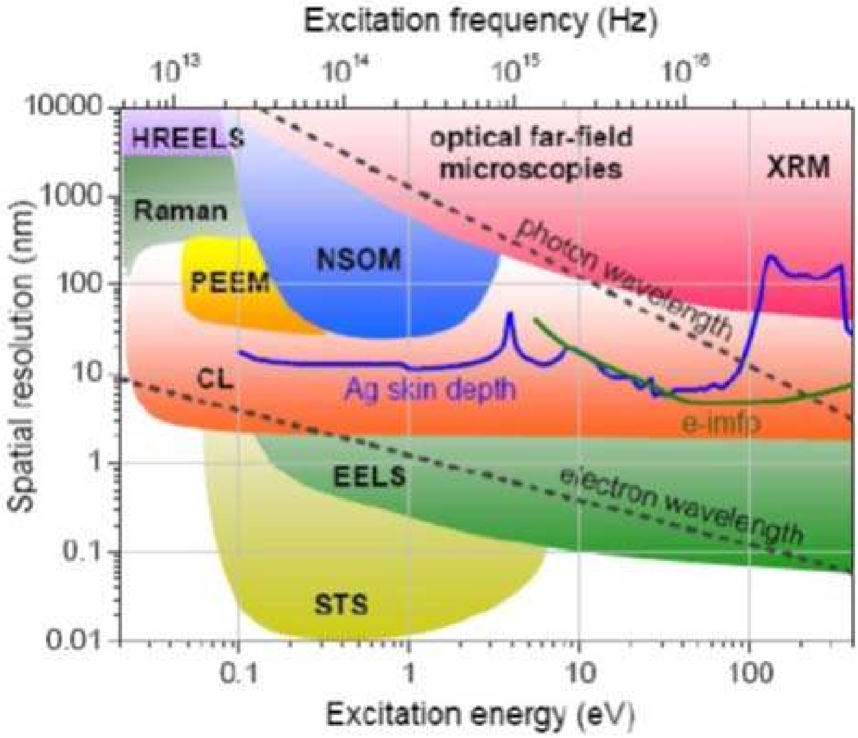

Figure 1.29: Atlas of spatially-resolved spectroscopy techniques used in plasmon resonance measurements, organized according to their spatial and energy resolution (figure reproduced from [179]).

Optical spectroscopic techniques such as UV-Vis-NIR spectroscopy and dark field microscopy are based on the measurements of absorption, reflection or scattering of light at the nanoparticles, where, usually, sampling volume is larger than the nanoparticles.

Some efforts have been made to measure plasmonic properties of individual nanoparticles by using UV-Vis spectroscopy where very low concentrations are prepared to ensure that the interparticle spacing is larger than the optical wavelength (no plasmon coupling) or, by depositing well-separated nanoparticles and correlation of their measured spectra with the shape, size and morphology [180]. Dark field microscopy is another commonly used technique that can provide plasmonic properties at a single nanoparticle level (providing that the nanoparticles are well dispersed on the substrate) [181–183]. Although dark field microscopy can reveal the plasmonic properties of individual nanostructures, it does not provide enough spatial resolution to visualize the morphology of the individual nanoparticles and it should be used in combination with a scanning electron microscope (SEM) or transmission electron microscope (TEM). Near-field scanning optical microscopy (NSOM), which provides spatial resolutions beyond the diffraction limit [184], has also been used to characterize plasmonic properties of individual nanoparticles with several nanometer spatial resolutions revealing the distribution of high order plasmon modes [185–187].

1.4.1 Cathodoluminescence (CL) spectroscopy

CL is a electron beam based light emitting technique, where the LSPRs are excited via high energy beam and the radiation scattered into the far field, due to the plasmon excitation, is detected [179, 188–190]. As it measures the plasmon-mediated emission, both the wavelength and polarization state of the scattered photons can be measured [190]. The CL system can be easily adapted to SEM and, therefore, most of the studies on the plasmonic properties of nanostructures are conducted with SEM-CL systems where the resolution is limited by the resolution of the microscope [125, 191–199]. Fig. 1.30 shows two examples of plasmon mapping by SEM-CL, by [191] and [197]. Fig. 1.30A is a SEM micrograph of a lithographically fabricated 725 nm long Au nanowire on a Si substrate. Fig. 1.30B shows CL emission maps of the Au nanowire at different wavelengths of 592 nm, 640 nm and 730 m, which clearly reveal the presence of different plasmon modes [191]. Fig. 1.30C shows the CL spectra obtained from the edge and the tip of an 80 nm thick truncated tetrahedral Au nanoparticle, along with its SEM micrograph and CL emission maps at 530 nm (edge mode) and 604 nm (tip mode). This figure is adapted from [197] where Das et al. conducted a systematical study of the high order surface plasmon modes of such nanoparticles, and could detect ultra-local variations by SEM-CL setup. Vesseur et al. [193] reported that it is possible to resolve whispering gallery modes of a plasmonic subwavelength ring cavities by CL. Lassiter et al. [198] have used CL in order to study the plasmonic properties of highly complex nanoparticle structures that can support both super-radiant bright and sub-radiant dark plasmon modes and reported some "design rules" for Fano resonance presence in such structures.

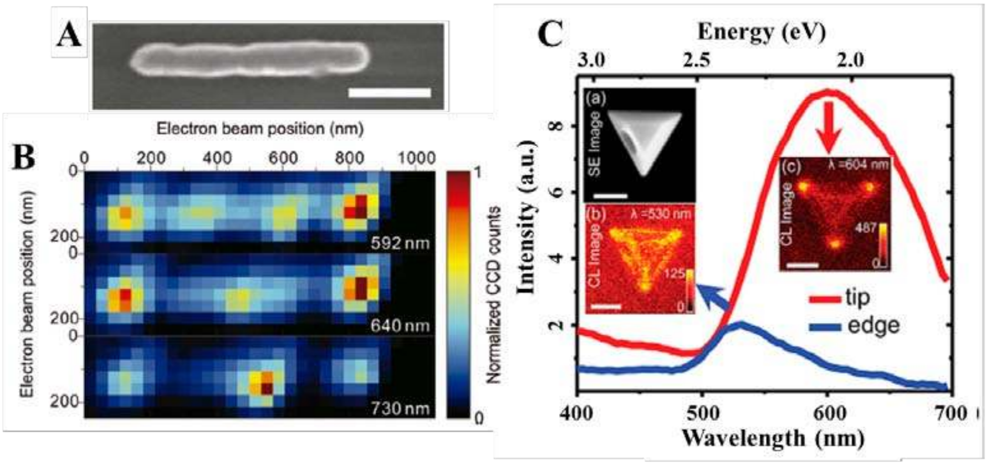

FIGURE 1.30: A. SEM micrograph of a 725 nm long Au nanowire on a Si substrate (scale bar is 250 nm). B. CL images of the Au nanowire at wavelengths of 592 nm, 640 nm and 730 nm, showing different plasmon modes (figure reproduced from [191]). C. CL spectra from the tip and edge of a 80 nm thick truncated tetrahedral (TT) Au nanparticle. Insets show the SEM micrograph and CL emission maps at 530 nm (edge mode) and at 604 nm (tip mode), scale bars are 200 nm (figure reproduced from [197]).

More recently, Atre et al. [199] characterized 3D plasmonic properties of a so-called nanocup (crescent) formed by a polystrene (PS) core and an Au shell (as shown in Fig. 1.31A and B). By tilting this structure over a wide range of tilts (0-165^o and 195-360^o) and obtaining CL spectrum maps at each tilt, they could reveal the angle-resolved distribution of different plasmon modes located at the top and bottom part of the crescent. Construction of CL spectroscopic tomography (Fig. 1.31) based on the individual CL maps at each tilt reveal the distribution of plasmon resonances in 3D [199].

CL implemented to TEM/STEM system is rather less studied yet provides higher spatial resolutions [188, 189, 200–203]. Recently, Losquin et al. [203] reported the plasmonic properties of a 60 nm Au nanoprism measured both using CL and EELS at the nanometer scale with a STEM microscope. Fig. 1.32 shows the EELS (in blue) and CL (in red) spectra obtained from the tip (Fig. 1.32A) and edge (Fig. 1.32B) of the nanoprism. Plasmon maps of the dipolar (Fig. 1.32C) and higher order (Fig. 1.32D) obtained by filtering around the energy of the EELS and CL spectra are also shown in this figure. Although they reveal similar behavior in intensity distribution, their amplitude maps (not shown here, see [203]) revealed that CL only probes the radiative modes, whereas the EELS can also reveal the dark modes [203].

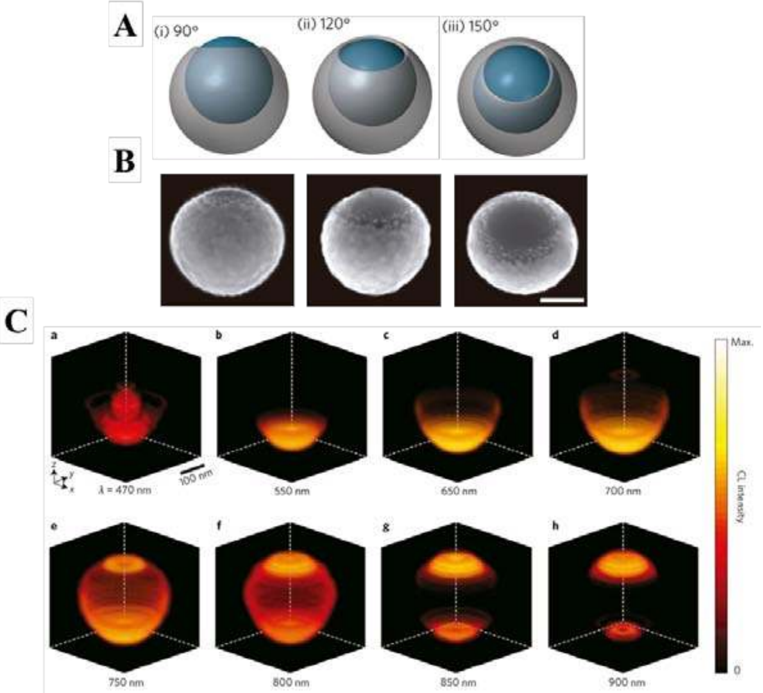
A
(i) 90°
(ii) 120°
(iii) 150°
B
C
a
b
c
d
e
f
g
h
λ = 470 nm
100 nm
550 nm
650 nm
700 nm
750 nm
800 nm
850 nm
900 nm
Max.
CL intensity
0

FIGURE 1.31: A. Schematics of the crescents with orientations of 90^o, 120^o and 150^o where B. shows their corresponding SEM micrographs. Scale bar is 100 nm for all micrographs. C. CL spectroscopic tomography results at different wavelengths from 470 nm to 900 nm, where the intensities are normalized.

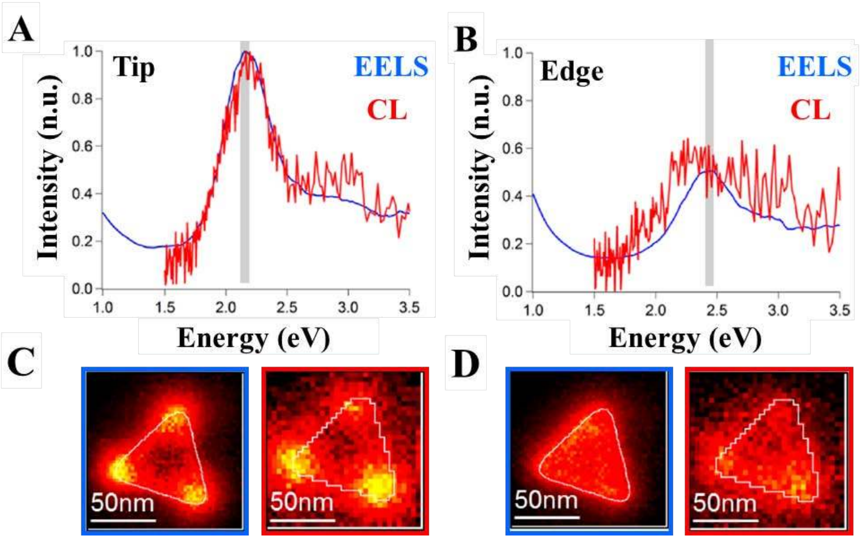

FIGURE 1.32: EELS (blue) and CL (red) spectra obtained from the tip (A) and edge (B) of a 60 nm Au nanoprism with a 30 nm thickness deposited on graphene.

1.4.2 Electron energy-loss spectroscopy (EELS) for plasmonics

Utilization of EELS for characterization of plasmonic properties is not very-well documented in the literature. In this section, we will present some examples of groundbreaking studies conducted over the years.

EELS for plasmonics goes back to the first experimental studies about plasmon resonances. As mentioned above, most of the early studies leading to the discovery of plasmon resonance phenomena observed the energy losses of fast electrons passing through metal films [14, 17–19]. In 2007, Nelayah et al. [204] and Bosman et al. [205] reported, almost simultaneously, first examples of mapping the surface plasmon resonances of individual nanoparticles at the nanometer scale by monochromated EELS in a STEM using spectrum imaging (SI) technique developed by Jeanguillaume and Colliex in 1989 [206].

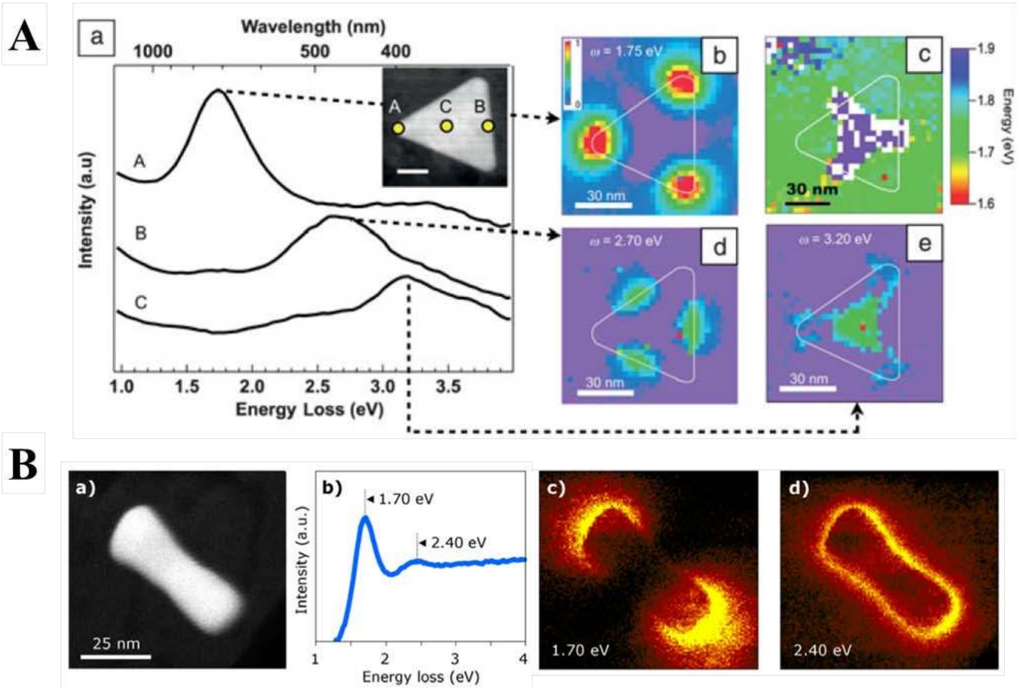

FIGURE 1.33: A. EEL spectra obtained from the tip, edge and center of a 70 nm Ag nanoprism along with their plasmon intensity and energy (only for the tip mode) maps (figure reproduced from [207]). B. STEM micrograph of a Au nanorod, the average spectrum revealing the presence of two plasmon resonances at 1.70 eV and 2.40 eV and the plasmon intensity maps of these modes (figure reproduced from [205]).

Fig. 1.33A shows the EEL spectra and maps obtained by Nelayah et al. [204] (figure reproduced from [207]). In this figure, local EEL spectra obtained from the tip, edge and center of a 70 nm Ag nanoprism are shown in (a), along with their plasmon intensity maps located at 1.75 eV (b), 2.70 eV (d) and 3.20 eV (e). (c) shows the plasmon energy map of the tip plasmon mode located at 1.75 eV. Fig. 1.33B shows the STEM micrograph of a 50 nm Au nanorod where the EELS mapping is obtained. The average

EEL spectra revealed the presence of two different plasmon modes located at 1.70 eV and 2.40 eV. Their plasmon intensity maps revealed that the mode located at 1.70 ev is a dipolar mode confined at the tips of the nanorod and the mode located at 2.40 eV is a surface mode present all around the nanorod.

Thanks to its high spatial resolutions (sub-nanometer scale) and high energy resolution (typically better then 0.2 eV), EELS has been used to map plasmon resonances of different nanostructures including spherical nanoparticles [208–210], nanorod/nanowires [211–215], nanocubes [90, 216, 217], nanodisks [218, 219], nanoprisms [219–221], nanostars [222], and nanodecahedra [223]. EELS has the ability to reveal full modal spectrum including dark plasmon modes, which are unvisible to optical spectroscopy techniques, in coupled nanostructures [208, 211, 215, 218, 221, 224].

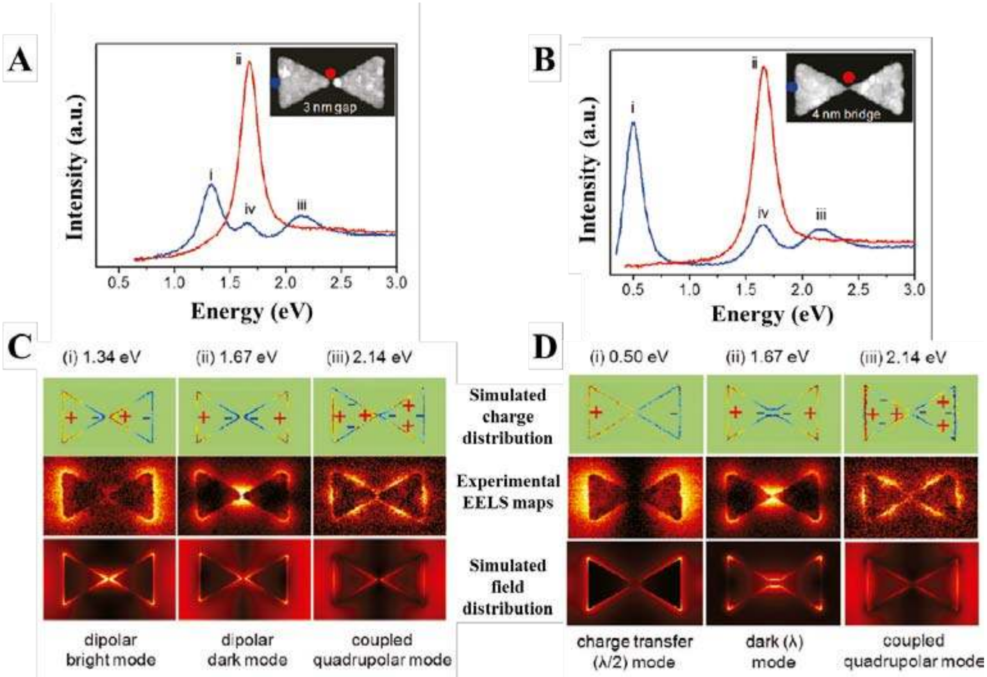

FIGURE 1.34: A. EELS spectra of two ∼80 nm Au nanoprisms separated by a 3 nm gap and B is the EELS spectra of two nanoprisms connected by a 4 nm bridge. C. and D. are simulated charge distributions, experimental EELS maps and simulated field distributions for various plasmon modes observed for separated and connected nanoprisms, respectively (figure adapted from [221]).

Fig. 1.34 shows the experimental EELS results and accompanying simulations for the plasmon resonance mapping of lithographically fabricated ∼80 nm Au nanoprisms on a Si_3N_4 substrate [221]. Fig. 1.34A is the EEL spectra obtained from two nanoprisms separated by a 3 nm gap, revealing the presence of different plasmon resonances at the gap between nanoprisms or at the edge of the nanoprism. Three modes located at 1.34 eV, 1.67 eV and 2.14 eV can be identified. When they have compared the plasmon resonances of individual nanoprisms, it has been found that the corner mode located at 1.62 eV for individual nanoprism splits into two modes with one having a substantial energy shift to 1.34 eV due to coupling [221]. EELS maps of these modes along with the simulated charge distributions and field distributions (Fig. 1.34C) reveal that the mode located at 1.34 eV is a dipolar bright mode, the mode located at 1.67 eV is a dipolar dark mode and the mode located at 2.14 eV is a coupled quadrupolar mode. When the two nanoprisms are not separated but connected each other with a 4 nm bridge, a plasmon peak located at ∼0.5 eV is observed, along with two other modes located at 1.67 eV and 2.14 eV (Fig. 1.34B). Their EELS maps and simulated charge and field distributions presented in Fig. 1.34D reveals that the low energy mode is a charge-transfer ($\lambda/2$) mode, classified on the basis of charge-transfer for the longitudinal modes from antenna theory would correspond to a $\lambda/2$ resonance. The modes located at 1.67 eV and 2.14 eV are identified as dark (λ) and coupled quadrupolar modes, respectively [221].

Charge transfers between two nanostructures can occur when they are touching each other (as in the case presented above) or when they are separated by sub-nanometer gaps as a result of quantum tunneling effect [93, 225]. In recent years, it has been revealed that EELS is capable of observing such quantum effects. For instance, Scholl et al. [106] experimentally observed quantum tunneling between two Ag nanoparticles with a gap of ∼0.5 nm, where they used e-beam induced displacements to control the gap between nanoparticles. More recently, Tan et al. [107] observed quantum tunneling between two adjacent Ag nanocubes, where they could increase the gap up to 1.3 nm for charge transfer via quantum tunneling thanks to bridging by self-assembled monolayers.

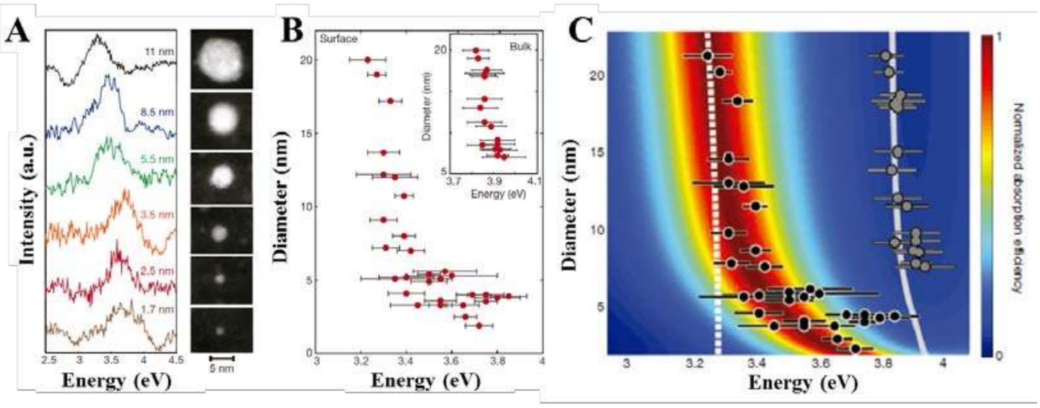

FIGURE 1.35: A. EELS spectra obtained from the spherical Ag nanoparticles ranging from 11 nm to 1.7 nm in diameter (shown in the STEM micrographs). The e-beam was placed onto the edge of nanoparticles in order to excite only the surface plasmons. B. Plot of the surface plasmon resonance energy versus nanoparticle diameter (inset shows the bulk plasmon resonance energies). C. Comparison of the experimentally observed results with the simulated results obtained by DFT-derived quantum permittivity model, where the two results are overlaid. The trend suggested by the classical approach is given in white dotted line. (figure adapted from [209]).

In addition to quantum effects observed between two nanoparticles, Scholl et al. [209] reported the presence of quantum plasmon resonances in individual Ag nanoparticles.

Fig. 1.35A shows the STEM micrographs and EEL spectra obtained from six individual nanoparticles with diameters of (top to bottom) 11 nm, 8.5 nm, 5.5 nm, 3.5 nm, 2.5 nm and 1.7 nm. The EEL spectra are collected with an e-beam placed onto the edge of nanoparticles in order to excite only the surface plasmons. As seen in this figure, the position of the surface plasmon peaks shift to higher energies as the nanoparticle size gets smaller. Moreover, the peak intensities decrease and their width increases with decreasing nanoparticle size. Fig. 1.35B shows the trend of surface plasmon energies with decreasing nanoparticle size. Inset shows the energy of bulk plasmon resonance versus diameter. In contrary to a monotonic trend as suggested by the classical approach, greater variations are observed at the smallest sizes. Such alterations are thought to be due to the fact that nanoparticles are in the quantum regime. In Fig. 1.35C, an overlay of experimental EELS data with the simulation results obtained by density functional theory (DFT)-derived permittivity model is shown, revealing a perfect fit between the experiments and simulations in the quantum regime. The trend suggested by the classical approach is given in white dotted line for the surface plasmon resonances and gray line for the bulk plasmon resonances.

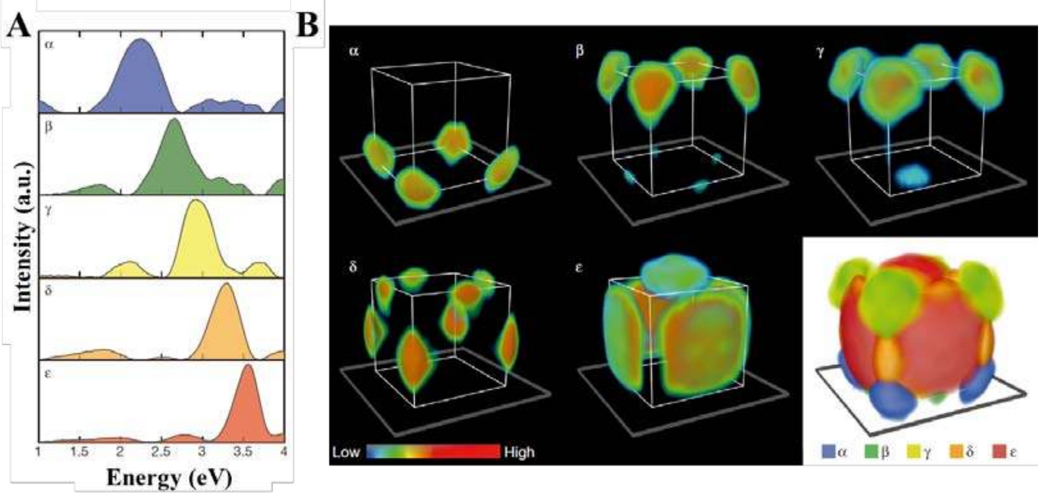

FIGURE 1.36: A. LSPR spectral components $(\alpha, \beta, \gamma, \delta, \epsilon)$ obtained by applying non-negative matrix factorization (NMF) to the EELS datasets at different tilt angles. B. 3D visualization of each spectral components and their overlay (figure adapted from [90]).

As a final example, we present the application of EELS for 3D mapping of plasmon resonances in a Ag nanocube. Nicoletti et al. [90] studied the angle-resolved plasmonic properties of a 100 nm Ag nanocube by using EELS. They have obtained EELS maps at different tilt angles of 0, -15, -30, -45 and -60 degrees and revealed the presence of 5 individual LSPR spectral components (shown as α, β, γ, δ and ϵ in Fig. 1.36A) by applying non-negative matrix factorization (NMF) algorithm to the EELS datasets at diffeent tilt angles. These spectra are used to obtain plasmon maps for each tilt angle and by applying tomographic reconstructures 3D maps shown in Fig. 1.36B are obtained. α, located at ∼2.2 eV is identified as proximal corner mode, where β and γ are two distal corner modes located at ∼2.6 eV and ∼2.9 eV, respectively. δ and ϵ, which located at ∼3.3 eV and ∼3.5 eV, are identified as distal edge and face modes, respectively. It should be noted here that the proximal edge and face modes are located at the same energies with distal corner modes (β and γ), respectively, revealing the above discussed substrate effects unambigously.

With Nicoletti et al. [90] paving the way for the 3D characterization of plasmonic properties by EELS in a Ag nanocube, we have investigated the 3D plasmonic properties of Ag@Au core-shell nanocubes and AuAg nanoframes along with plasmon coupling between two nanostructures, results of which are presented in Chapter 5 of this thesis manuscript.

Chapter 2

Methodology

In this chapter, we will give information about the experimental and simulation methodologies applied throughout this thesis manuscript. While giving the experimental details, we will try to be as definitive as possible.

We will start by giving the experimental details for the synthesis of hollow AuAg nanostructures, which are synthesized via the galvanic replacement reaction at room temperature. Details of the BSA sensing experiments will also be presented in this section.

Then, we will give some basic information about transmission electron microscopy (TEM) and scanning transmission electron microscopy (STEM) techniques, accompanied by a general information about electron-matter interactions. We will then present the basics of electron energy-loss spectroscopy (EELS) technique with an emphasis on the spectrum imaging, low-loss EELS and EELS tomography. Details of the EELS experiments including the microscopes and sample preparation are also given in this section.

Next, the details about the data processing routines applied to EELS datasets in order to determine the plasmonic properties of hollow metal nanostructures will be presented. Namely, we will talk about Gaussian fitting, independent component analysis (ICA) via blind source separation (BSS) and vertex component analysis (VCA) routines.

After giving some information about the simulations conducted by boundary element method (BEM), we will finish this chapter.

2.1 Synthesis of hollow AuAg nanostructures

The hollow AuAg nanostructures used throughout this thesis manuscript were synthesized via sequential galvanic replacement and Kirkendall growth at room temperature, which is reported in Ref. [69]. The possibility of straightforward tuning of the plasmonic properties of metal nanostructures via galvanic replacement has been reported extensively [49, 61, 66, 69, 115, 174, 226, 227]. The galvanic replacement offers a playground of plasmonic nanoparticles across the visible and near infrared regions. However, none of the above mentioned studies investigated the local plasmonic properties of individual nanostructures. In the present thesis manuscript, plasmonic properties of hollow nanostructures are analyzed via EELS at nano-scale. Here, we present the details of the synthesis procedures along with the details of the BSA sensing experiments.

For the synthesis of cuboid AuAg nanostructures presented in Chapter 3 and Chapter 5, Ag nanocubes were used as templates, which were synthesized by a modified polyol method [65, 228]. The straightforward morphological evolution from solid nanocubes to single-walled nanoboxes/nanoframes is due to the increasing extend of galvanic exchange between Ag and Au, whereas the synthesis of double-walled nanoboxes were made possible by slightly modifying the synthesis procedure. To be more precise, in a typical synthesis of single-walled AuAg nanoboxes 0.25 mL of Ag nanocubes ($\sim 10^{12}$ nps/mL) were dispersed in 1 mL of milli-Q water, 1 mL of polyvinylpyrrolidone (PVP, 1 mM by repeating unit), and 0.01 mL of absorbic acid (AA, 0.1 mM) were added. Then, 0.3 mL of $HAuCl_4$ (1mM), was added through a syringe pump at a rate of 25 μL/min under stirring. After the addition of the $HAuCl_4$ solution the reaction was stirred for about 30 min at room temperature. When the UV-vis spectra of the solution became stable, the reaction was stopped. The sample was centrifuged at 8000 g the supernatant was discarded and the pellet was re-suspended in 1 mL of milli-Q water for further characterization. As mentioned, this routine applies for the synthesis of intermediate nanostructures between the nanocubes and nanoboxes such as Ag@Au core-shell nanocubes and pinholed AuAg nanoboxes. The only difference there is the amount of $HAuCl_4$ addition, which was 0.05 mL for the Ag@Au core-shell nanocubes and 0.1 mL for the pinholed AuAg nanoboxes. For the synthesis of double-walled AuAg nanoboxes, we have changed the PVP with cetyl trimethylammonium bromide (CTAB, 1 mL of 0.02 M) and increased the amount of $HAuCl_4$ to 0.5 mL.

The synthesis of AuAg nanotubes presented in Chapter 4 were also done by the galvaninc replacement reaction but this time, Ag nanowires were used as templates. Several micron long, penta-twinned Ag nanowires with diameter about 80 nm were synthesized via a solution-phase approach as reported by Sun et al. [229]. In a typical synthesis of completely hollow AuAg nanotubes, 0.25 mL of Ag nanowires (310 ppm Ag+, 2.9 mM by ICP-MS) were dispersed in 2 mL of milli-Q water, 1 mL of CTAB (14 mM), and 0.1 mL of AA (0.1 mM) were added. Then, 0.5 mL of $HAuCl_4$ (1mM), was added through a syringe pump at a rate of 25 μL/min under stirring. After the addition of the $HAuCl_4$ solution the reaction was stirred for about 30 min at room temperature.When the UV-vis spectra of the solution became stable, the reaction has been stopped. The sample was centrifuged at 5000 g and washed with milli-Q water twice; finally the pellet was re-suspended in 1 mL of milli-Q water for further characterization. For the synthesis of hybrid AuAg nanotubes, the procedure was the same except the amount of $HAuCl_4$ (1mM), which was decreased to 0.25 mL.

Both cuboid AuAg nanostructures and 1D AuAg nanotubes were ultra-sonicated for about 20 min prior to depositing on the Si_3N_4 and/or SiO_2 grids, in order to assure the presence of isolated nanostructures.

We have measured the sensitivity of single-walled AuAg nanoboxes towards conjugation events with BSA and its antibodies. The sensitivity of solid Au nanoparticles were also measured as a reference. Instead of starting a new section presenting the details of these experiments, it is found convenient to show them here, together with the synthesis procedures. In the label free sensing experiments, 900 μL of nanoparticles (10^{12} NPs/mL), spherical Au nanoparticles (Au NP) or single-walled AuAg nanoboxes, dispersed in phosphate buffer 10 mM were mixed with 100 μL of BSA (1mM) in phosphate buffer and placed in an incubator at 37 ^{o}C for 48 hours. After incubation of the nanoparticles, the UV-Vis spectra were acquired. Finally, 20 mL of a 2 mg/mL solution of anti-BSA were added to the incubated nanoparticles and the UV-vis spectra were acquired. It should be noted there that the reason why we have used single-walled AuAg nanoboxes instead of nanoframes or double-walled AuAg nanoboxes was the fact that they can be synthesized with high abundances ($\sim$90%) compared to AuAg nanoframes ($\sim$50%) or double-walled AuAg nanoboxes ($\sim$35%), and we wanted to present a reliable sensing data obtained from such hollow nanostructures. We hope that in the future, by having a better control over the synthesis, we could obtain high abundance of nanoframes and double-walled nanoboxes, which are thought to have better sensitivity properties than those of single-walled nanoboxes, attending to the plasmonic properties shown experimentally and corroborated by simulations.

2.2 Transmission electron microscopy (TEM)

Transmission electron microscope is a versatile tool that can provide information on the materials structural and chemical features. Fig. 2.1 shows a block diagram of a modern day TEM with STEM and energy dispersive X-ray spectroscopy (EDX) and electron energy-loss spectroscopy (EELS) capabilities [230]. Such an equipment allows one to obtain imaging with various techniques such as diffraction contrast imaging, phase contrast imaging (high-resolution imaging) along with the chemical informations by EDX and EELS spectroscopies [230, 231]. In this section, we will present a very basic introduction to the conventional TEM and image formation, an introduction to STEM based imaging and EELS. More details about these techniques can be found in many fundamental books including [230–234].

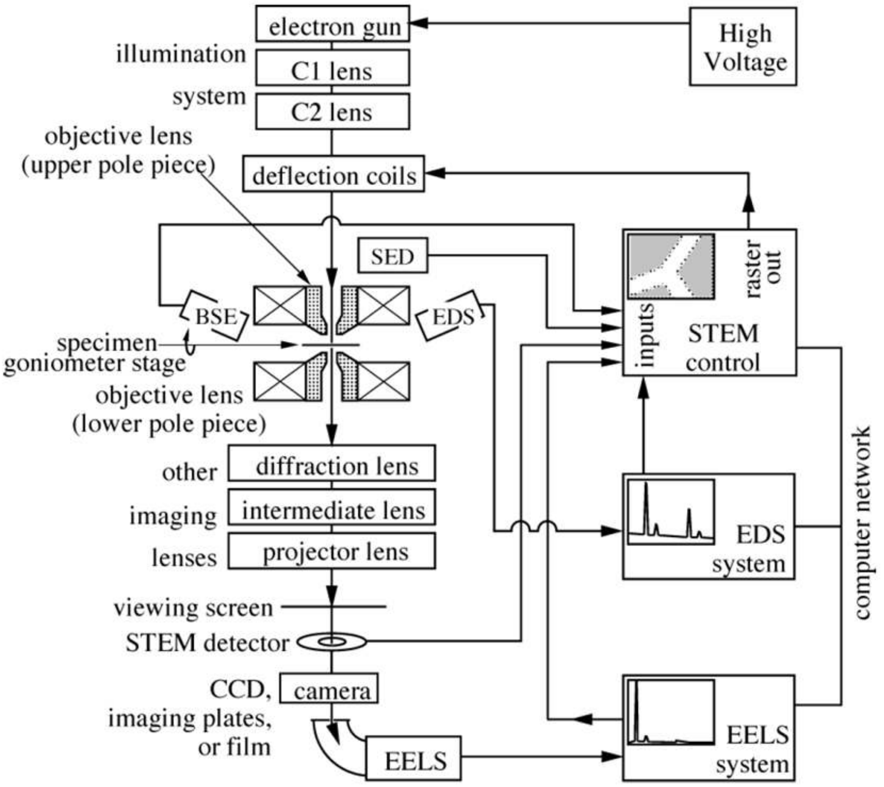
electron gun
High Voltage
illumination system
C1 lens
C2 lens
objective lens (upper pole piece)
deflection coils
SED
raster out
BSE
EDS
inputs
STEM control
specimen
goniometer stage
objective lens (lower pole piece)
other imaging lenses
diffraction lens
intermediate lens
projector lens
EDS system
computer network
viewing screen
STEM detector
CCD, imaging plates, or film
camera
EELS
EELS system

FIGURE 2.1: A block diagram of a modern day TEM with STEM and spectroscopy capabilities (figure reproduced from [230]).

Components of a typical TEM such as the electron source, condenser, objective and imaging lenses and various detectors are shown in Fig. 2.1. In the following, we will talk about the interaction of electrons with the specimen resulting in the formation of different signals, basic principles of TEM and STEM modes as well as the EELS, EELS spectrum imaging and EELS tomography.

2.2.1 Electron-matter interactions

When high energy electron beam hits a thin specimen, a wide range of signals are generated due to the interaction of the e-beam with the sample. Electrons are considered as ionizing radiation due to the fact that they are capable of removing the tightly-bond inner-shell electrons from the attractive field of the nucleus [231]. A schematic of this interaction and resulting secondary signals are shown in Fig. 2.2A. In this figure, we have indicated the techniques used in this thesis manuscript along with the related signals. Each one of these signals have been used in different microscopy techniques. For instance, Auger electrons are used in a surface analysis technique called Auger electron microscopy, whereas the back-scattered electrons (BSE) and secondary electrons (SE) are typical signals used in scanning electron microscopes (SEM). Here, we are interested in the signals exploited by the TEM related techniques. The generated visible (and UV) lights are used for cathodoluminescence (CL) technique, although it can be coupled with TEM, we are not going to talk about the CL in this chapter. Its application for the characterization of plasmonic properties at the nanoscale is presented in the previous chapter (see Section 1.4.1).

Characteristic X-rays generated from the upper part of the sample carry information about the atoms when collected by an energy dispersive X-ray spectroscopy (EDX) detector. They provide information about the chemical composition of the sample. We will use the EDX technique in order to determine the chemical composition of the hollow AuAg nanostructures throughout thesis thesis manuscript.

Electrons passing through the sample undergo *scattering*, which can be either *elastic* or *inelastic*. In elastic scattering, electrons do not lose their energy, whereas they experience some energy losses during the inelastic scattering. Both elastically and inelastically scattered electrons can be *coherent* (mainly *Bragg* scattering) or *incoherent* (mainly *Rutherford* scattering) according to their wave nature. Coherently scattered electrons are those that are in phase with one another (and of a fixed wavelength) and incoherently scattered electrons have no phase relationship after interacting with the specimen [231]. Basic TEM modes of imaging and diffraction, as well as the bright field STEM, are based on the coherent elastically scattered electrons, which are scattered nearly parallel to the incident beam. At high angles, typically larger than 10^o, elastically scattered electrons become more incoherent. The incoherent elastically scattered electrons are used in high angle annular dark field (HAADF) imaging, a technique where the intensity measured is barely proportional to the square of the atomic number (Z^2) and the specimen thickness [233]. As mentioned above, inelastically scattered electrons are the electrons that lose part of their energy due to the interaction with the sample. These

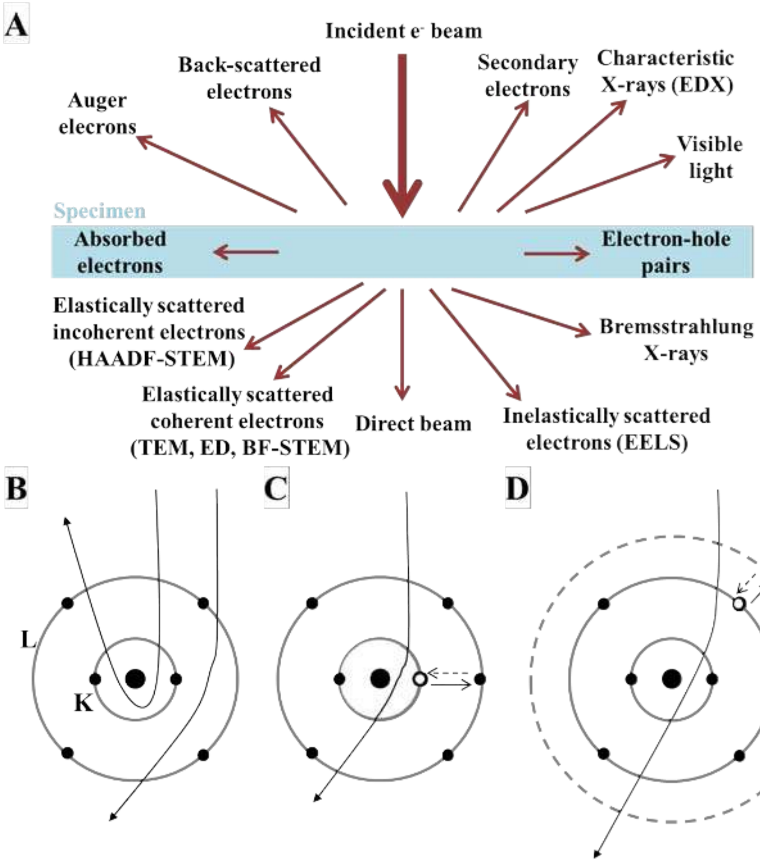
A
Incident e⁻ beam
Back-scattered electrons
Auger elecrons
Secondary electrons
Characteristic X-rays (EDX)
Visible light
Specimen
Absorbed electrons
Electron-hole pairs
Elastically scattered incoherent electrons (HAADF-STEM)
Bremsstrahlung X-rays
Elastically scattered coherent electrons (TEM, ED, BF-STEM)
Direct beam
Inelastically scattered electrons (EELS)
B
C
D
L
K

FIGURE 2.2: A. Different type of signals generated when an indicent beam interacts with a thin specimen. The techniques used in this thesis manuscript are written in parenthesis after the related signal. In the lower row, a classical view of electron scattering by a single carbon atom is shown. B. Elastic scattering. C and D are inelastic scattering by inner- and outer-shell electrons, respectively.

electrons are collected and their energy-distribution is measured with an electron energy-loss spectrometer (EELS) [234]. They carry valuable information about the chemistry and bonding states of the specimen due to the fact that the extend of energy-loss is specific for each interaction as well as the interactions with different materials/elements. During this thesis manuscript, we will exploit this technique in the so-called *low-loss* region (the regions extends up to 50 eV, whereas we are focused on the energy range between zero-loss peak and 4 eV), which provides information about the excitation of outer-shell electrons including plasmon resonances.

In Fig. 2.2, a classical (particle) scheme of electron scattering by single atom (in this case carbon) is also presented (lower row). Elastic scattering is caused by Coulomb interaction (attraction) with atomic nuclei (Fig. 2.2B), where each nucleus contains a high concentration of charge causing an intense electric field in the close surrounding. When an incident electron approaches close enough to the nucleus, it is deflected with a large angle, which is known as Rutherford scattering [234]. On the other hand, inelastic scattering occurs as a result of Coulomb interaction (repulsion) between the incident electron and the atomic electrons that surround the nucleus. It can be due to the scattering by inner-shell electrons as shown in Fig. 2.2C or outer-shell electrons as shown in Fig. 2.2D.

2.2.2 Basic principles of conventional TEM

Fig. 2.3A is a ray diagram showing the paths of image formation in a conventional TEM [230]. In this scheme, it is assumed that all the electrons travel straight forward (parallel to the optical axis) before interacting with the specimen. The image is formed at the viewing screen by combination of all transmitted and all diffracted rays leaving the specimen. Having said that, we note that not all the rays in the back focal are required to form an image, where different type of images can be formed with only rays passing through the same point in the back focal plane. One can control the rays by placing an objective aperture along the back focal plane at a specific location to form an image with different modes or a diffraction pattern. Fig. 2.3B shows the formation of a bright field (BF) image by positioning the aperture letting only the transmitted (un-diffracted) electrons to pass. Dark field (DF) images are formed by using diffracted electrons, in particular one can choose different diffraction spots to create the image solely formed by those electrons diffracted for that specific diffraction plane. It is done by placing the objective aperture on a diffracted beam (Fig. 2.3C). In addition to these image modes, it is possible to obtained diffraction patterns using a conventional TEM. Fig. 2.3D shows the ray diagram in the so-called *selected area diffraction (SAD)* mode, where a second aperture (selected area aperture) placed along the image plane to limit diffraction pattern formation by the diffracted beams from the selected region of interest.

After presenting different modes of conventional TEM, it is convenient to shortly mention about high resolution TEM (HRTEM, usually referred as phase contrast imaging), as it is used in several occasions during this thesis manuscript. Contrast in the TEM images can originate due to the differences in the phase of the electron waves scattered from the specimen. Although there are many different parameters affecting the contrast such as orientation, thickness, scattering factor etc. (see, for instance, chapter 23 in [231] for more details), the phase contrast can be exploited to image the atomic structure of the materials. Providing that the microscope has enough resolution power to image the atomic structure, a large objective aperture, which lets the usage of as many as possible beams for the image formation, has to be selected for high resolution imaging. Phase contrast will occur whenever more than one beam contributes to the image formation. A typical HRTEM contains information about the atomic orientation and spacing through the lattice fringes. However, it should be noted here that the fringes are not direct

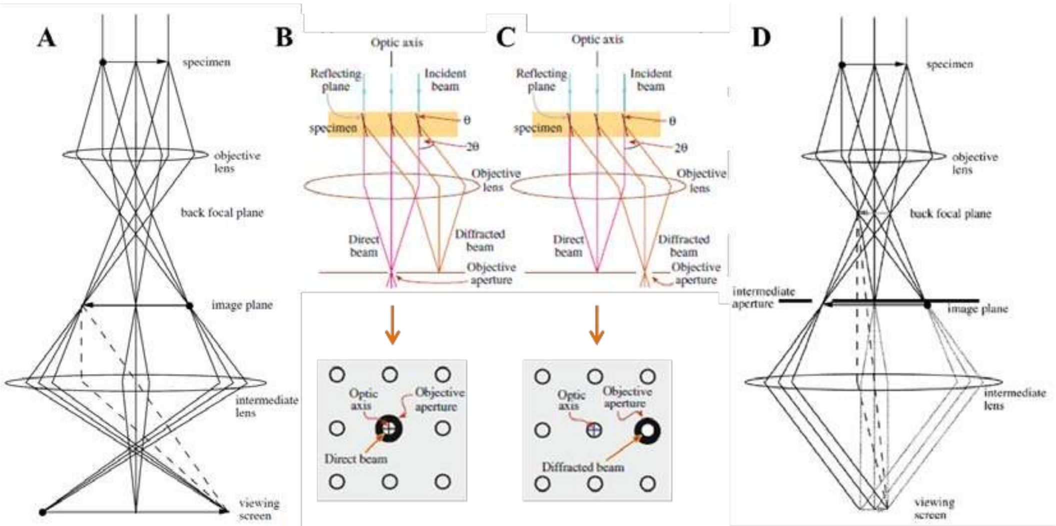
A
specimen
objective lens
back focal plane
image plane
intermediate lens
viewing screen
B
Optic axis
Reflecting plane
Incident beam
specimen
θ
2θ
Objective lens
Direct beam
Diffracted beam
Objective aperture
Optic axis
Objective aperture
Direct beam
C
Optic axis
Reflecting plane
Incident beam
specimen
θ
2θ
Objective lens
Direct beam
Diffracted beam
Objective aperture
Optic axis
Objective aperture
Diffracted beam
D
specimen
objective lens
back focal plane
intermediate aperture
image plane
intermediate lens
viewing screen

FIGURE 2.3: A. Ray paths in image mode (figure reproduced from [230]). Ray diagrams showing the use of objective aperture to produce bright field (B) and dark field (C) images along with the schematics of diaphgrams on the viewing screen (figures reproduced from [231]). D. Ray paths in selected area diffraction mode (figure reproduced from [230]).

images of the structure. Issues like overlapping of two crystals, which always do not create distinctive Moiré fringes, need to be considered. A nice example of possible misled of assuming the fringes as atomic planes, as they look like so, is obtained during the HRTEM studies of this thesis manuscript. Fig. 2.4A shows HRTEM image taken from an AuAg nanotube (see Chapter 4) revealing nicely oriented fringes with some dislocations and contrast differences along the image. Fig. 2.4B shows the detail of red squared region in Fig. 2.4A and suggests the presence of a defect-free mono-crystalline structure. In fact, this HRTEM image is formed by overlapping of two different crystals in the penta-twinned nanotube. Power spectrum (fast Fourier transform) shown in Fig. 2.4 reveals that the spacing between these lattices do not correspond to the face centered cubic lattice of AuAg alloys, yet somehow looks like a diffraction pattern obtained from a mono-crystalline material. The proof that it is generated by two different crystals is only visible by some diffraction spots with d-spacing of ∼1.23 Å (indicated by green circles) being separated from one another. Each of these diffraction spots belongs to the {311} planes of two different crystals having the face centered cubic AuAg phase.

2.2.3 Basic principles of STEM

We continue with the basic principles of a STEM. In most of the microscopes (of common brands like JEOL and FEI) STEM is an operation mode in the same microscope that can function as a TEM as well (as shown in 2.1) and there are some microscopes

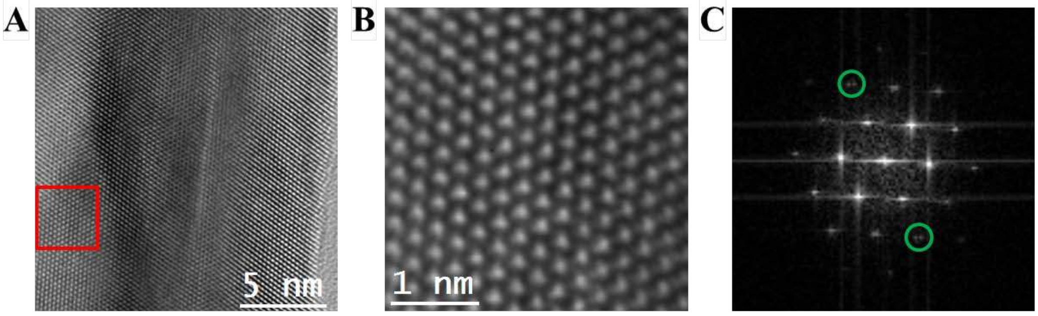

FIGURE 2.4: A. HRTEM image obtained from a AuAg nanotube. B. Detail of the red squared region and C. its corresponding power spectra.

that function only as a STEM (referred as ”dedicated” STEM, for instance Nion microscopes). Fig. 2.5A shows the schematic representation of a STEM showing different lenses and detectors. Notice the presence of scan coils, which was not the case for the TEM (compare with Fig. 2.3). In STEM, a focused electron beam (also called as probe) rastered through the sample with a fixed beam direction. The necessity of having a fixed optical axis requires the presence of scan coils, which tune the axis of the probe without tilting the optic axis [235]. As mentioned above, elastically scattered coherent electrons are used in bright field (BF)-STEM imaging, and the incoherent electrons, with high scattering angles, are used in dark field (DF)-STEM imaging.

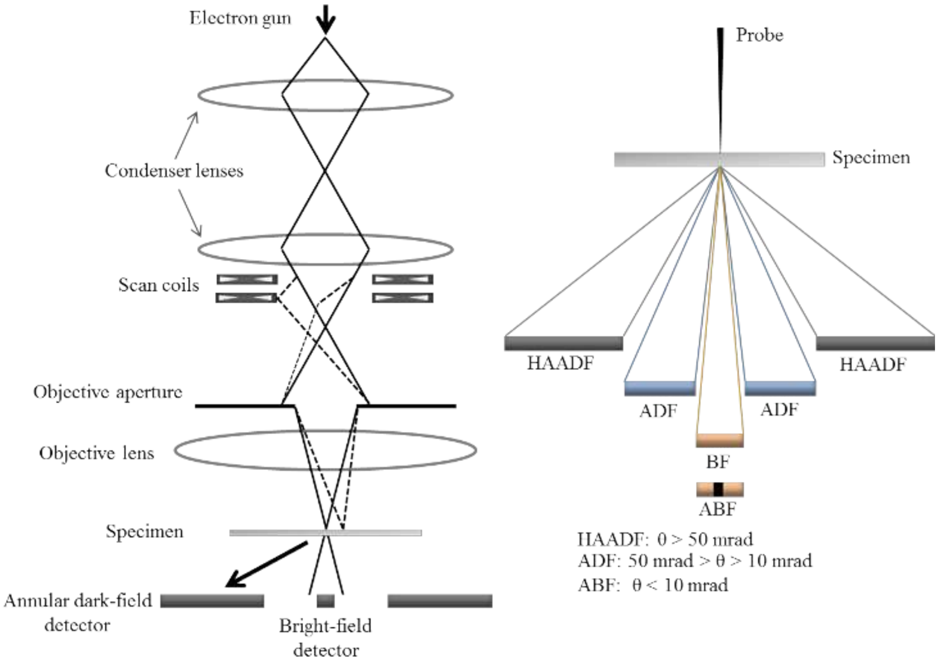
Electron gun
Condenser lenses
Scan coils
Objective aperture
Objective lens
Specimen
Annular dark-field detector
Bright-field detector
Probe
Specimen
HAADF
HAADF
ADF
ADF
BF
ABF
HAADF: θ > 50 mrad
ADF: 50 mrad > θ > 10 mrad
ABF: θ < 10 mrad

FIGURE 2.5: A. A schematic representation of a STEM, showing the basic elements and B. schematics of different STEM detectors based on the scattering angle.

In STEM, there are different detectors that collects the electrons scattered at different angles as shown in Fig. 2.5B. The detectors shown in this figure are namely, high angle annular dark field (HAADF), annular dark field (ADF), annular bright field (ABF) and bright field (BF) detectors. Notice the term of "annular" for all detectors except the BF, which is due to the fact that these STEM detectors consist of an annular sensitive region that detects the electrons scattered with different angles [236]. Related angles are also shown in Fig. 2.5B. The HAADF detector collects the electrons scattered with angles larger than 50 mrad. The intensity of the HAADF images are approximately proportional to the square of the atomic number (Z^2), thus, the heavier atoms will be brighter. For this reason, this method is also known as *Z-contrast* imaging after Crewe [237]. It is by far the most popular STEM imaging mode [233]. It is suggested that high scattering angles (∼100 mrad) would enhance the compositional contrast [238]. Moreover, when such high scattering angles are used, the coherent effects of elastic scattering could be neglected as the scattering in these conditions is almost entirely thermally diffuse [239]. During this thesis manuscript, we will take advantage of the HAADF-STEM technique coupled with EELS and EDX.

The ADF detector collects the electrons scattered with angles between 10 mrad and 50 mrad. This range of scattering can also be separated to two different ranges as low angle ADF (typically between 10 mrad and 25 mrad) and medium angle ADF (typically between 25 mrad and 50 mrad). In this regime, the contrast of the images is mostly due to the diffraction contrast [235]. As mentioned above, BF detector collects the elastically scattered coherent electron with scattering angles lower than 10 mrad. ABF detectors, which are formed by blocking the center of the BF detector, also collect the electrons scattered at low angles. With its annular design, the contrast of light elements is significantly increased, thus, it has been reported to be quite efficient in imaging of light elements. Even the visualization of H atomic columns is reported thanks to the ABF-STEM technique [240], where N and O atoms can be easily imaged [241].

2.2.4 Electron energy-loss spectroscopy

As mentioned above, electron energy-loss spectroscopy (EELS) in a S/TEM involves the analyses of the energy-distribution of inelastically scattered electrons [234]. A schematic diagram showing the collection of energy-loss spectrum by an image filter mounted to a S/TEM column is shown in Fig. 2.6 [231]. There is only one commercially available spectrometer produced by Gatan, Inc. referred as parallel-collection EELS or PEELS.

It is shown that inelastic scattering of electrons occurs due to the Coulomb interactions between the incident beam and the inner- or outer-shell electrons. The ground-state energies of inner-shell electrons are typically some hundreds or thousands of electron volts below the Fermi level of the solid. When the incident beam interacts with the

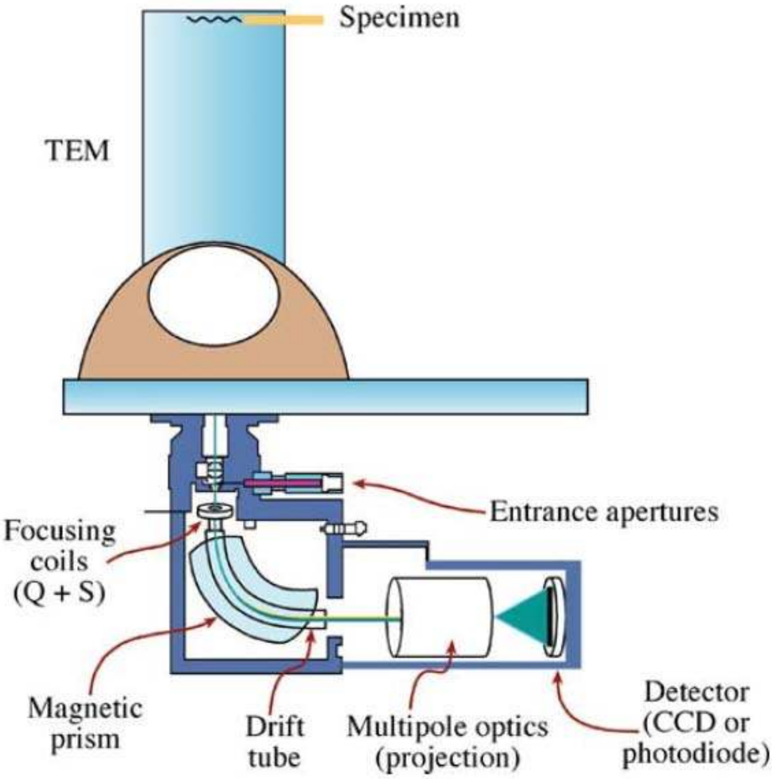

FIGURE 2.6: Schematic diagram of a parallel collection of the energy-loss spectrum, so-called parallel EELS (PEELS)system (figure reproduced from [231]).

inner-shell electrons, note that the unoccupied electron states (as shown in Fig. 2.2C) can only exist above the Fermi level [234], the inner-shell electrons can only be excited when they absorb an amount of energy greater than their binding energy. As the total amount of energy must be conserved for each collision, the incident beam loses an equal amount of energy, which, thereby, can be detected by EELS. Single-electron excitations are also possible for the case of inelastic scattering by outer-shell electrons (as shown in Fig. 2.2D). Due to such scattering, in an insulator or a semiconductor material, a valence electron makes an interband transition across the energy gap, or a conduction electron of the metal makes a transition to a higher state (possibly within the same energy band). Main interest of this thesis manuscript lies in another type of excitation where, as an alternative to the single-electron mode of excitation, outer-shell inelastic scattering involves many atoms of the metal. This collective scattering is the plasmon resonance and its theory and applications are given in detail in Chapter 1.

After this introduction about inelastically scattered electrons, we contiune with the EELS. In Fig. 2.7, a typical EELS obtained from C is presented, where the intensity is in logarithmic scale. It is composed of three main parts, namely zero-loss peak (ZLP), low-loss region and core-loss regions, which are indicated with red, green and blue bars,

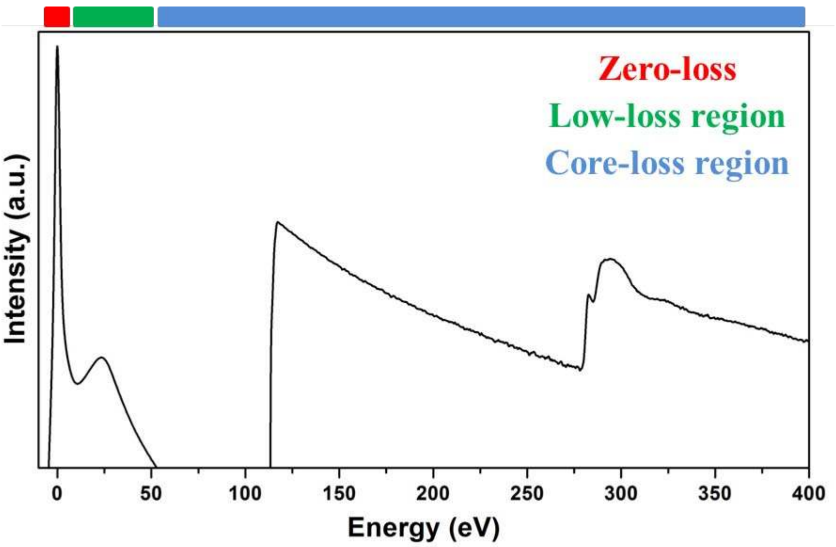

FIGURE 2.7: A typical EELS obtained from C (intensity is in logarithmic scale). Three different regions of zero-loss peak (red), low-loss region (green) and core-loss region (blue) are indicated with colored bars above the spectrum.

respectively. ZLP is formed by collection of all electrons that have suffered inconsequential inelastical scattering. Thus, it contains no measurable spectroscopic information. Its practical significance for low-loss EELS measurements like plasmon mapping mostly arise from the fact that it has a tail shadowing the lowest energy-loss region with its high intensity. This region, unfortunately, corresponds to the near-infrared (NIR)/visible range of the optical spectrum and contains valuable information [242]. Although it does not contain any information, it is useful. For instance, the ZLP is commonly used to determine the thickness of the sample. The most common procedure for thickness determination is so-called t/λ ratio, where t is the sample thickness and λ is the total mean free path for all inelastic scattering. It is calculated by the ratio between the area under the ZLP (I_o) with the total integrated area (I_t) [234]. It is also used as a reference point to align the energy of different spectra, which is crucial for spectrum imaging (SI) [206]. Let us shortly mention about the other regions of the EELS spectrum before presenting details of the SI technique.

The energy region between the ZLP and 50 eV is typically considered as low-loss region, which contains mostly the information related to the interactions with the outer-shell electrons. This region has a definitive link with the optical properties of materials. Having said that, also remember that the optical properties depend on the dielectric properties (see Section 1.1), some electronic properties of the materials can be obtained by low-loss EELS [242]. All the information presented in this thesis manuscript on the plasmonic properties of hollow metal nanostructures are extracted from the low-loss region of the EELS spectrum.

The core-loss region spans typically beyond the 100 eV and provides information on chemistry of the materials by elemental analysis, quantification and on the electronic structure by bonding and valence state analyses. As we are not interested in this region in the present thesis manuscript, we will not discuss its details here (see Ref. [234]).

2.2.4.1 Spectrum imaging: Data cube

Spectrum imaging (SI) refers to an EELS acquisition technique developed by Jeanguillaume and Colliex in 1989 [206] and experimentally applied for the first time by Hunt and Williams in 1991 [243]. During EELS, we obtain a typical spectrum, as the one presented in 2.7, which shows the variation of intensity (counts) as a function of energy loss (eV). Such a spectrum does not give any information about the spatial coordinates that it has been obtained. Schematic representation of different EELS acquisition techniques are presented in Fig. 2.8. The above presented EELS spectrum correspond to Fig. 2.8A, where only the energy axis is present. Similarly, we can obtain a spectrum line as we raster the e-beam over a line and collect the EELS spectrum from each pixel over one axis (Fig. 2.8B). If we collect EELS spectrum over an area of interest, we obtain a data cube (Fig. 2.8C) consisting of two spatial axes (x and y) and an energy axis [206]. This data cube is also known as spectrum image (SI). Over the last decade, it has become a common practice during EELS analyses and used for obtaining variety of information from different materials (see [242] for an overview of the technique and its applications). We will also take advantage of the spectrum imaging technique in order to spatially mapping the plasmon resonances shown in this thesis manuscript.

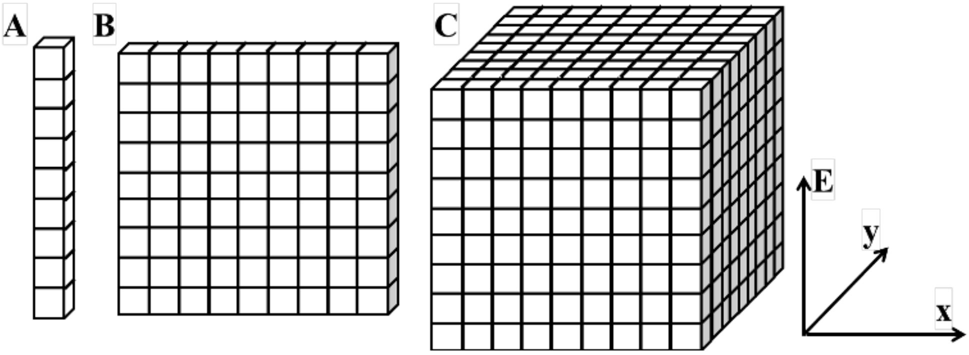

FIGURE 2.8: Schematic representations of different EELS acquisition techniques: A. single spectrum, B. spectrum line and C. spectrum image, along with the corresponding cartesian axes of energy (E), x and y.

During the recent years, the term of spectrum voxel (pr spectrum volume) has been introduced in order to refer the three-dimensional SI EELS analyses, where, after applying tomography reconstructions to the individual SIs obtained at each tilt angle, the dataset is formed by four-dimensional information (x, y, z and E) [244–247].

2.2.4.2 The need for high energy resolution

The energy resolution of the EELS is defined as the full-width-at-half-maximum (FWHM) of the ZLP. As mentioned above, the tail of the ZLP spans over the low-loss region covering many useful information about the optical properties of the materials. As the ZLP gets narrower, thereby the energy resolution increases, one can get the most out of the EELS data, not only for the mentioned low-loss region used for plasmon mapping [204, 205, 248], bandgap measurements [249] and valence determination [250] but also for the accurate determination of the fine structures obtained by core-loss EELS [251–253].

The energy resolution of the spectrometer is defined by the electron source. For instance, at ∼100 keV a W source has an energy resolution of ∼3 eV, which is ∼1.5 eV for a LaB_6 source, ∼0.7 eV for a Schottky field emitter and ∼0.3 eV for a cold field emission gun (FEG) [231]. As the accelerating voltage gets higher than 100 keV, these values get slightly worse due to the increased electrostatic electron-electron interactions at the electron source crossover, which is known as Boersch effect [231, 234]. One needs to improve the energy resolution of the electron source, thereby the resolution of the spectrometer, in order to study the low-loss region. For instance, in this thesis manuscript, we present plasmon resonances located at energies lower than 0.5 eV observed during the plasmon mapping on AuAg nanotubes (see Chapter 4). Such an observation would be impossible with the above mentioned energy resolutions. The most common way of increasing the energy resolutions is done by using a monochromator [231, 234, 253]. Basically, a monochromator is a system fitted to the microscope column that allows to narrow the energy spread down by using slits, which results in significant improvements in the energy resolution. About ∼0.7 eV energy resolution of the Schottky field emitter can be filtered to resolutions better than 0.1 eV [254]. Almost all of the studies mentioned in Section 1.4.2 used monochromated EELS for plasmon mapping, which is also used in the present thesis manuscript.

As an alternative to the monochromators, several mathematical algorithms are developed in order to increase the energy resolution [234]. In particular, by applying an algorithm known as *Richardon-Lucy*, which is based on the deconvolution of the obtained EELS spectra, typical energy resolutions of ∼1 eV could be enhanced down to 0.2-0.3 eV [255]. It has been extensively used by the ”Orsay STEM Group” in order to improve the ∼0.45 eV energy resolution obtained by using a cold FEG VG microscope during the characteriation of plasmonic properties (for instance, see [204] and [216]). Moreover, there have been several studies applied Richardson-Lucy algorithm to the data obtained by monochromated EELS to further increase the energy resolution [256, 257], where Bellido et al. [257] reported the possibility of obtaining 10 meV energy resolutions after deconvolution of ∼75 meV raw EELS data obtained with a monochromated STEM-EELS.

With their ∼0.3 eV resolutions, microscopes with cold FEG sources (like VG and Nion microscopes and new-generation JEOLs) provide the best energy resolution among non-monochromated microscopes. Krivanek et al. [258] designed an all magnetic monochromator/spectrometer system for their cold FEG Nion dedicated STEM setup with a prediction that it would provide 10 meV energy resolutions at sub-angstrom spatial resolutions. About five years after its design, it has been experimentally shown that such a system can, in fact, provide 9 meV energy resolutions and can be used to study vibrational excitations with energies as low as 106 meV (for SiC) [259].

2.2.4.3 EELS tomography

Electron tomography is a technique used to produce 3D information by acquiring images at different tilt angles and merging them together for so-called tomographic reconstruction [260–262]. Fig. 2.9 shows the schematic diagram of tomographic reconstruction using the back-projection method, where a series of images are acquired at successive tilt angles and then back-projected into a 3D object space resulting in the 3D reconstruction [260].

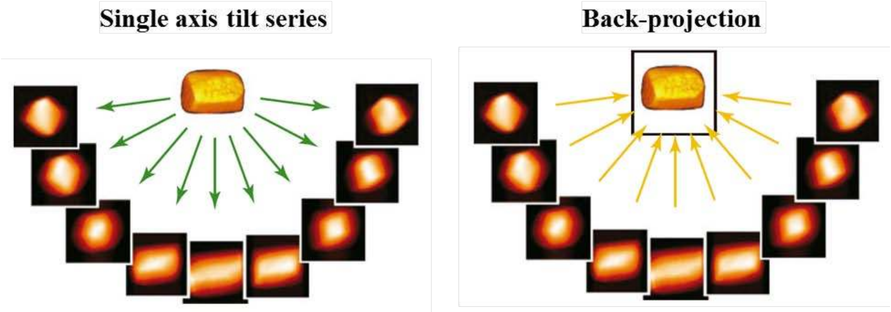

Figure 2.9: Schematic representation of electron tomography: A tilt series of a 3D object are acquired and then back-projected to obtain 3D volume (figure reproduced from [260]).

Electron tomography can provide chemical information in 3D when coupled with the EDX, EELS or EFTEM techniques [263–265]. In fact, there have been several studies showing the power of STEM-EELS technique for 3D characterization of different materials [90, 244–247, 265, 266], most of which have dealt with the core-loss signals. 3D plasmon-field tomography has been shown theoretically by Hörl et al. [267]. More recently, as also mentioned in the Section 1.4.2 (see Fig. 1.36), Nicoletti et al. [90] reported the first 3D EELS mapping of localized surface plasmon resonances of a 100 nm Ag nanocube. In Chapter 5 of this thesis manuscript, we present 3D plasmonic properties of hollow AuAg nanostructures as well as the plasmon coupling between two nanostructures in 3D.

2.2.5 Experimental details

Throughout this thesis manuscript, we present plasmonic properties of various AuAg hollow nanostructures obtained by EELS in monochromated STEMs. Here we present the details of these EELS experiments.

In Chapter 3, we present the plasmonic properties of cuboid AuAg nanostructures of an Ag nanocube, an Ag@Au core-shell nanocube, a pinholed AuAg nanobox, a single-walled AuAg nanobox, an AuAg nanoframe and a double-walled AuAg nanobox. These EELS analyses were performed by using a Cs probe-corrected FEI^{TM} Titan 60-300 STEM equipment operated at 80 kV. This microscope is located at the Advanced Microscopy Laboratory (LMA) in Institute of Nanoscience of Aragon (INA). It is equipped with a high-brightness X-FEG gun, a Wien filter monochromator and a Gatan^{TM} Tridiem 866 ERS energy filter with a collection angle of 32 mrad and a dispersion of 0.01 eV per channel.

We have deposited the AuAg nanostructures on 15 nm thick Si_3N_4 grids obtained from Ted Pella^{TM}. These grids have 9 0.1 mm x 0.1 mm windows.We have applied a hydrogen plasma cleaning by using a Plasma Etch^{TM} plasma cleaner, at room temperature with an H_2 flow of 1000 mT and applied power of 100 W, prior to EELS analyses in order to eliminate the presence of organic residues from the synthesis procedure. We have used hydrogen plasma due to the fact that Ag-rich nanostructures get easily oxidized during the typical Ar-O_2 plasma cleaning. The plasma cleaning time was typically around 20 minutes but it varied from sample to sample. It should be noted here that the Si_3N_4 grids can resist up to 1 hour of hydrogen plasma cleaning in given conditions.

We have obtained by EELS maps by using the spectrum imaging technique with spatial resolutions (pixel size) of about 1.6 nm. Typical energy resolutions of these EELS maps were about 130 meV. The details of data processing are presented in the next section. About 20 to 40 EELS spectra were obtained from each pixel with an exposure time $\sim$30 ms. Moreover, the HRTEM micrograph presented in this chapter was obtained by using a JEOL^{TM} 2010F FEG TEM operated at 200 kV. This microscope is located at the Scientific and Technological Centers (CCiT) of Universitat de Barcelona.

In Chapter 4, plasmonic properties of AuAg nanotubes are presented. These EELS analyses were also performed by using the FEI^{TM} Titan microscope at LMA with the same experimental conditions as the above presented details for the analyses of cuboid

AuAg nanostructures. Sample preparation routines were also the same as presented above. The spatial resolution of the EELS-SI obtained from AuAg nanotubes was about 5 nm as they are quite big in size, which is the only difference between the EELS analyses on the nanocubes/nanoboxes and nanotubes. HRTEM micrographs presented in this chapter were obtained by using an image-corrected FEI^{TM} Titan^3 microscope operated at 300 kV. This microscope is located at LMA-INA. Moveover, the STEM-EDX maps presented in this chapter were obtained by using a FEG FEI^{TM} Tecnai F20 microscope operated at 200 kV, which is located at the Institut Català de Nanociència i Nanotecnologia (ICN2).

In Chapter 5, we present the 3D plasmonic properties of different AuAg nanostructures of an Ag@Au core-shell nanocube, a partially hollow AgAu nanocube, an AuAg nanoframe, two Ag@Au core-shell nanocubes separated by ∼22 nm gap and an Ag@Au core-shell nanocube and an AuAg nanoframe separated by ∼14 nm gap. These samples are essentially similar to the ones presented in Chapter 2. The EELS analyes presented in this chapter were obtained by using the FEI^{TM} Titan^3 50-300 "PICO" microscope operated at 80 kV. This microscope is located at the Ernst Ruska-Centre (ER-C) for Microscopy and Spectroscopy with Electron at Jülich Research Centre, Germany. It is a specially designed microscope referred as the PICO and it is equipped with a high-brightness X-FEG electron gun, a monochromator unit, a Cs probe corrector, a Cs-Cc achro-aplanat image corrector and a post-column energy filter (Gatan Quantum ERS image filter) system. The EELS maps obtained by using this microscope had typical energy resolutions of 120 meV, where the spatial resolution varied between 1.2 nm and 2.0 nm depending on the spectrum imaging area. We have obtained EELS maps between tilt angles of $\pm 60_o$ (which may differ slightly from sample to sample). Since the Si_3N_4 grids have small isolated windows, they did not allow us to obtain tilt series at these high angles. Instead, we have used 18 nm thick SiO_2 grids with a single 0.5 mm x 0.5 mm window area, obtained from Ted Pella^{TM}. The rest of the sample preparation was the same as above. Due to high number of tilt series and, more importantly, e-beam induced morphological changes, we had to reduce the acquisition times to about 5 min per EELS maps. We have obtained about 3 EELS spectra at each pixel. Moreover, atomic resolution STEM micrographs and STEM-EDX analyses presented in this chapter were obtained by using a Cs probe-corrected FEI^{TM} Titan GE 80-200 microscope operated at 200 kV, which is equipped with a high brightness X-FEG, a Super-X EDX system with four detectors and a Gatan Enfinium ER DUAL EELS spectrometer. This microscope is also located at ER-C.

2.3 Processing of EELS data

A typical EELS spectrum is formed by contributions from various types of inelastic scattering, and it is often necessary to separate these components for further studies. For most of the core-loss EELS experiments, providing that there is no overlap of peaks from different materials, spectral components can be obtained by just separating them from the contributions of the background. This can be done quite efficiently by using different algorithms including the ones presented in the following. However, for the low-loss EELS studies like the ones presented in this thesis manuscript, an extreme care must be given to the separation of the spectral components where numerous different plasmon modes can be present within a very narrow energy range. We have used three different processing routines on the obtained EELS data in order to extract the plasmonic properties of the hollow nanostructures. Prior to the application of the processing routines, we have aligned the energy of the each pixel of the SI using the zero-loss peak as a reference. In Chapter 3, we will compare all three methods of spectral fitting via Gaussian fitting, independent component analysis (ICA) via blind source separation (BSS) and spectral unmixing via vertex component analyses (VCA). Plasmonic components presented in Chapter 4 were obtained by using Gaussian fitting and VCA routines. Since the results presented throughout these two chapter indicated that VCA routine provides more reliable plasmonic components compared to the Gaussian fitting and BSS, we have only applied VCA to obtain the plasmonic components of the different nanocubes and nanoframes in 3D presented in Chapter 5.

2.3.1 Gaussian fitting

We have used Gatan$^{\mathrm{TM}}$ Digital Micrograph (DM) software to apply Gaussian fitting to the EELS datasets using Nonlinear Least Squares (NLLS) curve fitting algorithm implemented in DM.

In Fig. 2.10, we show the application of a Gaussian fitting to the EELS data of the single-walled AuAg nanobox. After aligning the ZLP positions, we subtract the ZLP and background by using power law algorithm [234], also implemented in DM. Thus, we have a background subtracted EELS SI as shown in Fig. 2.10A. The summed EELS spectrum of the SI is shown in Fig. 2.10B. We, then, fit a Gaussian to the main plasmon peak as shown in this figure. After applying the NLLS algorithm, we obtain the results composed of center of the Gaussian peak fitting in each SI pixel (Fig. 2.10C), amplitude of the Gaussian (Fig. 2.10D) as well as the FWHM and residual signals after the fitting procedure (which are not shown here). The center of the Gaussian is based on the distribution of the energy of the peak positions with maximum intensity. Therefore, it is used as the plasmon energy distribution map. The amplitude of the Gaussian reveals the distribution of maximum peak intensities in each pixel, thus, it is used as plasmon intensity distribution map. Throughout this thesis we present the results obtained by Gaussian fitting in the temperature color scale, which are shown in the lower row of Fig. 2.10C and Fig. 2.10D, along with the scale bar of this color scale. For the energy maps, this color scale represents the distribution of energies in eV. For instance, the colored center map shown in Fig. 2.10C reveals the distribution of plasmon energies between 1.9 eV and 2.4 eV. On the other hand, plasmon intensity maps are presented in arbitrary units.

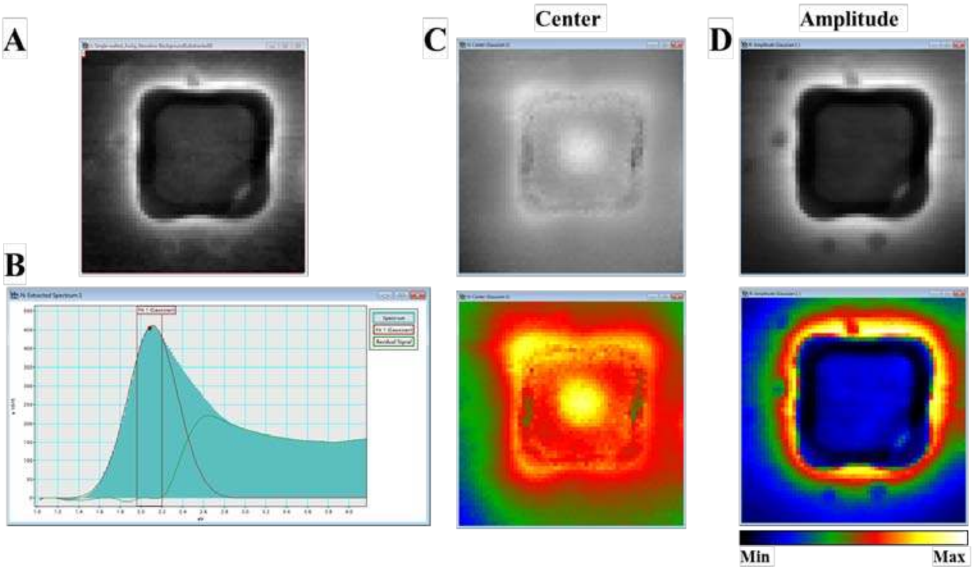

FIGURE 2.10: A. Background subtracted EELS SI obtained from the single-walled AuAg nanobox. B. Summed EELS spectrum over the SI where a Gaussian peak is fitted to the main plasmon peak. C. Center of the Gaussian fitting, which is used as plasmon energy distribution map. D. Amplitude of the Gaussian fitting, which is used as plasmon intensity distribution map. In the lower row of C and D, center and amplitude maps are shown in temperature color scale.

2.3.2 Blind Source Separation

In addition to the above presented Gaussian fitting, we have used a multivariate component analysis (MVA) based technique, namely independent component analysis [234] based on the combination of principal component analysis (PCA) and blind source separation (BSS). We have used an open source Phyton library named HyperSpy multidimensional data analyis toolbox to apply PCA and BSS which is freely available online at www.hyperspy.org [268].

In PCA, which is the most popular multivariate method, the signal is assumed to comprise a linear combination of contributions from individual elements and components.

It is also assumed that these contributions would have higher variance than the noise, thereby, the noise can be isolated from the signal and, mostly, eliminated from the data [234]. This technique decomposes the SI into two matrices which are factors and loading matrices that contain the spectral signature and the weighting of the factor components, respectively. We elaborate how thesse two matrices are obtained in the following.

The spectrum S_i from each pixel, thus, can be written as the sum of the components X_k which has a weighting $P_{i,k}$ [269]:

$$S_i = \Sigma_k P_{i,k} X_k \tag{2.1}$$

The components are orthogonal and described as *eigenspectra* [269]. It should be taken into account that, although the first component of an uncentered data represents an average spectrum, these components do not, in general, correspond to the ionization edges of particular elements and therefore may not have direct physical meanings [234]. The SI data can now be arranged as a two-dimensional data matrix

$$\mathbf{D}_{((x,y),E)} = \mathbf{S}_{((x,y),n)} x \mathbf{L}^T_{(E,n)}, \tag{2.2}$$

where $\mathbf{S}_{((x,y),n)}$ is called the score matrix and $\mathbf{L}_{(E,n)}$ is called the loading matrix (the superscript T of $\mathbf{L}$ represents a matrix transpose) [270]. In such a dataset, each row of the matrix $\mathbf{L}^T$ contains an eigenspectrum which is uncorrelated with the other rows and each column of $\mathbf{S}$ gives the spatial distribution of the corresponding eigenspectrum in the loading matrix [234, 270]. The individual product of each of these loading and score matrices is called a *principal component* [270].

The number of components is n and it is equal to the smaller of x·y and E. Matrix decomposition is then carried out by applying *eigenanalysis* or *singular value decomposition* to the data matrix [234]. In the decomposed matrix, the components are ordered from high to low according to their eigenvalues, thus, to their variance or information content. It should be noted that the main idea of improving signal-to-noise ratio by PCA relies on the fact that the number of the useful data is typically much less than n and the lower-variance components mostly present the noise. A so-called *scree plot* is a plot that shows the logarithms of the eigenvalues against component number. For instance, Fig. 2.11 shows the variances of the components for the dataset obtained from the single-walled AuAg nanocube by using PCA in HyperSpy. We have used 5 components in order to obtain plasmonic components from these dataset, as the higher number of components were producing too much noise.

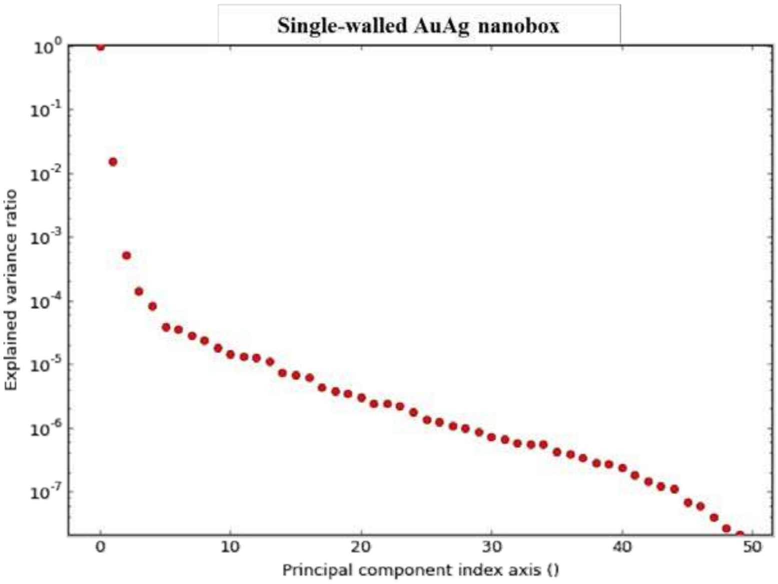

FIGURE 2.11: Scree plot showing the variance of the components obtained by applying the weighted PCA on the EELS data of the single-walled AuAg nanobox.

The PCA method is quite useful to improve the signal-to-noise ratio. However, experimental EELS spectra do not always fulfill the requirement of orthogonality and nevertheless they are not composed of independent spectra. Bonnet et al. [271] developed a new method for analysing series of spectra which is called independent component analyses (ICA) or blind source spearation (BSS). It is based on the complementation of two existing methods of spatial difference method and MVA [234]. Hence as the name suggests, this method attempts to find components that are mutually independent, rather than orthogonal as in the case of PCA. It has been proven to provide completely independent signal separation by using processed EELS data via differentiation process, where working with the derivative data is found to be quite efficient [234, 271]. It has been applied for the processing of EELS data obtained from different materials [265, 272–274] and shown that it gives more reliable components than PCA [274]. However, as underlined above, the application of this routine requires the processing of the experimental EELS datasets such a linear processing which allows the quantification to be performed on the results of the unmixing procedure [271]. Therefore, it is found convenient to use BSS method in combination with PCA [265, 273]. These studies clearly demonstrated that how ICA-BSS algorithm can, in certain cases, transform the principal components into easily interpretable independent components.

Having said that, let us summarize the procedure we follow in order to apply BSS on the EELS datasets obtained from the hollow AuAg nanostructures presented in Chapter 3. In the first step, we use the weigthed PCA, in which the dataset is described as a weighted sum of finite number of components and Poissonian noise that are separated according to their variances. Application of weighted PCA allows us to increase the signal-to-noise ratio by reconstructing the dataset only with the higher variance components and therefore, minimizing the noise contribution. Then, we apply BSS algorithm to obtain independent plasmonic components from the datasets. Both weighted PCA and BSS algorithms are implemented in HyperSpy [268].

2.3.3 Vertex component analysis

The third approach we have used to process the EELS data is a spectral unmixing (SU) based routine via combination of vertex component analysis (VCA) improved by the implementation of the bayesian linear unmixing (BLU) algorithm. VCA is developed by Nascimento and Dias [275] and BLU is developed by Dobigeon et al. [276].

VCA is an unsupervised algorithm and based on the geometry of convey sets, exploiting the fact that endmembers (factors) occupy the vertices of a simplex [275]. This algorithm is based on the hypothesis of pure pixels in the data, assuming that resulting spectra are present among the observed pixels, however, it is often not the case for experimental EELS data [274, 277, 278]. A more complex spectral unmixing algorithm, bayesian linear unmixing (BLU) algorithm, which does not need the assumption of pure pixels, has been developed by Dobigeon et al. [276] and recently applied to core-loss EELS data [274].

Dobigeon and Brun compared the efficiency of different routines such as PCA, ICA and BLU and reported that BLU provides an improvement on the obtained spectral signatures (endmembers) and their associated maps (abundances) [274]. In ICA algorithm, the endmember signatures are found by multiplying the spectral vectors with an unmixing matrix, which minimizes the mutual information among channels (remember that they are considered as independent from each other) [275]. If the sources are truly independent, ICA provides the correct unmixing as the minimum of the mutual information corresponds to independent sources. However, it is not valid for dependent fractional abundances, although some endmembers can be approximately unmixed [279]. It is reported that ICA and PCA may perform poorly for linear spectral mixture analysis due to the strong dependences between the abundances of different materials [274].

The VCA routine we have used throughout the thesis manuscript is also implemented in HyperSpy multidimensional data analysis toolbox [268].

2.4 Boundary element method simulations

We have used simulations based on the boundary element method (BEM) in order to have better understanding on the results experimentally obtained throughout this thesis manuscript.

Simulations of electron energy-loss probabilities of arbitrary shaped structures are developed by Garcia de Abajo and Howie [280, 281], by an approach named as boundary element method (BEM). It consists in expressing the 3D dependence of the scalar and vector potentials in terms of interface charges and currents via a set of surface integral equations, as it assumes that the different media involved in the studied structures are described by frequency-dependent local dielectric functions (as explained in Chapter 1) and terminate in abrupt interfaces [281]. In other words, this method is based on the solution of Maxwell's equations in the presence of arbitrarily shaped abrupt dielectric interfaces, which involves the interface charges and currents that act as sources of the induced electromagnetic field (see [281] for more information about the theory behind this approach).

In particular, we have used a Matlab$^{\text{TM}}$ toolbox developed by Hohenester and Trügler [282] called MNPBEM, which calculates the plasmonic properties of metallic nanoparticles based on the BEM approach. This approach has several advantageous over other commonly used approaches such as discrete dipole approximation (DDA) [283, 284] and finite-difference time-domain (FDTD) [285] as it assumes a dielectric environment where bodies with homogeneous and isotropic dielectric functions are separated by abrupt interfaces, rather than assuming a general inhomogeneous dielectric environment [286]. Moreover, for the simulation of metallic nanoparticles embedded in dielectric environments, it has the advantage of generating faster simulations with moderate memory requirements due to the fact that only the boundaries between different dielectric materials have to be discretized instead of whole volume [282]. Over the years, BEM approach has been successfully applied to simulations of various plasmonic nanostructures characterized by EELS [203, 217–219, 222, 223, 287–289].

During BEM simulations presented in this thesis manuscript, we have used the optical data from Johnson and Christy [13] and modified them according to the [77] for the case of AuAg alloys. We have also taken into account the size effects on the dielectric properties [2]. Throughout this thesis manuscript, we have exploited the BEM simulations in order to elaborate the shape, composition and environmental (substrate) effects on the plasmonic properties of hollow AuAg nanostructures.